Phase transitions and optically induced phenomena in cooperative systems

Fausti, Daniele

Phase Transitions and Optically Induced Phenomena in Cooperative Systems

Daniele Fausti

University of Groningen
Zernike Institute
for Advanced Materials

Zernike Institute PhD thesis series 2008-11
ISSN 1570-1530
ISBN: 978-90-367-3476-9

The work described in this thesis was performed in the research group Optical Condensed Matter Physics of the Zernike Institute for Advanced Materials at the University of Groningen, the Netherlands. This work is part of the research programme of the 'Stichting voor Fundamenteel Onderzoek der Materie (FOM)', which is financially supported by the 'Nederlandse Organisatie voor Wetenschappelijk Onderzoek (NWO)'.

Printed by: Facilitair Bedrijf RuG, Groningen.
Front Cover: Marco Furri, *La montagna* (2002).
Cover layout: Marcel Zinger.

RIJKSUNIVERSITEIT GRONINGEN

Phase Transitions and Optically Induced Phenomena in Cooperative Systems

Proefschrift

ter verkrijging van het doctoraat in de
Wiskunde en Natuurwetenschappen
aan de Rijksuniversiteit Groningen
op gezag van de
Rector Magnificus, dr. F. Zwarts,
in het openbaar te verdedigen op
maandag 16 juni 2008
om 13:15 uur

door

Daniele Fausti

geboren op 6 mei 1978
te Gardone V.T. Brescia, Italië

Promotor:	Prof. dr. ir. P. H. M. van Loosdrecht
Beoordelingscommissie:	Prof. dr. P. Rudolf
	Prof. dr. D. Komskii
	Prof. dr. F. Parmigiani

alla mia famiglia

Contents

Chapter 1

Introduction and Theoretical Prologue

1.1 Memories and invitation

When I was a child, I was extremely fascinated by the snow melting in the sun. At that time, I would have never thought that this memory could be the starting sentence of my PhD dissertation. Back then, I could not explain to myself how substances made of the same element could display such different properties. Water was liquid and transparent, snow soft and opaque and ice again transparent but extremely hard. Today the title of this dissertation "Phase transitions and optically induced phenomena in cooperative systems" could be reformulated less scientifically but funnier as "The snow melting in the sun, as I see it now".

In thermodynamics a phase transition is the passage of a thermodynamic system from one phase to another without changing its chemical composition. The physical properties of the two phases can be substantially different, and hence the transition can be seen as a sudden (or smooth) change in the physical properties of the system. The most intuitive perspective on how a phase transition can dramatically changes the physical properties of a system comes from those involving a transition of the aggregation state (e.g. solid-liquid, liquid-gas or solid-gas transitions). The best known example of such a transition is probably the water-ice transformation, which obviously changes the mechanical properties of H_2O in a dramatic way. Possibly more difficult to grasp, but no less interesting, are solid-solid phase transitions that do not change the aggregation state of a material but only some of its physical properties like conductivity, stiffness, density, or magnetization. An example of such a phase transition involves the well-known magnetic properties of iron crystals. Due to a transition from a "magnetic" to a "non-magnetic" phase, the attraction between two pieces of iron disappears if the crystal is heated above 750°C, while the solid aggregation changes remains up to

1300°C.

The interaction of light with matter lies at the very core of our knowledge of the world. The "optical" investigation of nature started with humankind. It is hard to imagine the amount of "scientific" questions that a sunset, a rainbow, an eclipse or just the properties of a fluorite crystal must have raised in our ancestors. Probably our ancestors, as many of our contemporary fellows, did not pay too much attention to the fact that our vision itself is based on the light-matter interaction. In our eyes, harvesting the electromagnetic bath we happen to live in is the starting point of a process that finally leads to the image of the objects which we form in our brain. In this sense, the interaction of light with matter is one of the most valuable tools that we have to explore and understand the properties of the nature surrounding us. Obviously, in the course of the scientific history of the last centuries, many other investigation tools have been developed. Nevertheless it is interesting to note that the large majority of these "tools" is still substantially based on different kinds of radiation-matter interaction phenomena. The most obvious examples are found in the large variety of spectroscopic techniques available, from γ-rays to the far infrared spectroscopy, which are all based on the interaction between radiation and matter.

On the other hand, it is clear from various examples in nature, that light, apart from being used as an analysis tool, can also strongly affect the properties of matter itself. It can trigger various physical phenomena and can even be used to control matter's behavior and properties. The first intuitive example of a light-induced phenomenon has already been mentioned in the first sentence of this dissertation: heating. When matter absorbs light, the energy carried by the electromagnetic field is taken up by the material and heat is generated. As a consequence of this, the state of matter can be influenced. Returning to the example from my youth, the snow-water phase transition is a marvelous example of *optically induced phase transition*. The energy carried by the sun beams is transformed into thermal energy (vibrations) in the ice and these vibrations, above a certain excitation density, are strong enough to break the bonds between the water molecules inducing melting of the snow crystals. In addition to the optically induced phenomena due to radiation heating, light can transform matter in a way "directly related" to the absorption process itself, and not mediated by the average induced heat. Here one can think of photosynthesis, the vital energy harvesting process in plants, which transforms carbon dioxide and water into glucose and oxygen by making use of the "direct" absorption of light in a receptor molecule and leaving the temperature of the system virtually unchanged (no thermalization process is required).

The knowledge of how the light can perturb a system to the extent that its macroscopical physical properties are changed cannot proceed without understanding the dynamics of the photon-atom interactions. How does the radiation absorption interfere with the material's properties? When are these properties effectively perturbed? How long does the system need to recover equilibrium? These are all questions that on one hand help to understand the phenomena, and

on the other hand point the way to control the properties of matter, out of the thermodynamical equilibrium, using optical techniques. The possibility of shaping the state of a material through irradiation and thereby obtaining transient "phases", i.e. phases with properties not achievable under thermal equilibrium, has stimulated an enormous interest in the scientific community over the last decade. Another aspect that makes this branch of physics extremely appealing is the fact that the laser technology developed over the last two/three decades allows to easily produce extremely short light pulses (less than 10^{-13} seconds). This kindles the hope of controlling those transient properties on extremely short timescales, paving the way to countless potential applications in different fields, from fast electronics to micromechanics. Nowadays it is only possible to speculate on the impact that the ultrafast optical control of material properties will have in the years to come, but given all the recent advances in this field I dear to say: "the future looks bright!"

When a quantum of light - a photon- interacts with matter, many possible processes can happen: absorption, diffusion, scattering. In particular, the research reported in this thesis focuses on a technique based on the inelastic scattering of light, called Raman spectroscopy. When a beam of light interacts with a material, a tiny fraction of the photons (10^{-8}-10^{-10} with respect to the incident ones) are scattered into photon with a different energy. From the study of the characteristic energy of the scattered light, it is possible to retrieve the characteristic excitations of a system and thereby to extract detailed information on its state and symmetry.

It is worth to spend here a few words to explain why Raman spectroscopy is a unique tool for studying photo-induced dynamics and non-thermal phenomena. There are two main Raman scattering processes. In the first one, called Stokes process, the energy of the emitted photons is lower than that of the incoming photons and therefore the system is left in an excited state after the scattering process. Conversely, in scattering processes of the second type, called Antistokes, the energy of the photon leaving the sample is larger than that of the incoming photons and an excitation is annihilated in the sample. It is easy to understand how the Antistokes processes are strongly dependent on the presence of excitations. For example, in a crystal at 0 K, there will be no excitation present and therefore all the Antistokes scattering processes will be quenched. As will be explained later in this chapter, from a comparison of the Stokes and Antistokes intensities, it is possible to monitor specifically the temperature of the investigated excitations. The properties of complex systems are determined by the interplay between different degrees of freedom: vibrational, magnetic, and electronic. Making use time resolved Raman Spectroscopy it is possible to extract detailed information on the temperatures of these different degrees of freedom and thereby to extract detailed information on the nature of the observed processes. If one can follow at the same time the properties and the temperature of a system, one has a unique tool to study the nature of dynamical processes in matter, and in particular to discriminate between thermal and non-thermal processes. Hence the interest to implement time-resolved Raman spectroscopy, a subject which will be described

in the central part of this thesis.

We are just beginning the exploration of the previously inaccessible universe of systems far from the thermal equilibrium. The possibility of inducing material properties non-existent under equilibrium conditions and of controlling them on an ultrafast time scale discloses a world whose laws, and possible applications, are still mainly unexplored. This makes the spectroscopist job in the twenty first century intriguing and compelling!

1.2 Detailed Summary

The work described in this thesis is divided into two main parts. In the first part (chapters 2 and 3), standard Raman spectroscopy, together with different other techniques, is employed to study the magnetic and structural properties of two different families of crystals: $RFe_3(BO_3)_4$ (R = Gd, Tb, Nd, Y and Er) and TiOX (X = Cl and Br). The second part of the thesis (chapter 4, 5, and 6) is devoted to the description of the dynamical version of the Raman spectroscopy. It starts with a description of the technique itself and the set-ups we developed for time resolved Raman spectroscopy (chapter 4), followed by two examples of how the technique can be employed to study optically induced phase transitions in semimetals (chapter 5) and an organic charge-ordered salt (chapter 6).

The second chapter present a study of the cascade of phase transitions characteristic of the family of crystals called "rare-earth-ferroborates". A structural phase transition at high temperature is followed by two magnetic phase transitions at lower temperature: an antiferromagnetic ordering and a spin-flop transition. Through the study of the vibrational properties (phonons) we could reveal that the structural transition has an unusual "weakly first order character". The order parameter of the phase transition was found to display an unusual behavior intermediate between a first order transition (hysteresis) and a second order transition (soft mode behavior). This anomalous phenomenon is explained in the light of the particular symmetry of the crystal structure of this family of compounds. In addition to this, the analysis of the magnetic excitations revealed the presence of short range magnetic correlations in the paramagnetic phase up to unprecedented high temperatures. This will be discussed in Chapter 2 in terms of the low dimensional structural characteristics of the magnetic system.

In the third chapter we present a symmetry disquisition about the different phases of a class of transition metal oxides, namely titaniumoxihalides (TiOCl and TiOBr). The electronic configuration of the Ti ions ($3d^1$), together with the low-dimensional character of the magnetic interaction, make these systems ideal candidates for a Spin-Peierls transition, previously observed in only one other inorganic compound ($CuGeO_3$). Our Raman study of the phase transition focused on two particularly interesting aspects: i) the low temperature phase transition (Spin-Peierls transition) is preceded at higher temperatures by a second phase transition to an intermediate phase; ii) the Spin-Peierls transition has a first order character in contrast to its conventional theoretical description. In chapter 3 we also explain how by studying the symmetry of the vibrational modes characteristic of the three phases, we managed to suggest the space group of the Spin Peierls phase (later confirmed by an X-ray structure determination). Using the same approach we gave some symmetry arguments to rationalize the anomalous first order character of the Spin Peierls transition.

In the fourth chapter we describe the different experimental setups used in the experiments and the commissioning we did to characterize them. The chapter starts with a description of the continuous wave Raman setup where we review

its specifications. In the second part of the chapter the two approaches used for achieving dynamical Raman information will be detailed. The first approach, used for the experiments in chapter 6, is based on a custom made mechanical chopper and achieves a time resolution of 10μsec and a frequency resolution of 1cm^{-1}. The second approach makes use of normal interferometric techniques to achieve a time resolution of a few picoseconds at the cost of the frequency resolution which degrades to 8-10cm^{-1}.

In the fifth chapter we report on the study of the elemental crystals of Bismuth and Antimony. The room temperature thermodynamically stable phase of both materials is characterized by a semimetallic behavior due to a Peierls distortion ("Jones-Peierls mechanism"). Through ultrafast Raman measurements, we unraveled two distinct dynamics following intense laser excitation, one ascribed to a thermal and other one to a non-thermal pathway. We could show how, via optical excitation of electrons into the conduction band, it is possible to control, in a non-thermal way, the crystal distortion by reducing the electronic energy gain responsible for the stabilization of the Peierls distortion. Moreover, for excitation fluences larger than 5mJ/cm^2, corresponding to 3 excited electrons per atom, a new phonon becomes Raman active. We interpreted this as evidence of an optically induced phase transition to a non-thermal "phase" which will hopefully stimulate future studies to clarify its precise nature.

In the sixth chapter we present a study of the previously discovered optically induced insulator-metal phase transition in the organic crystal $(\text{EDO-TTF})_2\text{PF}_6$. Resistivity measurements on this organic salt show a metal to insulator phase transition when the temperature is lowered below 280 K. The low temperature insulating phase is characterized by a charge order on the EDO-TTF molecules. It has previously been shown that by irradiating the low temperature phase with light pulses at 800nm and an extremely low excitation density (1 photon every 500 molecules), it is possible to induce a transient metallic phase, lasting a few hundred microseconds. This phase was suggested to be the high temperature phase. Our transient Raman measurements give clear indication that the photo-induced phase, although also metallic, could be of a different nature than the high temperature phase.

1.3 Theoretical Prologue

There are many topics touched upon on this thesis and the appreciation of the central part of this work requires a background knowledge of different subjects and techniques, not necessarily *"historically related"*. The aim of this section is to summarize this background in a form useful for reading the core of this thesis. The arguments given are not intended to be complete but rather they are meant as an "informal reminder" of fundamental concepts.

In the first part of this section, we shall review the spectroscopic techniques used, focusing mainly on the theory fundament of Raman spectroscopy. In particular we shall give an introduction on the most important scattering processes that will be encountered in the different parts of this thesis. While reviewing the scattering processes we shall give touch on different excitations in solids, focusing on the magnetic ones. In the second part of this section we shall try to give a taste of the theories behind the intriguing solid state phenomena encountered in low dimensional magnetic systems.

1.3.1 "Technique" Physics

Introduction to the Raman Effect

In 1922, the Indian physicist Chandrasekhara Venkata Raman published his work "Molecular diffraction of light"[17]. This was the first of a series of investigations with his collaborators which ultimately led to his publication in 1928 of "A new radiation"[1], that reported the discovery of the radiation effect which bears his name. This effect had been predicted theoretically in 1923 by Smekal, and was independently discovered by Grigory Landsberg and Leonid Mandelstam in 1928. Raman's paper presented the most exhaustive work and in 1930 he was awarded the Nobel Prize for his work.

When light is impinged on a molecule or from a crystal, most of the photons scatter elastically. However, a small fraction of light (approximately 1 in 10^8 photons, depending on the cross section of the specific compound) may scatter inelastically, thereby changing the photon energy. This process of inelastic scattering of light is termed the Raman effect. A large body of literature focuses on the vibrational Raman effect, namely scattering from vibrational and rotational excitation in molecules and solids. The Raman effect is, however, much more general since it is not limited to the vibrational effect, but also refers to scattering processes from other fundamental excitations. Indeed, inelastic light scattering, such as that from magnetic and electronic excitations, has proven to be a valuable tool in contemporary condensed matter physics. The introductory nature of this section leads us to proceed with the following logic: we shall firstly start with a simple classical model explaining the Raman effect for molecules, in an attempt to make it intuitively clear. Secondly, we shall discuss the effect in crystals and finally treats the quantum mechanical scattering process in more details to ex-

plain the "thermodynamic" information revealed by this technique. This will be useful to clarify the specific potential of Raman spectroscopy for studying non thermal processes. The second part of the chapter is devoted to the introduction of the concept of magnons and of Raman scattering from magnetic excitations. In the final part we shall introduce some peculiarities of low dimensional magnetic systems.

Classical Description The classical description of Raman scattering interprets the scattering as originating from a change in molecular polarizability due to the presence of vibrational modes in the system. For an applied electromagnetic field $E(\omega)$, the polarizability α_0, gives a dipole moment $P_D(\omega) = \alpha_0 E(\omega)$, which acts as a source of an evanescent wave. If the molecule is vibrating at the frequency of a vibrational eigenmode (Ω), the polarizability becomes modulated at the same frequency by an additional term $\alpha_1 = \frac{d\alpha}{dr}$. We can write the dipole moment as $P_D(\omega) = (\alpha_0 + \alpha_1 \cos(\Omega\ t))E(\omega)$ and by substituting the field with a plane wave, it is easy to obtain:

$$P_D(\omega) = \alpha_0 E_0 cos(\omega\ t) + \alpha_1 E_0/2[cos((\omega + \Omega)t) + cos((\omega - \Omega)t)] \tag{1.1}$$

Thus the evanescing light oscillates mainly at the field frequencies ω, but also at two frequencies $\omega - \Omega$ (Stokes line) and $\omega + \Omega$ (Antistokes). In normal cases, α_1 is many orders of magnitude smaller than α_0, thus the side bands are extremely weak compared to the elastically scattered light. A vibration will give a Raman response if it induces a change in the molecular polarizability. This is not necessarily the case for any vibration, but rather depends on the particular deformation induced. For the calculation of the molecular selection rule using molecular point group symmetry we refer to [3].

Phonons in solids have a periodic structure and this causes the Raman scattering process to be directional for a given phonon and a given excitation intensity. To put it simply, to evaluate the scattering cross section, it is necessary to take into account the interference between photons scattered in different parts of the crystal. The constructive interference will be given for $sin(\theta/2) = n\lambda/2\Lambda$, where θ is the angle between the incident and scattered light, n the refractive index of the crystal, λ the wavelength of the incident light, and Λ the wavelength of the phonon[1].

To describe the scattering processes in crystals, following the approach of [2], we can proceed in a similar manner, namely by expanding the susceptibility tensor χ_{ij} in terms of the the normal coordinates of the phonons (Q_k) instead of the atomic displacements of Eq.1.1.

$$\chi_{ij} = (\chi_{ij})_0 + \sum_k (\frac{\partial \chi_{ij}}{\partial\ Q_k}) Q_k + h.o. \tag{1.2}$$

[1]The usual "almost flat" dispersion of optical phonon close to the k=0 point of the Brillouin zone, will make the directionality of the average signal weak. This is the reason why in most of the experiments, a small misalignment of the crystal axis will not be crucial.

The coefficients $\frac{\partial \chi_{ij}}{\partial\ Q_k} = \chi_{ij,k}$ constitutes a tensor also known as the Raman tensor, and the intensity of the Raman scattered light is proportional to its square. The induced dipole moment which accounts for the emission of the side bands is (with an incident field $E_l^i(t) = E_{l,0}^i cos(\omega t)$ and the phonon expressed as $Q_k = Q_{k0} cos(\Omega_k t)$):

$$P_{Dj}^s(\omega \pm \Omega_k) = \chi_{jl,k} \varepsilon_0 V_u E_{l0}^i Q_{k0} \cos(\omega \pm \Omega) t \tag{1.3}$$

where V_u is the volume of the unit cell. The scattering intensity is proportional to the square of the dipole moment, P_D^s, which is given for a mode and for a selected direction of polarization, e^s, of the scattered light by the square of the projection of P_D^s on e^s:

$$\phi(k) = C|e^s P_D^s|^2 = C|\sum_j e_j^s P_{Dj}^s(k)|^2 \tag{1.4}$$

where P_{Dj}^s are the components of the dipole moment induced by the Raman effect given by Eq.1.3. It follows that the scattering intensity is given by:

$$\phi(k) = C|\sum_{jl} e_j^s \chi_{jl,k} e_l^i|^2 \tag{1.5}$$

Eq.1.5 shows how it is possible to measure any component of the Raman tensor by selecting the proper combination of the incoming and scattered polarization.

Selection Rules Crystals can be classified in terms of the symmetry operations required to generate all the crystal (with the atoms at the equilibrium positions) starting from a single atom or a basis (for non-primitive lattices). The set of these symmetry operations obeys the mathematical criteria for a group and is called the "Space group". The determination of the number of vibrational modes, their symmetry, and hence the selection rule for infrared and Raman absorption becomes easier when making use of the group theoretical analysis. The scalar properties such as temperature and density of a crystal, will be invariant under the symmetry operation of the group. Conversely, vectorial and tensorial properties like dipole moments and susceptibility, are not invariant under the symmetry operation of the group. Vectorial properties transform like the coordinates (x,y and z), while tensorial properties transform as the products of the cartesian coordinates. Similarly, the symmetry representations for the susceptibility tensor are the same as those of quadratic terms involving the Cartesian coordinates, x^2, y^2, z^2, xy, yz, and xz. That means that an excitation is not infrared-active if its representation does not contain terms transforming as the cartesian coordinates under the symmetry operations of the group. In the same way, excitations involving a change in the susceptibility of the crystal must have the representation of the quadratic form, since excitations without this characteristic will not be Raman active. A particularly interesting case is that of centrosymmetric crystals, where the presence of an inversion center (written as the symmetry operator $x, y, z \longrightarrow -x, -y, -z$) make the infrared and Raman activity mutually exclusive.

Quantum Mechanics A theoretical description of the Raman scattering proceeds by calculating quantum mechanically the dipole moment induced by the incident light; this is done through the second order perturbation theory considering a classical electromagnetic field as a perturbation. By subsequently making use of the "correspondence principle", the intensity of the radiation emitted by the dipole moment is calculated by the classical expression for an oscillating dipole. The full description goes beyond the purpose of this thesis and can be found elsewhere ([7]). The aim here is to give an insight into how thermodynamics come into play, giving access, through the ratio of Stokes to Antistokes intensities, to a local temperature measurement. The schematic view of Raman scattering is sketched in Fig.1.1. In the left part (Stokes process), an electron is excited by a photon and this excitation is followed by a recombination with a simultaneous emission of a photon of different energy. Also in the Antistokes process the final state ($< f|$) differs from the initial one ($|i >$) by the absorption of an excitation of the system, and is reached from the initial state via an intermediate state. This could be a real electronic state (resonant Raman scattering) or a virtual one.

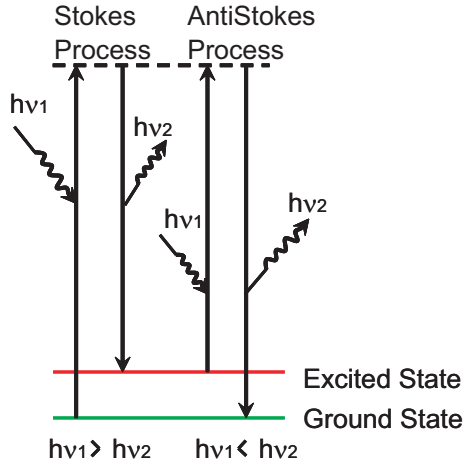

Figure 1.1: *Schematic view of the Raman process. The Stokes process creates an excitation in the system, while the Antistokes annihilates one.*

The quantum mechanical analogue of Eq.1.3, describing the polarization induced by an electromagnetic field is $P_{fi} =< f|\varepsilon_0 \chi\ E|i >$, where $< f|$ and $< i|$ are wave functions considering both electronic and nuclear coordinates. Following the adiabatic (or Born-Oppenheimer approximation) the total wave functions can be factorized in a electronic part $\varphi(x, X)$ and a nuclear part $\varrho(X)$. If the wavelength of the field is larger than the interatomic distances we can extract the field from

the integral and obtain:

$$< f|\chi|i >= \int \varrho_f^*(X)\varphi_f^*(x,X)\chi\varphi_i(x,X)\varrho_i(X)dxdX \tag{1.6}$$

Considering that only the electronic part of the susceptibility is still dependent on the atomic coordinates, we can expand it in term of the normal coordinates (Q_k):

$$< f|\chi|i >= (\chi)_0 < ..\nu_{fk}..|..\nu_{ik}.. > + \sum_k (\frac{\partial \chi}{\partial\ Q_k})_0 < ..\nu_{fk}..|Q_k|..\nu_{ik}.. > \tag{1.7}$$

Where the *bra* an *ket* represent the total vibrational wave function of Eq.1.6, and they are expressed as the product of harmonic oscillator wave function, where the ν_{ik} and ν_{fk} are their occupation numbers:

$$< \nu_{f1}..\nu_{fk}..\nu_{fn}| = \prod_k < \nu_{fk}| \quad \text{and} \quad < \nu_{i1}..\nu_{ik}..\nu_{in}| = \prod_k < \nu_{ik}| \tag{1.8}$$

where $< \nu_{fk}|$ and $< \nu_{ik}|$ again stay for harmonic oscillator wave function with occupation number ν_{fk} and ν_{ik}. The products between two wave function are:

$$< \nu_{fk}|\nu_{ik} >= \begin{cases} 0\ , & \text{for } \nu_{fk} \neq \nu_{ik} \\ 1\ , & \text{for } \nu_{fk} = \nu_{ik} \end{cases}$$

and the normal coordinate expectation value is:

$$< \nu_{fk}|Q_k|\nu_{ik} >= \begin{cases} 0\ , & \text{for } \nu_{fk} = \nu_{ik} \\ (\nu_{ik}+1)^{1/2}\sqrt{\hbar/2\Omega_k}\ , & \text{for } \nu_{fk} = \nu_{ik}+1 \\ (\nu_{ik})^{1/2}\sqrt{\hbar/2\Omega_k}\ , & \text{for } \nu_{fk} = \nu_{ik}-1 \end{cases}$$

The first term in Eq.1.7 is different from zero only if $\nu_{fk} = \nu_{ik}$, so that the final state population is unchanged (Rayleigh scattering). The second term, as made clear by the derived susceptibility, describes the Raman scattering. According to Eq.1.9, this term is different from zero for the mode k $\nu_{fk} = \nu_{ik} \pm 1$, where Eq.1.7 is reduced to:

$$\begin{aligned} < \nu_{ik}+1|\chi|\nu_{ik} >= (\nu_{ik}+1)^{1/2}\sqrt{\hbar/2\Omega}(\frac{\partial \chi_{mn}}{\partial\ Q_k})_0 \qquad (Stokes) \\ < \nu_{ik}-1|\chi|\nu_{ik} >= (\nu_{ik})^{1/2}\sqrt{\hbar/2\Omega}(\frac{\partial \chi_{mn}}{\partial\ Q_k})_0 \quad (Antistokes) \end{aligned} \tag{1.9}$$

Comparing these equations with Eq.1.2, one notes the equivalence between the tensor for the transition susceptibility and the derived susceptibility multiplied with the amplitude of the normal coordinates. In the quantum mechanical calculation the amplitude of the normal coordinate is replaced by the quantum mechanical equivalent $\sqrt{\hbar/2\Omega}$. Attention must be paid to the dependence of the

scattering intensity on the occupation number, ν_k, determined by the Boltzmann factor:

$$W(\epsilon_k) = \frac{exp(-\epsilon_k/K_BT)}{Z} = \frac{exp[-\hbar\Omega_k(\nu_k + 1/2)/K_BT]}{\sum_{\nu_k} exp[-\hbar\Omega_k(\nu_k + 1/2)/K_BT]} \tag{1.10}$$

and a thermal average of the form $\sum_{\nu_k}(\nu_k + 1)W(\epsilon_k)$ is required to obtain the effective square of the tensor in Eq.1.9. Assuming the Raman tensor to be equal for the two processes (reasonable for transparent samples, but not at the edge of an absorption band), it is clear that the intensity of Stokes and Antistokes ratio is dependent on the local temperature on the sample as:

$$\frac{\phi_A}{\phi_S} = (\frac{\omega + \Omega_k}{\omega - \Omega_k})^4 exp(\frac{-\hbar\Omega_k}{K_BT}) \tag{1.11}$$

The intensities of the second-order Raman lines are obtained from the higher order expansion of the susceptibility and the statistics obtained are summarized in Tab.1.1. These are given in terms of the phonon mean occupation number n_i ($n_i = [exp(-\hbar\omega/k_BT) - 1]^{-1}$), and the intensities of the scattered light are proportional to the square of the result.

Table 1.1:

Process	Stokes	Antistokes
One-Phonon	$1+\mathrm{n}_i$	n_i
Two Phonon (Overtones)	$2+3\mathrm{n}_i+\mathrm{n}_i^2$	$\mathrm{n}_i^2-\mathrm{n}_i$
Summation	$1+\mathrm{n}_i+\mathrm{n}_j+\mathrm{n}_i\mathrm{n}_j$	$1+\mathrm{n}_i+\mathrm{n}_j$
Difference	$\mathrm{n}_j+ \mathrm{n}_i\mathrm{n}_j$	$\mathrm{n}_i+\mathrm{n}_i\mathrm{n}_j$

This gives an extremely useful insight on the possible application of Raman spectroscopy in dynamical studies of matter.

Provided that the matrix elements of stokes and antistokes scattering don't change in time, Raman spectroscopy provides a local probe for the temperature of the excitation under investigation, potentially allowing us to disentangle in a single measurement the real time evolution of, for example, electron, spin and lattice temperatures.

Raman Scattering from Magnetic Excitations

The experimental report of inelastic light scattering processes from magnetic excitation is almost 40 years younger than Raman's observation of the vibrational ones. The first observation of Raman scattering from magnetic excitations was only reported in 1966 for the antiferromagnet FeF_2[11]. The presence of magnons in magnetic materials causes a periodic modulation of the material's permittivity and light is scattered by this permittivity fluctuation.[8] A direct coupling between spin fluctuation and magnetic vector was shown to be negligible respect to

the first process.[8] To illustrate the light scattering process in a magnetic system, we follow the approach of reference [6].

The incident electric field E_I^i will produce a polarization proportional to the susceptibility $P^j(r,t) = \epsilon_0 \sum_i \chi^{ji}(r,t) E_I^i(r,t)$, where i and j indicate the three cartesian coordinates, ϵ_0 the free space permittivity, and χji the susceptibility tensor. As described in the previous section, the polarization acts as the source of the scattered field and the evaluation of the scattering cross section will be reduced to the evaluation of the correlation function $< \chi^{\alpha\beta} \chi^{\mu\nu} >_\omega$ (where the α, β, μ, and ν indicate the cartesian coordinates). The effective Hamiltonian describing the interaction of light with a magnetic system can be regarded as the electric dipole interaction between the polarization vector and the scattered field in a particular direction, E_S^j: $H = \sum_r \sum_{i,j} E_S^i \chi^{ij}(r) E_I^j$, where the sum over r indicates the sum over different magnetic sites. In magnetic materials the susceptibility can be a spin dependent quantity, and using a similar approach to the one previously described for vibrational Raman spectroscopy, we can expand the susceptibility at the site r in terms of the spins operators:

$$\chi^{ij}(r) = \chi_0^{ij}(r) + \sum_\mu K_{ij\mu}(r) S_r^{mu} + \sum_{\mu,\nu} G_{ij\mu\nu} S_r^\mu S_r^\nu + \sum_\delta \sum_{\mu,\nu} H_{ij\mu\nu}(r,\delta) S_r^\mu S_{r+\delta}^\nu + h.o. \tag{1.12}$$

The first term, χ_0^{ij}, is the susceptibility in the absence of magnetic excitation and will give rise to elastic scattering.

The one magnon scattering processes can be mostly described by the next terms (K and G), involving the spin operator on a single site. The linear coupling coefficient, K, is proportional to the magnetic circular birefringence, while the quadratic term, G, is proportional to the magnetic linear birefringence. The main macroscopic mechanism for the one magnon scattering process goes through electric dipole coupling of radiation to the crystal and relies on the spin-orbit coupling ($\lambda L \cdot S$) in the electronic excited state for changing the ion spin state. Further insight into the so-called Elliot-Loudon mechanism can be found elsewhere ([6, 18]). This thesis mostly concerns antiferromagnetic systems, where the main scattering process is the two magnon scattering, described by the last term of Eq.1.12 (H) and involving a pair of spin operators on different sites. This term can provide an additional (small) contribution to one magnon scattering, but what is more interesting, is that the term involving the H tensor gives rise to two magnon scattering, in which a pair of magnons is created or destroyed. In the Stokes process the frequency shift of the incoming light will be the sum of the frequencies of the two magnons created, $\Delta\omega = \omega(q) + \omega(q')$. Since the momentum of light, k, is very small with respect to the Brillouin zone, the momentum conservation law gives $q \approx -q'$ (see Fig.1.2 (a)). It appears straightforward that the two magnon processes are not limited (as the one magnon scattering) to the center of the Brillouin zone. Indeed, the two-magnon scattering feature results in a peak

near the frequency region where the magnon excitation spectra have the highest density of states, and this usually happens at the zone boundary (Fig.1.2(b)).

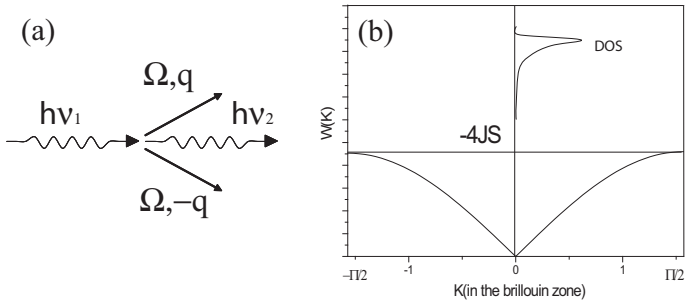

Figure 1.2: *Schematic view of the two magnon Raman scattering for antiferromagnetic samples. (a) In the scattering process, two magnons with opposite wave vector are created. To make the example clear, a sinusoidal magnon dispersion, derived for a one dimensional antiferromagnet, has been depicted (b). The two magnon scattering feature is proportional to the density of state of the magnon dispersion.*

The Elliot-Loudon process will give a contribution when extended to a higher order. However, this mechanism predicts a cross section substantially smaller than that of the one-magnon process. Conversely, as anticipated, experiments on antiferromagnets revealed that the two magnon scattering is of comparable intensity (and larger) than the one-magnon feature. This inconsistency was resolved by a suggestion of an alternative and more efficient scattering process for antiferromagnet, called the exchange-scattering mechanism[12].

We shall now try to give a simple explanation of the two magnon scattering processes in an antiferromagnet. The magnon excitation spectrum in a simple antiferromagnet consists of two magnon branches, corresponding to the spins precessing in opposite directions on the two sublattices $\omega^{\pm}(k)$. Physically the two branches correspond to excitations in which the total S^z operator changes by 1. It is easy to show that the two branches became degenerate in the case of 0 applied magnetic field [6]. The function which describes the state of each branch is denoted with $|k,+>$ and $|k,->$ to indicate whether the S^z is increased $(+)$ or decreased $(-)$. The linearly independent two-magnon state with wave vector k and $-k$ can be constructed as follows:

$$\begin{array}{ll} |a>=|k,+>|-k,+> & \Delta\ S^z=+2 \\ |b>=2^{-1/2}[|k,+>|-k,->+|k,->|-k,+>] & \Delta\ S^z=0 \\ |c>=2^{-1/2}[|k,+>|-k,->-|k,->|-k,+>] & \Delta\ S^z=0 \\ |d>=|k,->|-k,-> & \Delta\ S^z=-2 \end{array} \tag{1.13}$$

The states $|a>$ and $|d>$ with $\Delta\ S^z = \pm 2$ correspond to the one-magnon processes extended to higher order (the state $|d>$ is the only two-magnon state possible in a ferromagnet where the excitation spectrum is "single-branched"). The $|b>$ and $|c>$ terms ($\Delta\ S^z = 0$) describe spin deviations created on opposite magnetic sublattices, on sites which are exchange-coupled through a virtual electronic transition to higher states. The state with even parity ($|b>$) corresponds to two-magnon scattering processes, while the one with odd parity ($|c>$) is more relevant for two-magnon absorption processes. This results in a much more efficient scattering process than the one described as the one-magnon scattering extended to higher order. Moreover, this shows that two-magnon scattering arises mainly from a physically different process, and hence there is no a priori reason to expect the two-magnon intensity to be weaker than the one-magnon feature in antiferromagnets.

Time Resolved Reflectivity

Another technique which in the framework of the research of this thesis was used in the experiments described in chapter 5 and 6 is Time-Resolved-Reflectivity (TRR). Widely employed in the last 20 years thanks also to the availability of cheap ultrafast laser sources, TRR was probably the first basic experiment to study ultrafast dynamics in solids (even though often not the "more straightforward" to interpret). To give just a taste of the information available from a transient reflectance experiment, it is necessary to understand where the reflectivity changes induced by light irradiation come from. To give a simple introduction to this huge family of experiments, we follow the approach suggested by Zieger[4]. If R is the unperturbed reflectance, the fractional changes of reflectance after irradiation can be written: $\frac{\Delta R(t)}{R} = \frac{1}{R}(\frac{dR}{dn}n(t) + \frac{dR}{dT_E}\Delta T_E(t) + \frac{dR}{dQ}Q(t) + \frac{dR}{dT_l}\Delta T_l(t))$. Here the first term accounts for the electron excited in the conduction band, the second one for the changes in the electronic temperature, the third for the lattice displacement[2], and the fourth for the variation in lattice temperature[3]. The timescales for the electronic and lattice thermalization are expected to be different and, as will be seen in chapter 5, this will allow us to distinguish between the two. Nevertheless, it must be made clear that disentangling the different contributions is not always easy, and usually requires a model based on a series of assumptions suitable for describing the physics of the investigated system.

[2]This term is generally used to describe the "Coherent Phonon excitation". The 'sudden' displacement of the atoms from their equilibrium position (through different suggested mechanisms, DECP[4], ISRS[16], or others[9]) will force the atoms to oscillate in phase around the equilibrium position, which would modulate the reflectivity with the frequency of the vibrational eigenmode.

[3]The last term is not present in Zeiger approach and it has been added for clarity

1.3.2 "Material" Physics

Low Dimensional Magnetic Systems

The understanding of low dimensional magnetic systems is a topic of major interest for the condensed matter physicist in the last years. The effect of the reduced dimensionality on magnetic systems gives life to a novel branch of physics, whose properties, dominated by quantum fluctuation and non-thermal disorder, are far from being completely understood. The theoretical bottom line to study the low dimensional system is the Mermin-Wagner theorem. It states that continuous symmetries cannot be spontaneously broken at a finite temperature in one and two dimensions. This is because if such a spontaneous symmetry breaking occurred, then the corresponding Goldstone bosons, being massless, would have an infrared divergent correlation function. Intuitively, this means that long-range fluctuations can be created with little energy cost and since they increase the entropy they are favored, and therefore they would destroy the order. As an example, Heisenberg spin systems, where the interaction Hamiltonian is $S_i \cdot S_j$, the field excitations are called spin waves and can be recognized as Goldstone bosons. The excitation spectra of spin waves is gapless. It can be shown that for these excitations spectra fluctuations would destroy the order in 1 dimension and would allow a 2 dimensional order only at T=0. On the other hand the three dimensional order would be allowed. A formal description of the Mermin-Wagner theorem goes beyond the purpose of this introduction and can be found elsewhere[9].

The central part of chapter two (and partially chapter three) deals with magnetic systems where the interactions are of quasi-one-dimensional nature. As for this introduction, the aim is simply to point out how fluctuations can play a key role in determining the properties of quasi-one/two-dimensional systems.

Landau theory of phase transitions

It is worth including in the theoretical prerequisites of this thesis a short introduction to the Landau theory of phase transitions. In chapter 2 we shall make use of the Landau theory to together with some symmetry arguments to explain the first order character of the temperature induced structural phase transition in the borates family. We shall also rely on the Landau theory of phase transitions in Chapter 5 to discuss phonon screening by an excited electron/hole plasma. The phonon softening observed will be proposed as a precursor of an optically induced phase transformation and discussed in the spirit of the Landau theory.

The Landau theory assumes that the free energy of a system is determined by some parameters called the order parameters, and can be expressed analytically in terms of the order parameters. The choice of the order parameters depends on the physics of the investigated system. As an example, in the cases investigated in chapter 2 and 5, the order parameter will be the distortion of the lattice[4]. Note

[4]The description of the dynamical distortion in chapter 5 will make use of two coupled order

that in spite of the different nature of the phenomena investigated in chapter 2 and in chapter 5, the description in terms of the Landau theory is "relatively" similar.

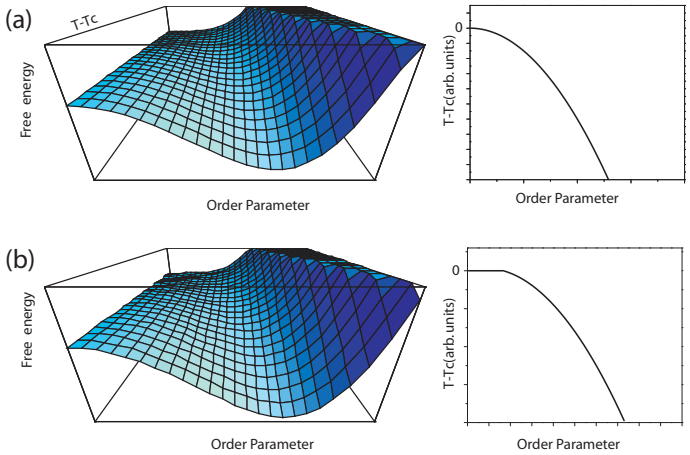

Figure 1.3: *Free energy in the Landau description, considering all the terms (b) and only the even ones (a). On the right a plot of the order parameter as a function of temperature is depicted for the two cases.*

At a finite temperature, the order parameter will have a certain value (ϵ_0) that minimizes the free energy, so that $F(\epsilon_0, T) \leq F(\epsilon, T)$ for any other $\epsilon \neq \epsilon_0$[5]. The appearance of a minimum of the free energy for different values of ϵ at different temperatures describes the system approaching a phase transition. The free energy of the system obeys two main requirements: it is analytic and it satisfies the symmetry requirements of the Hamiltonian. In the vicinity of the equilibrium position the free energy $F(\epsilon, T)$ can be expanded in power terms of the order parameter: $F(\epsilon, T) = q_0 + q_1\epsilon^2 + q_2\epsilon^3 + q_3\epsilon^4 + h.o.$ [6].

In general, all the expansion coefficients have to be taken into account but the symmetry requirements of the specific investigated problem can help in simplifying the description. The most common simplification is the case of a centrosymmetric Hamiltonian, where all the odd terms of the expansion vanish due

parameters, the distortion of the lattice and the number of electrons excited in the conduction band.

[5]The free energy should also contain an entropy term ($-TS(\epsilon, T)$), but for simplicity we assume that this term is constant at all ϵ - ie. this corresponds to the assumption that the volume and the number of particles are constant at different ϵ.

[6]The first term of the expansion is neglected due to the fact that ϵ_0 is an equilibrium position: $\frac{dF}{d\epsilon}(\epsilon_0) = 0$.

to symmetry reasons. In this case it is common to express the first term in the free energy's expansion as changing sign at the phase transition: $q_1 = a(T - T_0)$. Hence, the free energy minimum (the order parameter) approaches 0 continuously (Fig.1.3(a)), describing a second order phase transition. If the symmetry of the Hamiltonian allows the even terms of the expansion to be non-zero (as an example, see Appendix A, Chapter 2) the situation changes. The order parameter shows a discontinuity at T_c, as typical for 1^{st}-order phase transitions, and subsequently shifts as in 2^{nd}-order phase transitions (Fig.1.3(b)). This will be used in Chapter 2 to describe a "weak first-order" phase transition.

Magnons

A full description of magnetic excitations goes beyond the purpose of this thesis. Nevertheless, a general introduction on spin waves and magnetic excitation is necessary to understand the following chapters of this thesis and has therefore been included below.

As for lattice vibrations, where the notion of phonons as quantized lattice excitation has been introduced, a magnon is the quantized excitation of the magnetic system (the classical analogue is a spin wave). The simplest way to understand and visualize spin waves is to consider the Heisenberg Hamiltonian $H = -J \sum_{i,j} S_i \cdot S_j$. For $J > 0$ the energy is minimized when the spins on different atoms are oriented parallel to each other, with a total magnetic energy gain of $U = NJS^2$. Hence, as sketched in Fig.1.4(a), the ground state for $J > 0$ will be ferromagnetic ($|... \uparrow\uparrow\uparrow ... >$). Similarly it can be seen that $J < 0$ will give rise to an antiferromagnetic ordering ($|... \uparrow\downarrow\uparrow\downarrow ... >$, Fig.1.4(b)). In general the situation can be more complex: the anisotropy can be of a different nature and long range interaction can be relevant. In addition, in solids with different atomic species, multiple interactions are usually present, and in some cases an interaction can be even "frustrated", a term used to indicate that different interactions cannot be satisfied simultaneously. Therefore, it is natural to expect that a variety of different ground states could appear, ranging from canted antiferromagnet to sinusoidal order or spiral ordered states.

To introduce the spin wave calculation, we consider the ideal case of a one dimensional antiferromagnet sketched in Fig.1.4(a). The excitation spectra and the dispersion relations of an Heisenberg Hamiltonian, in the approach of [13, 14], are calculated starting from the equations of motion for the spin S_i at the site i. Assuming that the spins are aligned ($S_z = S$) and that $S_x, S_y << S_z$, the equation of motion for S_z is of second order in S_x, S_y and can be neglected. By transforming the equation of motion into the momentum, space it is possible to show that in the excited states the spins precess along the z-axis with the same frequency but different phase (Figure 1.4(c)). For an antiferromagnet, the situation is similar and the simultaneous treatment of the two magnetic sublattices is needed ($\uparrow$ and

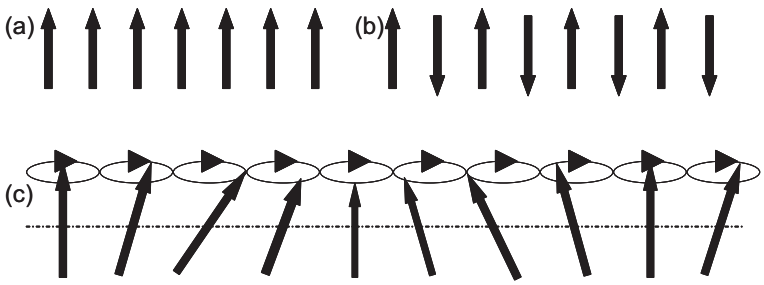

Figure 1.4: *Sketch of a ferromagnetic (a) and antiferromagnetic order (b). (c) Sketch of a spin wave excitation for a one dimensional ferromagnetic system.*

↓). It can be shown that the main difference is the appearance of an optical branch in the excitation spectra [4]. Further details on the spin wave calculation can be found elsewhere [19].

1.3.3 Summary

To summarize, the aim of this chapter was to help make the rest of this work more readable. We tried to put together a summary of background knowledge on different subjects in a simple and useful way for further reading. In the first part we gave a general motivation for this study, and a short introduction to every chapter. In the second half, we gave an overview of the theoretical foundation of the experimental techniques used and, at the same time, we tried to give the "flavor" of some of the problems investigated.

Bibliography

[1] V. Raman, Indian J. Phys. **2**, 387 (1938).

[2] H. Kuzmany, *Solid-State Spectroscopy* (Springer, Berlin, 1998).

[3] P. Atkins' and J. de Paula, *Physical Chemistry* (Oxford university press, Oxford, 2006).

[4] C. Kittel, *Introduction to Solid State Physisc* (John Wiley & Sons, New York, 1996).

[5] D. Komskii, *Quantum Solid State - Course Notes* .

[6] M. G. Cottam and D. J. Lockwood, *Light Scattering in Magnetic Solids* (JohnWilley & Sons, New York, 1986).

[7] P. Brüesch, *Light Scattering in Magnetic Solids* (JohnWilley & Sons, New York, 1986).

[8] R. Loudon, Proceedings of the Royal Society of London. Series A, Mathematical and Physical Sciences **275**, 218 (1963).

[9] N. D. Mermin, H. Wagner, Phys. Rev. Lett. **17**, 1133 (1966).

[10] R. Loudon, Advances in Physics **50**, 813-864 (2001).

[11] P. A. Fleury, S. P. S. Porto, L. E. Cheesman, H. J. Guggenheim, Phys. Rev. Lett. **17**, 84 (1966).

[12] P. A. Fleury, S. P. S. Porto, R. Loudon, Phys. Rev. Lett. **18**, 658 (1967).

[13] T. Holstein, H. Primakoff, Phys. Rev. **58**, 1098 (1940).

[14] F. Bloch, Z. Physik **61**, 206 (1930).

[15] D. M. Sagar, A. A. Tsvetkov, D. Fausti, S. van Smaalen, P. H. M. van Loosdrecht, JOURNAL OF PHYSICS - CONDENSED MATTER **19**, 346208 (2007).

[16] G. C. Cho, W. Kutt, H. Kurz, Phys. Rev. Lett. **65**, 764 (1990).

[17] C. V. Raman, *On the Molecular Scattering of Light in Water and the Colour of the Sea* (Proceedings of the Royal Society, 1922).

[18] W. Hayes and R. Loudon, *Scattering of light by crystals* (JohnWilley & Sons, New York, 1978).

[19] put toghether by A. Zheludev (2006), "http://neutron.ornl.gov/ zhelud/useful/dispforweb/index.html".

Chapter 2

About Phonons and Magnons in $RFe_3(BO_3)_4$

2.1 Introduction

The family of $RM_3(BO_3)_4$ crystals (R=Y or a rare earth, M=Al, Ga, Sc, Cr, Fe) has attracted considerable attention during the last years. Different combinations of R and M lead to a large variety of physical properties that, together with their excellent physical characteristics and chemical stability, make these crystals extremely interesting both from application and fundamental points of view. The lack of inversion symmetry has stimulated different applications in the field of optical and optoelectronic devices. Crystals of $YAl_3(BO_3)_4$ and $GdAl_3(BO_3)_4$ doped with Nd have been widely studied and used in optical devices, for self-frequency doubling and self-frequency summing lasers [1, 2, 3]. Concentrated $NdAl_3(BO_3)_4$ crystals are efficient media for mini-lasers [3]. Rare-earth borates with magnetic ions (M = Cr, Fe) are much less studied. Recently, some iron borates were reported to possess multiferroic features, demonstrating the coexistence of magnetic and ferroelectric order parameters [4]; they may therefore be considered for optoelectronic applications. These magnetic borates are also expected to exhibit interesting magnetic properties because of the presence of two different kinds of magnetic ions (3d and 4f elements), and in particular because their structure features isolated helicoidal chains of magnetic 3d atoms.

The crystal structure of $RM_3(BO_3)_4$ borates belongs to the structural type of the natural mineral huntite $CaMg_3(CO_3)_4$ that crystallizes in the space group $R32$ of the trigonal system [5, 6, 7, 8]. The primitive unit cell contains one formula unit. Three kinds of coordination polyhedra are present, trigonal prisms for RO_6, octahedra for MO_6, and two types of planar triangular BO_3 groups: equilateral $B1O_3$ and isosceles $B2O_3$ (the numbering of inequivalent ions position is the same as in Ref. [8]). The MO_6 octahedra share edges forming mutually independent

helicoidal chains which run parallel to the *c*-axis (see Fig.2.1). The RO_6 prisms are isolated polyhedra, each of them connects three helicoidal MO_6 chains, while there are no direct R-O-R links between different RO_6 prisms. This structure can also be seen as a succession of alternating BO_3 and R+M layers perpendicular to the c axis.

Recently, a systematic study of rare-earth iron borates $RFe_3(BO_3)_4$ (R = Y, La-Nd, Sm-Ho) was undertaken for polycrystalline samples [9]. The measurements of magnetization, specific heat, and ^{57}Fe Mössbauer spectra revealed an antiferromagnetic ordering at low temperatures. The magnetic ordering temperature increases with decreasing R^{3+} ionic radius, from 22 K for $LaFe_3(BO_3)_4$ to 40 K for $TbFe_3(BO_3)_4$. In addition to this, X-ray diffraction, specific heat measurements, and differential thermal analysis have indicated a structural phase transition for $RFe_3(BO_3)_4$ compounds with R = Eu-Ho, Y. Its temperature increases with decreasing R^{3+} ionic radius, from 88 K for $EuFe_3(BO_3)_4$ to 445 K for $YFe_3(BO_3)_4$. Magnetic ordering of the La- and Nd-iron borates has been confirmed by spectroscopic and magnetic measurements on non oriented single crystals [7, 10]. The most investigated compound of the family is the $GdFe_3(BO_3)_4$, a variety of techniques and methods have been employed to study the single crystal magnetic behavior [11, 12, 13, 4, 8, 14]. Recent specific heat, Raman scattering, and Nd^{3+} probe absorption measurements revealed a cascade of three spontaneous phase transitions in $GdFe_3(BO_3)_4$ [12]. A structural, weakly first-order, phase transition into a less symmetric low-temperature phase was found at T_S=156 K (this in contrast to the powder result T_S=174 K [9]). At lower temperature, two magnetic transitions have been observed. A second-order phase transition occurs at 37 K, resulting in an antiferromagnetic ordering of the Fe spin sublattice. This transition is accompanied by a polarization of the Gd spin subsystem. The second magnetic transition is observed at 9 K, and has been identified as a first-order Fe spin-reorientation transition [12]. A detailed picture of magnetic phase transitions in $GdFe_3(BO_3)_4$ as a function of temperature and magnetic field has recently been suggested in Ref. [13] on the basis of antiferromagnetic resonance studies.

This chapter is divided in two main part:

1. In the first part making use of **x-ray diffraction** we investigate the low temperature structure of $GdFe_3(BO_3)_4$, and we determine the symmetry of the low temperature phase. It is found that the LT-structure has the $P3_121$ symmetry

2. In the second part of the chapter we investigate **inelastic light scattering** on different compound of the $RFe_3(BO_3)_4$family (R=Gd, Nd, Er, Tb and Y). Two different aspects of the rare-earth iron borates are investigated. First, inelastic light scattering studies of the vibrational and structural properties of different $RFe_3(BO_3)_4$ are presented. This will confirm that the weak first-order phase transition from the high-temperature $R32$ structure to the low-temperature $P3_121$ (studied on $GdFe_3(BO_3)_4$) is a general characteristic of the whole family. The second part of this section focuses on the magnetic

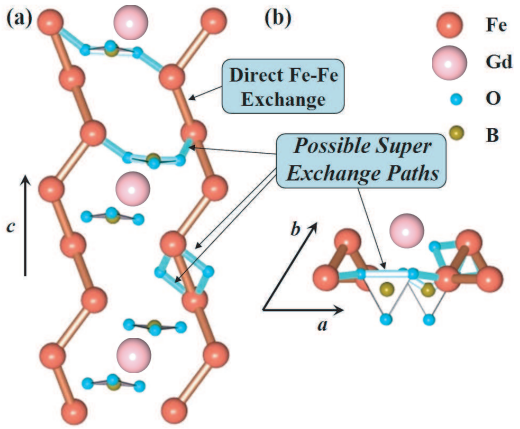

Figure 2.1: *The structure of $RM_3(BO_3)_4$ incorporates helicoidal chains of M^{3+} ions. The picture shows the structure of iron borates (M=Fe) viewed from different angles a) perpendicular to the C_3 axis and b) parallel to it. The possible exchange paths are shown.*

properties. Apart from observing changes in phonon frequencies at the antiferromagnetic ordering transition arising from magneto-elastic couplings, the spectra also exhibit relatively strong two-magnon scattering features. The magnetically ordered phases exhibits well defined magnon excitations resulting in a multiple peaked scattering continuum at finite energy. In the paramagnetic phase a strong low energy continuum is found, which results from the persistence of short range correlations in the helicoidal Fe spin chains up to quite high temperatures.

2.2 Low Temperature Structure Determination of $GdFe_3(BO_3)_4$

2.2.1 Experiment and result of structure determination

Crystals of $GdFe_3(BO_3)_4$ were grown using a $K_2Mo_3O_{10}$ - based flux, as described in Ref. [11]. Big transparent single crystals of gadolinium ferroborates were light green in color and had a good optical quality. A block-shaped crystal ('broken-fragment') with the dimensions of $0.22 \times 0.15 \times 0.11$ mm^3 was mounted on top of a glass fiber and aligned on a Bruker [27] SMART APEX CCD diffractometer. The crystal was cooled to 90(1) K using a Bruker KRYOFLEX. Intensity measurements were performed using graphite monochromated Mo-K$\bar{\alpha}$ radiation. Generator settings were 50 KV/ 40 mA. SMART [27] was used for preliminary determination of the unit cell constants and data collection control. The inten-

sities of reflections of a hemisphere were collected by a combination of 6 sets of exposures (frames). Each set had a different angle for the crystal and each exposure covered a range of 0.3° in ω. A total of 3600 frames were collected with an exposure time of 10.0 seconds per frame. The overall data collection time was 16 hours. Data integration and global cell refinement was performed with the program SAINT. The final unit cell was obtained from the xyz centroids of 4767 and 5439 reflections after integration for RT and 90 K, respectively. Intensity data were corrected for Lorentz and polarization effects, scale variation, for decay and absorption (an analytical absorption correction was applied), and reduced to F_o^2. The program suite SHELXTL was used for space group determination (XPREP).

At both temperatures of RT and 90 K the unit cell was identified as trigonal: reduced cell calculations did not indicate any higher metric lattice symmetry [29]. Space groups $R32$ and $P3_121$ were derived for RT and for 90 K, respectively, from the systematic extinctions and discriminated from other candidate space groups, which comply with the same extinctions conditions, during the structure determination process. Examination of the final atomic coordinates of the structure did not yield extra crystallographic or metric symmetry elements [30, 31].

The polarity of the structure of the crystal actually chosen was determined by Flack's **x**-refinement [32, 33, 34]; refinement resulted in a **x** value of 0.50(1), so ultimately an inversion twin is used in the refinement.

Crystal data and numerical details on data collection and refinement are given in Table 2.4. Final fractional atomic coordinates, equivalent displacement parameters and anisotropic displacement parameters are given in Table 2.5 for data at RT and in Table 2.6 for the 90 K data.

2.2.2 Discussion of the structure

The room temperature structure of $GdFe_3(BO_3)_4$ belongs to the $R32$ space group (Fig. 2.2 (a) and 2.2(b)). Our measurement confirms the structure reported previously for powder samples [5] and for several single crystals [6, 7] from the family $RFe_3(BO_3)_4$. The structure consists of alternating layers (parallel to ab-plane) of Fe-Gd and BO_3 groups (see Fig.2.2(b)). The main features of this structure are already described in literature [7]: the BO_3 groups are arranged in layers nearly perpendicular to the C_3 axis and the Fe atoms are arranged in helicoidal chains parallel to this axis. Different chains are connected by GdO_6 and BO_3 groups, where each individual BO_3 and GdO_6 group connects three chains. The distance between Fe atoms in the same chain (3.1669(4) Å) is shorter than the Fe-Fe distances for two nearest chains, that varies along the chain, 4.8308(5) Å, being the shortest one. The main exchange interaction between Fe^{3+} is therefore of quasi-1D nature.

Upon lowering the temperature the $GdFe_3(BO_3)_4$ crystal reduces the symmetry from $R32$ to $P3_121$, in the trigonal system. Fig. 2.3 shows the coordination polyhedra (GdO_6, FeO_6, and BO_3) for two different structures $R32$ and $P3_121$. At RT the BO_3 groups occupy two inequivalent positions, B1 (D_3) and B2 (C_2).

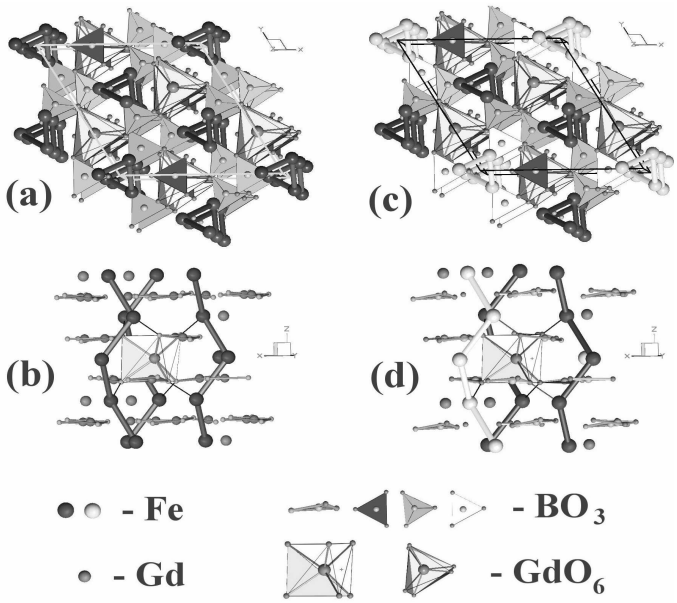

Figure 2.2: *The structure of $GdFe_3(BO_3)_4$ in two different projection. The left panels (a) and (b) show the RT structure, and the right panels (c) and (d) show the structure at 90 K. The Fe atoms are arranged in chiral chains parallel to the **c**-axis. Different chains are separated by GdO_6 prisms and BO_3 groups. The unit cell outline for R32 is shifted by (1/3, 1/3, 0) for comparison with the LT $P3_121$ structure. The two inequivalent chains are depicted in (d), the elongated Fe-Fe bond is depicted in white and the compressed one in black.*

At 90 K the site symmetry of the B1 atoms is reduced to C_2, whereas the site symmetry of the B2 atoms differentiates into a B2b (C_2) and B2a (C_1) (see also Table 2.1). In the LT-phase, the angle between BO_3 groups and ***c***-axis is changed. Moreover, in the LT-phase the BO_3 groups in C_1 position are considerably distorted and no longer flat (see Tab.2.1).

Concerning the magnetic structure, the main peculiarity of both the RT and the 90 K structures is the existence of magnetically quasi-1D helicoidal iron chains (see Fig. 2.2). The intra-chain exchange interaction between the Fe ions is expected to be dominated by Fe-Fe direct exchange and Fe-O-Fe superexchange, depending respectively on Fe-Fe distance and two Fe-O-Fe angles (Fig.2.4). Nevertheless there are some significant differences.

At RT all the Fe atoms are in equivalent positions (C_2). All Fe-chains are equivalent as are the Fe-O-Fe angles (102.40°(12) and 103.65°(8)) and Fe-Fe distances (3.1669(4) Å). Therefore, the exchange interactions between neighboring iron ions within a chain are also equivalent. At LT (Fig. 2.2), as shown in Table 2.1, the BO_3 groups form one general triangle (gray C_1 position) and two isosceles

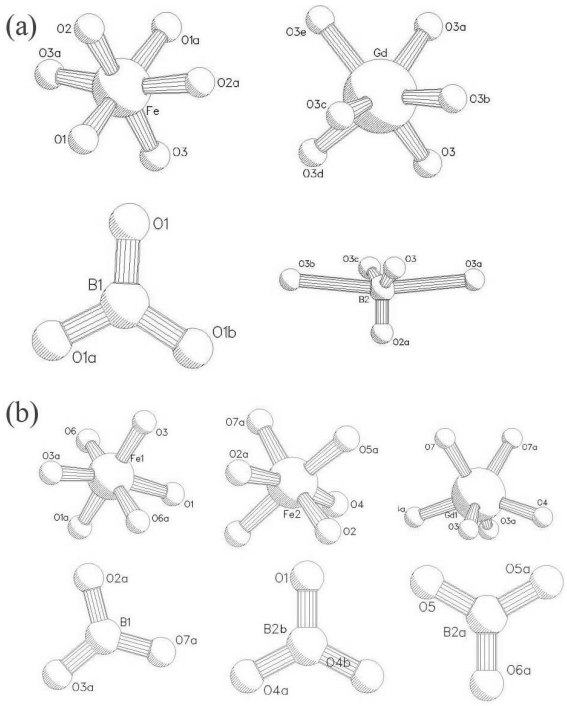

Figure 2.3: *Coordination polyhedra for the RT (R32-(a)) and the LT ($P3_121$-(b)) structures of $GdFe_3(BO_3)_4$. At RT the Fe atoms with C_2-symmetry are coordinated by three different types of oxygen atoms. AT 90 K there are two inequivalent positions for the Fe atoms: Fe1 (the same symmetry as RT) and Fe2, which is in a general position (surrounded by five different types of oxygen). At RT the Gd atoms are surrounded by six oxygens of one type (D_3-symmetry). At 90 K they are coordinated by three different types of oxygen atoms (C_2-symmetry). For the B atoms there are two kinds of coordination at RT. B1 (in D_3-symmetry) is surrounded by three oxygen atoms of the same type, the $B1O_3$-group is thus an equilateral triangle. The B2 atoms are surrounded by two types of O, $B2O_3$ is an isosceles triangle (C_2-symmetry). At 90 K there are three kinds of coordinations for the B atoms: $B2bO_3$ and $B1O_3$ are isosceles triangles (C_2 symmetry) and $B2aO_3$ is general triangle.*

triangles (white and dark, C_2 position). At RT "gray" and "white" groups become also equivalent, with C_2 symmetry, and the "dark" one is a regular triangle with the D_3 symmetry. The reduction of the symmetry of the borate groups changes the surrounding of the Fe atoms (Fig. 2.3), yielding two inequivalent positions (C_2 and C_1). Therefore, the Fe-Fe distances are different for the two chains: one is stretched (3.1828(4) Å) and in the other one is compressed (3.1554(4) Å). The angles Fe-O-Fe for the first chain are 101.24°(5) and 103.71°(9), while those for the second are 102.46°(6) and 103.91°(8). Therefore also the intra-chain exchange

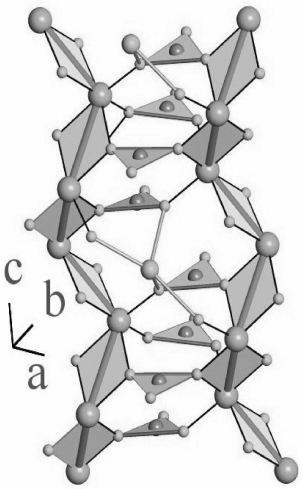

Figure 2.4: *Two Fe-chains and the most important exchange paths: the intra-chain exchange is via Fe-Fe direct exchange or Fe-O-Fe super-exchange, while the inter-chain exchange is through Fe-O-Gd-O-Fe and Fe-O-O-Fe.*

interaction is different for the two chains.

The GdO_6 prism connects three chains, one containing Fe1-atoms with C_2 symmetry and two with Fe2-atoms in a general position. There is only one inequivalent position for the Gd-ions in both the RT and the 90 K structures. However, the site symmetry of the Gd-ions changes from D_3 at RT to C_2 at 90 K. This confirms the interpretation of the authors of Ref. [12], who interpreted low-temperature infrared spectra of $Nd_{0.01}Gd_{0.99}Fe_3(BO_3)_4$ in terms of Kramers doublets of Nd, assuming only one structural position for the Nd ions.

The detailed structure of the Fe-chains and their interconnection are shown in Fig. 2.4. The intra-chain interactions between Fe-atoms go through two Fe-O-Fe superexchange pathways. The magnetic inter-chain interaction arises from the Fe-O-O-Fe, and possibly the Fe-O-Gd-O-Fe superexchange path. The role of the first superexchange path is important because the substitution of Gd for

Table 2.1: *Symmetry position of BO_3 groups, angle between the group and the **c**-axis and their flatness of them The flatness is expressed as distance of the B atoms from the plane defined by the three oxygen ligands.*

	Room Temperature				Low Temperature		
	Symmetry	Angle [degrees]	Flatness		Symmetry	Angle [degrees]	Flatness
B1	D_3	90	0	B1	C_2	87.52(4)	0.00002(4)
B2	C_2	84.37(11)	0	B2a	C_1	81.89	0.0055(11)
				B2b	C_2	83.55	0.0000(2)

non-magnetic Y does not lead to a disappearance of 3D magnetic ordering. On the contrary, the Néel temperature for $YFe_3(BO_3)_4$, T_{N1}=40 K, is larger than the one found for Gd-compound (T_{N1}=37 K), and for $NdFe_3(BO_3)_4$ (T_{N1}=30 K) [10]. Considering the different RE^{3+} ionic radii (0.983 Å for Nd, 0.938 Å for Gd, and 0.900 Å for Y) it is clear that the Neél temperature of $RFe_3(BO_3)_4$ depends strongly on the ionic radii: a smaller ionic radius results in a higher T_{N1}. Moreover, T_{N1} does not seem to be affected by the spin of the RE. In this sense it is clear that the main superexchange path of the interaction between different chains is the Fe-O-O-Fe path, and that a small distortion of this path changes substantially the magnetic properties of the system. It is therefore clear that the existence of two nonequivalent Fe chains with different Fe-Fe distances and Fe-O-Fe angles could lead to substantially different intra-chain exchange constant for the two chains [35], therefore it should be taken into account for the interpretation of the magnetic properties.

2.3 Raman scattering from phonons and magnons in $RFe_3(BO_3)_4$

2.3.1 Experimental Details

Different samples of $RFe_3(BO_3)_4$, with R = Gd, Nd, Tb, Er, and Y were grown using a $Bi_2Mo_3O_{12}$ - based flux, as described in Ref. [16, 17]. Unlike the Bi_2O_3 based fluxes [7], in $Bi_2Mo_3O_{12}$ - based flux Bi_2O_3 is strongly bonded to MoO_3 which excludes a partial substitution of bismuth for a rare earth during crystallization. Spontaneous nucleation from the flux resulted in small single crystals (1x1x1 mm). We used these crystals as seeds to grow large (10x5x5 mm) single crystals of Gd, Nd, and Tb iron borates. As for $ErFe_3(BO_3)_4$ and $YFe_3(BO_3)_4$, only small single crystals of these compounds were studied in this work. All the crystals were green in color. The samples were oriented either by X-ray diffraction technique or by using their morphology and optical polarization methods.

The Raman measurements were performed in a backscattering configuration, using a three-grating micro-Raman spectrometer (T64000 Jobin Yvon) equipped with a liquid nitrogen cooled charged coupled device (CCD) detector. The frequency resolution was better that 1 cm^{-1} for the frequency region considered. The samples were placed in a optical microscope cryostat. The temperature was varied from 2.7 to 500 K, with a stability of $\pm$0.02 K. The scattering was excited by the second harmonic light of a Nd:YVO_4 laser (532 nm), focused down to $\sim$50 μm^2 with the power density on the sample kept below 0.1 $mW/\mu m^2$. The polarization was controlled both on the incoming and outgoing beams giving access to all relevant polarization combinations.

Most of the experiments were performed with light incident perpendicular to the C_3-axis of the crystal, $\vec{k} \perp c$ (as a rule, precise orientation of $\vec{k}$ in the (ab)-plane was not known), however, when the shape of the samples allowed, also

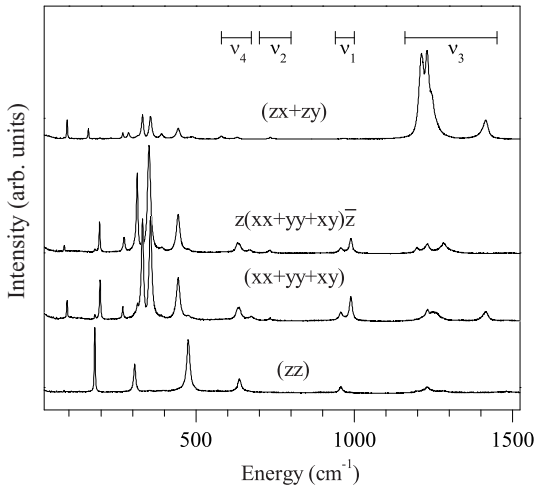

Figure 2.5: *Polarized Raman spectra of $GdFe_3(BO_3)_4$ at room temperature. The bars at the top indicate the frequency regions for the internal vibrations of BO_3 groups.*

the $\vec{k}||c$ configuration has been employed. Spectra are marked using the Porto notation [18]. For $\vec{k} \perp c$, only the polarization of incident and scattered light are indicated. The conventions z||C_3, x||C_2 are used to describe the geometry of the Raman experiments. Due to low sample quality, we were able to obtain only partially polarized Raman spectra of $ErFe_3(BO_3)_4$ and $YFe_3(BO_3)_4$.

Preliminary dielectric measurements were performed for $RFe_3(BO_3)_4$ on non oriented crystals of typical size 1x1x0.2 mm^3. The surfaces were polished and covered with Ag paste and the electrical contacts were made using Pt wires connected to the surface by additional Ag paste. The samples were mounted on a home-made insert for a Quantum Design PPMS system. The capacitance was measured using a Andeen-Hagerling AH2500A capacitance bridge operating at a fixed frequency of 1kHz.

2.3.2 Experimental Results

The room-temperature (RT) spectra of $GdFe_3(BO_3)_4$ for all studied experimental configurations are presented in Fig.2.5. The regions where the internal BO_3 vibrations are expected are indicated by the horizontal bars in the top of the panel. The spectra show a strong dependence on the polarization of the incoming and scattered light, but also show a distinct difference between (xx+yy+xy) polarized spectra for $\vec{k}$ parallel to c and for $\vec{k}$ perpendicular to c. The spectra for different rare earth iron borates are, as expected, qualitatively quite similar, as is shown in Fig.2.6.

The phonon lines narrow progressively with lowering the temperature and sev-

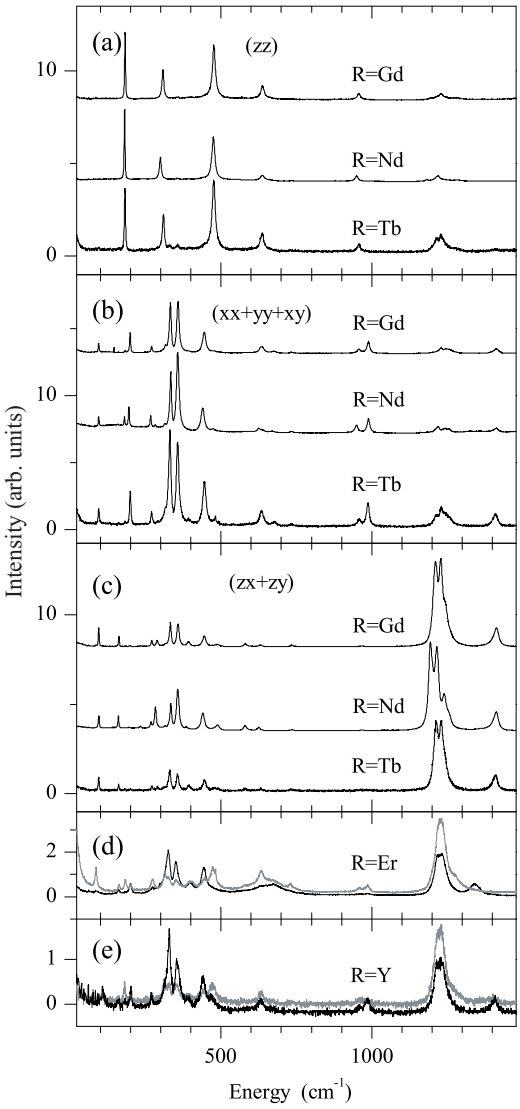

Figure 2.6: *(a, b, c) Polarized Raman spectra for $RFe_3(BO_3)_4$, R=Gd, Nd, Tb, at room temperature. (d,e) Partially polarized Raman spectra for (d) $ErFe_3(BO_3)_4$ at 390 K and (e) $YFe_3(BO_3)_4$ at 420 K.*

eral new modes appear abruptly in $GdFe_3(BO_3)_4$, $TbFe_3(BO_3)_4$, $ErFe_3(BO_3)_4$, and $ErFe_3(BO_3)_4$, at T_S=155 K, 198 K, 340 K, and 350 K, respectively. Figures 2.7 and 2.8 and Tab. 2.7 give a detailed comparative picture of the phonon modes observed above and below T_S in $RFe_3(BO_3)_4$. The intensities of the new modes show a hysteresis as a function of temperature (see Fig.2.9). The lowest-frequency intense new mode appears abruptly below the phase transition, but then exhibits a soft-mode-like behavior with further lowering of the temperature; i.e.

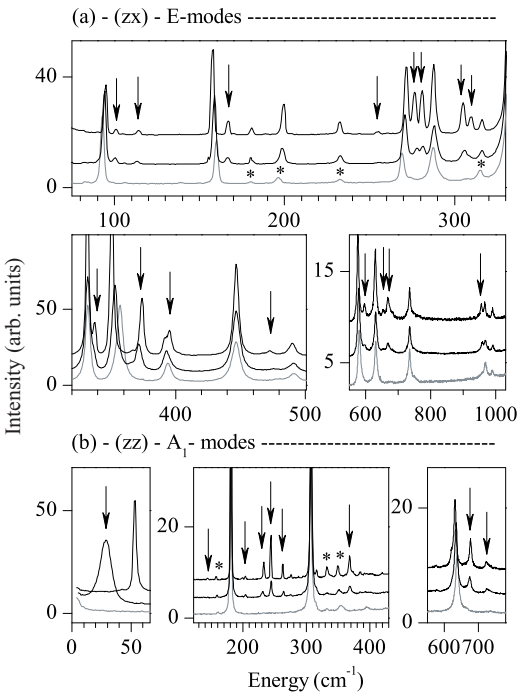

Figure 2.7: *Raman spectra of $GdFe_3(BO_3)_4$ above and below T_s=156 K, namely, at 161 K (the lowest traces in each panel), 150 K (middle traces), and 30 K (upper traces). (a) (zx+zy) polarization; (b) (zz) polarization. New modes that appear below T_s are indicated by arrows. Asterisks mark the lines from another polarization.*

for $GdFe_3(BO_3)_4$ and $TbFe_3(BO_3)_4$ the low frequency mode shifts from 26 cm^{-1} at T_S to respectively 56 cm^{-1} and 57 cm^{-1} at 3 K, and for $ErFe_3(BO_3)_4$ and $YFe_3(BO_3)_4$ it goes respectively from 25 to 72 cm^{-1} and from 27 to 76 cm^{-1}. At the same time its linewidth decreases from 12 to 3 cm^{-1} (see Figs.2.10). The spectra in (xz+yz) polarization of all the compounds demonstrate a low-frequency scattering continuum that gradually changes its shape with lowering the temperature and exhibits the opening of a "gap" at T_N (see Fig.2.11). For $NdFe_3(BO_3)_4$ at the lowest temperatures a well-defined narrow peak at about 10 cm^{-1} is observed within the gap. This mode shifts to zero frequency and strongly broadens upon approaching T_N from below (Fig.2.11(c)). For the Gd compound a similar mode is observed below T_N at about 18 cm^{-1}.

2.3.3 Group-Theoretical Analysis

High-temperature structure $R32$ (D_3^7)

The primitive cell of the high-temperature structure $R32$ of $RFe_3(BO_3)_4$ contains 20 atoms which results in 57 vibrational normal modes. Knowing the local symmetry of all the atomic positions, one can perform the factor-group analysis to find the symmetries of these modes [19, 18]. R and B1 atoms reside in highly

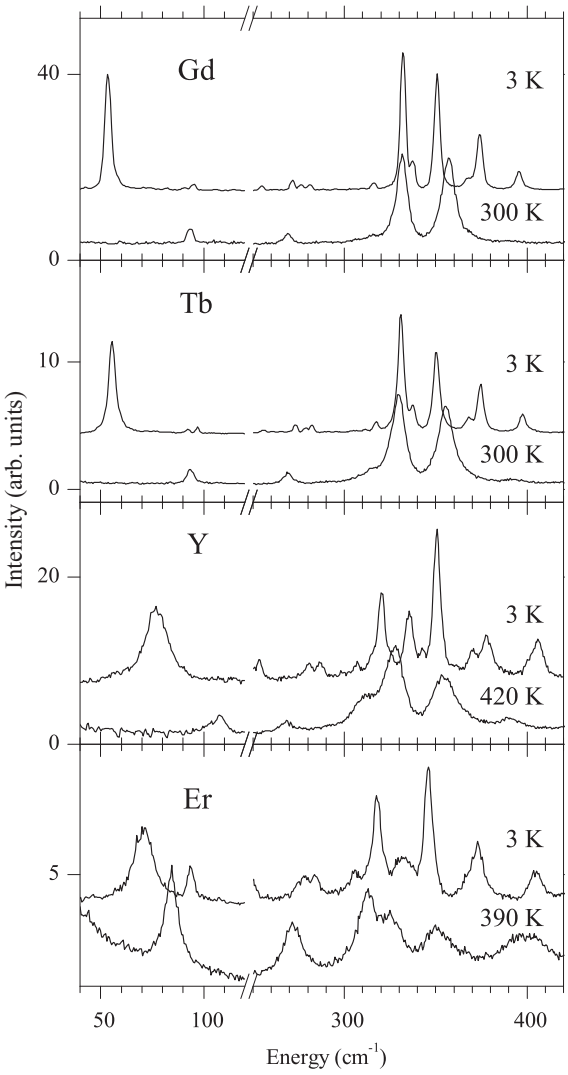

Figure 2.8: *Comparison of several low-temperature new modes in different $RFe_3(BO_3)_4$. Spectra in (xx+xy)-polarization for R=Gd and Tb and partially polarized spectra for R=Y and Er.*

symmetric D_3 positions [7, 8] and generate $A_2 \oplus E$ modes each. Fe, B2, O1, and O2 atoms are in C_2 symmetry positions, which results in $A_1 \oplus 2A_2 \oplus 3E$ modes for each of them. O3 atoms occupy general C_1 positions and give $3A_1 \oplus 3A_2 \oplus 6E$ modes. Summing all these modes and subtracting the $A_2 \oplus E$ acoustic modes one gets the following optical vibrational modes of the crystal, in accordance with the results of Ref.[15].

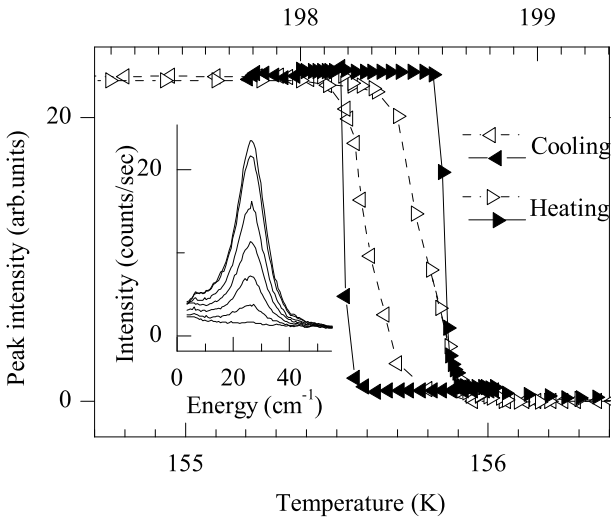

Figure 2.9: *The lowest-frequency A_1-mode appearing in low-temperature $P3_121$ structure demonstrates hysteresis in a plot of its intensity vs temperature. The data for Gd(Tb)-compound are presented by open (black) triangles. Inset shows this mode during cooling down for temperatures 154.91, 155.03, 155.08, 155.11, 155.16, 155.20, 155.45 K in Gd-compound. The lower temperature axis refer to R=Gd, the upper one - to Tb.*

$$\Gamma_{vibr} = 7A_1(\mathrm{xx,yy,zz}) \oplus 12A_2(E//\mathrm{z}) \\ \oplus 19E(E//\mathrm{x}, E//\mathrm{y}, \mathrm{xz,yz,xy}) \tag{2.1}$$

Notations in parentheses refer to the allowed components of electric dipole moment (infrared (IR) activity) and the polarizability tensor (Raman activity). Doubly degenerated E modes are polar and both IR and Raman active. The light propagating along the c-axis ($\vec{k}||c$) probes TO modes, while the $\vec{k}\perp c$ configuration gives pure LO modes [15].

The strongest bonds in the structure of $RFe_3(BO_3)_4$ borates are B-O bonds within the planar BO_3 triangles. Considering them as molecular units that occupy D_3 (for $B1O_3$) and C_2 (for $B2O_3$) positions, and adding the modes of translational character coming from R and Fe ions (respectively in D_3 and C_2 position), we obtain the following optical modes:

$$\Gamma_{vib}^{tr} = 2A_1 \oplus 5A_2 \oplus 7E; \quad \Gamma_{vib}^{lib} = A_1 \oplus 3A_2 \oplus 4E, \tag{2.2}$$

where the librational ones (right equation) come from the BO_3 units. The total number of external optical vibrations is, thus,

$$\Gamma_{vib}^{ext} = 3A_1 \oplus 8A_2 \oplus 11E \tag{2.3}$$

Subtracting (2.2) from (2.1), one gets the internal vibrational modes related to the vibrations of BO_3 groups:

$$\Gamma_{vib}^{int} = 4A_1 \oplus 4A_2 \oplus 8E \tag{2.4}$$

The correlation scheme of Fig.2.12 helps to get a deeper insight into the origin of the vibrational modes of $RFe_3(BO_3)_4$. It follows from this scheme that two of the seven A_1 modes originate from the fully symmetric vibration of the $B1O_3$ and $B2O_3$ groups, two correspond to the $B2O_3$ ν_3 and ν_4 vibrations, and two to the rotational and translational modes of the $B2O_3$ group. The remaining A_1 mode results from displacements of the iron atom. Table 2.2 indicates the origin of crystal modes in the frequency ranges of internal vibrations of the BO_3 molecules.

Low-temperature structure $P3_121(D_3^4)$

The primitive cell of the low temperature structure contains three formula units [8] (60 atoms) which gives 177 vibrational modes. Unique positions for the R and B1 atoms remain but their symmetry lowers from D_3 in the $R32$ structure to C_2 in the $P3_121$ one. On the contrary, instead of single threefold C_2 symmetry positions for Fe, B2, O1, and O2 there are now two different positions, namely, a threefold C_2 and a sixfold C_1 positions for each of them. O3 oxygen atoms occupy now three different general (C_1) positions [8]. The factor-group analysis of the low-temperature structure $P3_121$ gives the following optical vibrational modes:

$$\Gamma_{vib}(P3_121) = 27A_1 \oplus 32A_2 \oplus 59E \tag{2.5}$$

Carrying out the same procedure as in the previous subsection one finds what modes correspond to the external (translational and librational) motions of the R and Fe atoms and of the BO_3 entities and to the internal vibrations of the BO_3 "molecules". The results are summarized in Table 2.3.

Table 2.2: *Frequency range and assignment of the vibrations of the BO_3-group. The second column lists the assignments for the free ions. The third column shows the expected internal modes and their symmetries in the high temperature phase of the rare-earth iron borates (the superscripts 1 and 2 refer to the different borate groups in the rare-earth iron borates).*

Frequency range (cm^{-1})	BO_3 vibrations (D_{3h})	Crystal vibrations
600	$\nu_4(E')$ in-plane bending	$\nu_4^{(2)}(A_1) + \nu_4^{(1)}(E) + 2\nu_4^{(2)}(E)$
700-800	$\nu_2(A_2'')$	$\nu_2^{(2)}(E)$
950	$\nu_1(A_1')$ symmetric breathing	$\nu_1^{(1)}(A_1) + \nu_1^{(2)}(A_1) + \nu_1^{(2)}(E)$
1250-1400	$\nu_3(E')$ asymmetric breathing	$\nu_3^{(2)}(A_1) + \nu_3^{(1)}(E) + \nu_3^{(2)}(E)$

2.3.4 Discussion

Phonons of $RFe_3(BO_3)_4$ in the $R32$ and $P3_121$ phases

First of all, we consider the polarized room-temperature Raman spectra of $RFe_3(BO_3)_4$, R=Nd, Gd, and Tb (Fig.3.5). Table 2.7 summarizes the observed Raman modes of these iron borates at RT. It has been constructed taking into account the results of the group-theoretical analysis for the $R32$ structure and the frequency ranges for normal modes of the regular planar free ion $(BO_3)^{3-}$ (they are indicated in Fig.3.4; see also Tables 2.2 and 2.3). The spectra of $ErFe_3(BO_3)_4$ and $YFe_3(BO_3)_4$ were only partially polarized. Comparing the 390 K spectra of $ErFe_3(BO_3)_4$ and the 420 K spectra of $YFe_3(BO_3)_4$ with the RT spectra of other iron borates we complete Table 2.7 for these compounds as well (at room temperature, $ErFe_3(BO_3)_4$ and $YFe_3(BO_3)_4$ are already in the low-temperature phase).

The low-frequency part of the Raman spectrum is dominated by external modes arising from translational motions of the R and Fe atoms and from librational and translational modes of BO_3 groups. The number and polarization properties of the modes observed below 500 cm^{-1} agree with the group-theoretical predictions. All the modes observed in the frequency ranges of the ν_4, ν_2, and ν_1 vibrations of BO_3 correspond well to those derived using the correlation analysis and summarized in Fig. 2.12. In contrast, there is one extra mode in the region of the ν_3 vibration. Possibly, the strong doublet at about 1220 cm^{-1} in the (zx+zy)-polarization arises due to the Fermi resonance [20] between the ν_3 vibrations and an overtone of the ν_4 vibration.

The highest vibrational frequency (originating from the ν_3 vibration of the BO_3 group) observed in $ErFe_3(BO_3)_4$ differs markedly from the highest frequencies of both TO ($\vec{k} \parallel c$) and LO ($\vec{k} \perp c$) phonons (1280 and 1414 cm-1, respectively, in $GdFe_3(BO_3)_4$). This is because in our particular non oriented $ErFe_3(BO_3)_4$ sample the direction of $\vec{k}$ was arbitrary, while the frequencies of polar E modes depend on the direction of $\vec{k}$.

Table 2.3: *The origin of vibrations for two structural modifications of $RFe_3(BO_3)_4$ and the new modes that should appear below the temperature of the structural phase transition T_s.*

species	$T > T_s$: $R32$ (D_3^7)	$T < T_s$: $P3_121$ (D_3^4)	New modes
R	$A_2 \oplus E$	$A_1 \oplus 2A_2 \oplus 3E$	$A_1 \oplus 2E \oplus A_2$
Fe	$A_1 \oplus 2A_2 \oplus 3E$	$4A_1 \oplus 5A_2 \oplus 9E$	$3A_1 \oplus 6E \oplus 3A_2$
external BO_3			
translational	$A_1 \oplus 3A_2 \oplus 4E$	$5A_1 \oplus 7A_2 \oplus 12E$	$4A_1 \oplus 8E \oplus 4A_2$
librational	$A_1 \oplus 3A_2 \oplus 4E$	$5A_1 \oplus 7A_2 \oplus 12E$	$4A_1 \oplus 8E \oplus 4A_2$
internal BO_3	$4A_1 \oplus 4A_2 \oplus 8E$	$12A_1 \oplus 12A_2 \oplus 24E$	$8A_1 \oplus 16E \oplus 8A_2$
Total	$7A_1 \oplus 13A_2 \oplus 20E$	$27A_1 \oplus 33A_2 \oplus 60E$	$20A_1 \oplus 40E \oplus 20A_2$

Summarizing the RT results, it is concluded that (i) the number and symmetries of the Raman modes observed for the $RFe_3(BO_3)_4$ in the high-temperature phase are fully consistent with the predictions of group-theoretical analysis based on the $R32$ space group; (ii) the modes above $\sim$550 cm^{-1} originate from the internal vibrations of the BO_3 groups, while those below $\sim$550 cm^{-1} can be considered as external modes.

In the low-temperature $P3_121$ phase, 20 A_1 (12 external and 8 internal) and 40 E (24 external an 16 internal) new modes should appear, according to the results of the group-theoretical analysis (see Table 2.3). These new modes arise due to two reasons. First, the symmetries of the local positions for some of the atoms reduce. The intensity of these new modes should be proportional to the deviation from the former symmetric position. Second, the primitive cell contains now not one but three formula units, leading to an additional Davydov (factor-group) splitting proportional to the strength of interaction between equivalent atoms inside the new primitive cell. Both these effects are, as a rule, small. That is why the number of the observed new modes ($10A_1 \oplus 18E$ in $GdFe_3(BO_3)_4$) is lower than the number predicted by group-theoretical analysis. The same new modes appear below T_s in all the compounds $RFe_3(BO_3)_4$, with R=Gd, Tb, Er, and Y (see Fig. 5 and the bottom of Table III), which strongly suggests the same $P3_121$ low-temperature structure in all of them.

Weak first-order structural phase transition

The most characteristic Raman feature that announces the phase transition from the high-temperature $R32$ structure to the low-temperature $P3_121$ one is the sudden appearance of a strong new low-frequency mode (see Figs.2.7, 2.9 and 2.10) in the Raman spectra. As the intensities of new modes are proportional to the squares of atomic displacements, $I \sim \delta^2$, the strongest new mode is believed to be associated with the biggest displacements. A detailed analysis, according to Ref. [8], of the structural changes shows that the biggest displacements are those associated with the BO_3 "molecules". In particular, BO_3 triangles, perpendicular to the C_3 axis in the $R32$ structure, tilt by $\sim 7^o$ in the $P3_121$ phase; the B1 atoms shift by $\sim$0.03 Å from the centers of regular triangles. The shifts of boron ions relative to neighboring oxygen ions create local dipole moments; their triangular arrangement corresponds to an antiferroelectric ordering below the temperature of the structural phase transition. This ordering manifests itself via a strong dielectric anomaly at T_S observed in our preliminary dielectric measurements (Fig. 2.13).

The structural changes considered above give rise to many new Raman active vibrational modes connected with the BO_3 groups (see Table 2.3), in particular, to $4A_1$ additional librational modes. The energy value of the intense excitation measured is in the typical range of the molecular librations. At 3 K, it is 56, 57, 72, and 76 cm^{-1} for Gd(157), Tb(159), Er(167), and Y(89) compounds, respectively. As the values for the Er and Y compounds are very close, notwithstanding a big

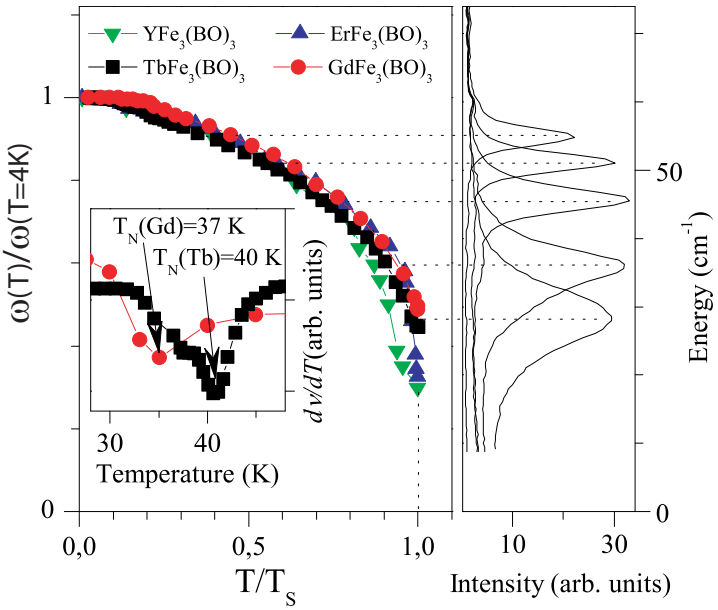

Figure 2.10: *The lowest-frequency mode appears at the phase transition at a finite frequency (characteristic of a first-order transition), but exhibits a high-frequency shift with further lowering the temperature (characteristic of a second-order transition). The inset shows the derivative of the peak frequency in the vicinity of the magnetic ordering temperature, evidencing the coupling of vibrational and magnetic degrees of freedom (see text for discussion).*

difference in atomic masses of Er and Y, we conclude that the rare earth does not take part in this lowest-frequency vibration. A difference between the values for the compounds with relatively big (Gd, Tb) and small (Er, Y) ions comes from the difference in interatomic distances and, hence, force constants. The ensemble of these observations strongly suggests that the phase transition in $RFe_3(BO_3)_4$ is correlated to a rotational mode of the BO_3 groups.

The abrupt appearance of new phonon modes and the hysteresis observed for their intensities when approaching T_S from different sides indicate the first-order character of the phase transition. The energy of the low frequency mode strongly increases upon lowering the temperature below T_S (Fig.2.10). At the lower temperature (3K) the frequency of the mode has more than doubled. Such an anomalously large shift is typical for soft modes that announce a second-order structural phase transition. Apparently, we deal with a so-called "weak first-order" phase transition. It is worth noting that the lowering of the symmetry from $R32$ (D_3^7) to $P3_121$ (D_3^4) is indeed also compatible with a second-order phase transition [21]. Thus, the observed first-order character of the phase transition does not depend on symmetry changes but rather can arise from the third order

therm in the Landau expansion of the crystal free energy h, allowed by the crystal symmetry, or from the negative sign of the fourth order coefficient u:

$$G = G_0 + rQ^2 + hQ^3 + uQ^4 + ..., \tag{2.6}$$

where Q is the order parameter [22].

Figure 2.14 shows the temperatures of the structural phase transition in $RFe_3(BO_3)_4$ plotted versus ionic radii of R^{3+}, as determined in Ref. [9] for powder samples and in the present study for single crystals. A mismatch between our data and those of Ref. [9] could arise from a rather poor quality of the Er and Y iron borate single crystals. A further study is necessary to clarify this question.

Finally we note that $NdFe_3(BO_3)_4$ preserves the $R32$ structure down to the lowest temperatures, while $RFe_3(BO_3)_4$ with R^{3+} smaller than Tb^{3+} have the low-temperature $P3_121$ structure already at room temperature.

Magnetoelastic coupling

The inset of Fig.2.10 shows the derivative of the peak frequency of the strongest new A_1 mode as a function of temperature in the vicinity of the magnetic ordering temperature T_N. The coupling of vibrational and magnetic degrees of freedom is evident. The discontinuity in the phonon frequency observed at $T = T_N$ is ascribed to magneto-elastic coupling. The magnetic ordering causes spontaneous magnetostriction, that is, atomic displacements. The latter, evidently, influence vibrational frequencies. Recently, Ref.[4] reported on the study of magnetoelectric and magnetoelastic properties of $GdFe_3(BO_3)_4$. A strict correlation between both has been shown experimentally and discussed theoretically. The authors of Ref.[4] assumed that, below T_N, the crystal symmetry lowers, due to magnetoelastic coupling with spontaneous magnetic moments lying in the ab-plane. This breaks the symmetry of the antiferroelectric arrangement of the electric dipole moments in the $P3_121$ structure and leads to the appearance of an electric polarization which could be responsible for the weak growth of the dielectric constant in the temperature region $T_R < T < T_N$ [4], (see also Fig. 2.13). The proposed lowering of crystal symmetry below T_N, however, should result in the appearance of new vibrational modes. No indications for additional modes below T_N have been found. This does not necessarily mean that the model by Zvezdin *et al.* is in error. It might very well be that the structural changes are simply too small to be detected by Raman scattering.

As Reference [4] suggests, the spin-reorientation first-order phase transition at T_R into the antiferromagnetic configuration of spins parallel to the c-axis recovers the $P3_121$ structure (that does not allow the presence of the electric dipole moment) and, therefore, is expected to be accompanied by a jump of the dielectric constant. As is clear from Fig. 2.13, the dielectric function indeed exhibits such a jump, thereby strongly supporting the suggested scenario.

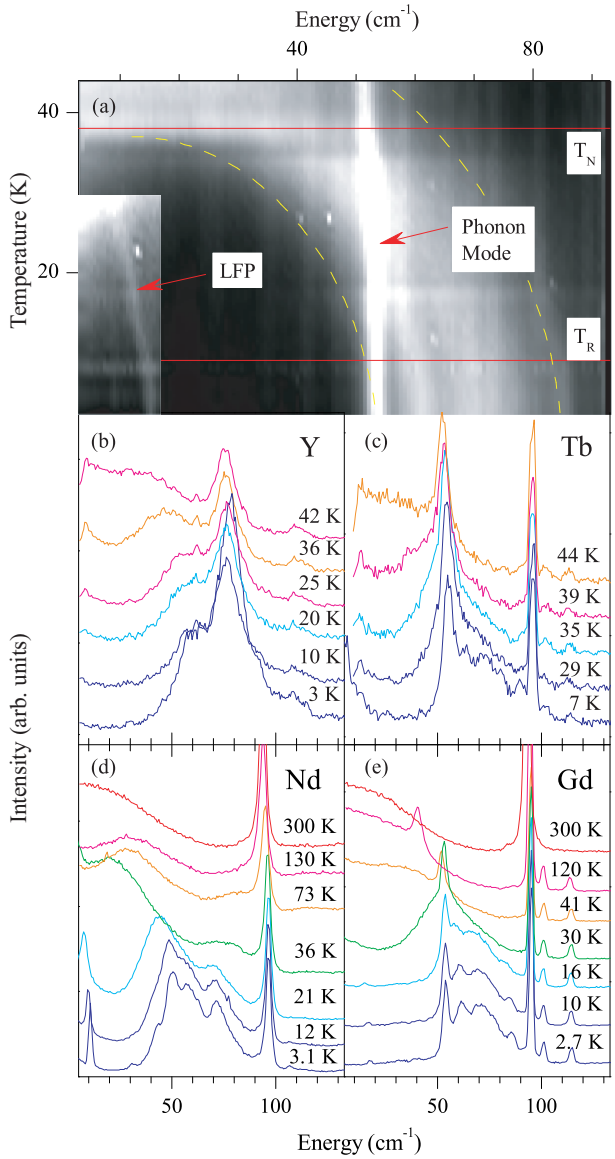

Figure 2.11: *Raman spectra of different $RFe_3(BO_3)_4$ collected in (xz+yz) polarization. The upper picture (a) shows the opening of a gap in the magnon Raman scattering at $T_N = 37K$ for $GdFe_3(BO_3)_4$ (the intensity scale of the left bottom corner of the picture is optimized to evidence the low-frequency mode, and the dotted lines are guides for evidencing the scattering features). The central picture (b,c) show the magnetic scattering around T_N for $YFe_3(BO_3)_4$ and $TbFe_3(BO_3)_4$. The lower one (d,e) shows the two-magnon spectra in the full temperature range ($2.7K < T < 300K$) for $NdFe_3(BO_3)_4$ on the left and for $GdFe_3(BO_3)_4$ on the right. For the Gd sample a phonon line is evident in proximity of the magnon feature. LFP indicates the low-frequency peak, see the text for the discussion. Above T_N the paramagnon scattering survives up to at least nearly ten times the ordering temperature. Different temperature measurements in the panels b,c,d,e are depicted with an arbitrary offset for clarity.*

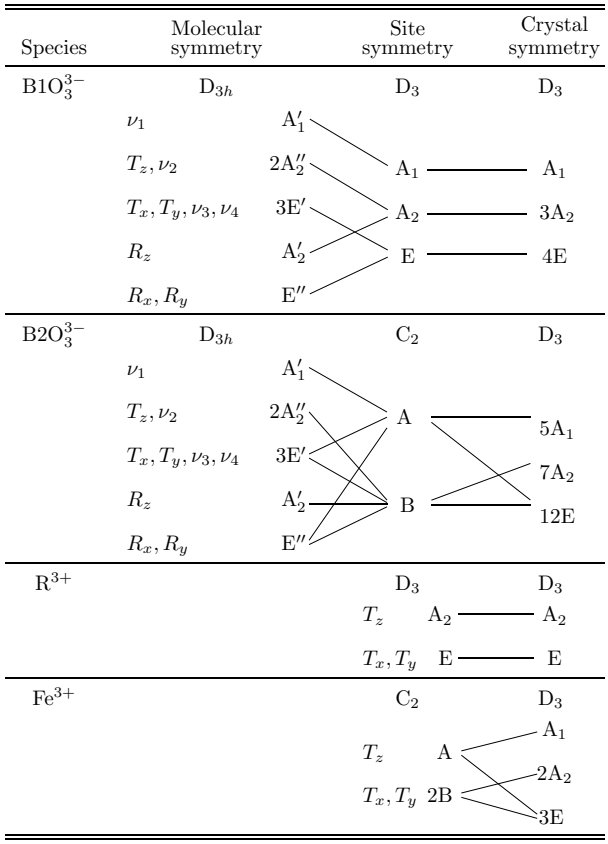

Figure 2.12: *Correlation scheme for vibrational modes of $RFe_3(BO_3)_4$, space group R32.*

2.3.5 Magnetic scattering

As discussed in the introduction, due to the structural properties of the $RFe_3(BO_3)_4$ family, Fe atoms (S=5/2) are arranged in helicoidal chains. As a result, the Fe-Fe distance inside the chain is substantially smaller than the distance between different chains. The main exchange interaction is therefore expected to be between Fe ions on the same chain ($J_{//} \rangle\rangle J_{\perp}$), suggesting that low dimensionality could play a crucial role in the magnetic properties of the family. This, together with the presence of two coupled magnetic sublattices makes the compounds with magnetic R^{3+} ions good candidates for exotic magnetic ground states.

A complex magnetic behavior has indeed been found and widely discussed in $GdFe_3(BO_3)_4$. The first magnetization measurements on oriented single crystals were interpreted under the assumption that both Fe and Gd subsystems order antiferromagnetically at T_N=40 K [11]. In this model, below 10 K, the total

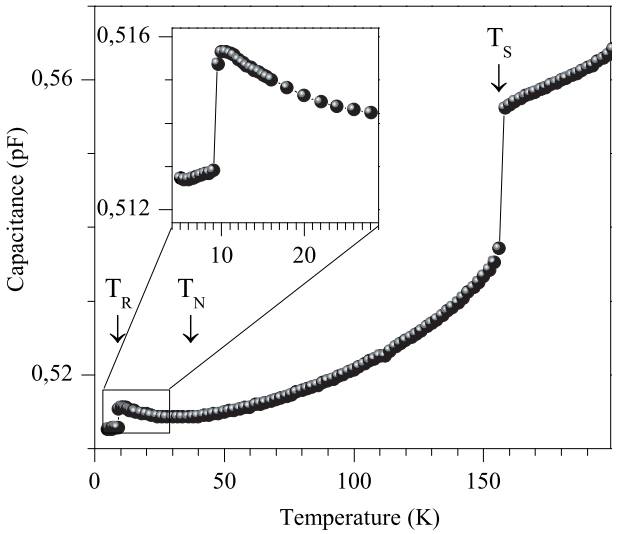

Figure 2.13: *Dielectric measurements of $GdFe_3(BO_3)_4$. The structural phase transition is made evident by a step in the capacitance at T_S. No evidence is found of the Fe ordering phase transition at T_N, while the capacitance shows a discontinuity at the spin-reorientation phase transition at T_R (displayed in more detail in the Inset).*

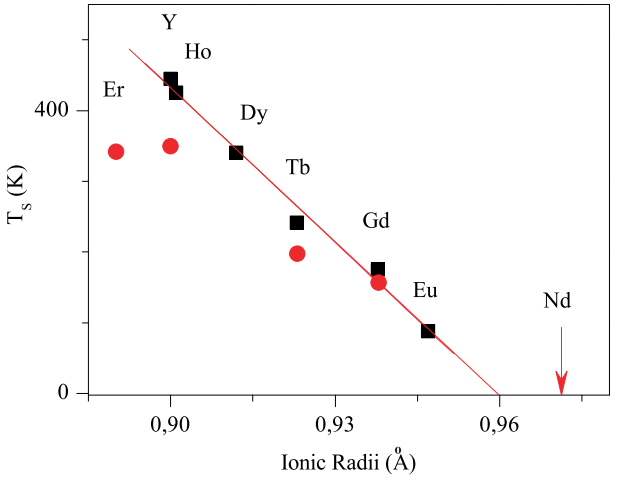

Figure 2.14: *(Color online) Temperatures of the structural phase transitions for different $RFe_3(BO_3)_4$ as a function of the ionic radius. Our data on single crystals are shown by circles, those of Ref. [9] on powder samples are presented by squares.*

magnetic moment of the three Fe sublattices (S = 5/2) oriented at polar angles $\sim 60^\circ$ to the c axis is compensated by the Gd moment (S = 7/2) oriented along the c axis. Sharp singularities in magnetization in the magnetic field H||c observed below 10 K were attributed to spin-flop transitions in the Fe subsystem. It was assumed further that in the range of temperatures between 10 and 40 K the magnetic moments of every Fe sublattice fall into the ab plane, perpendicular to the c axis, preserving the 120° azimuthal orientation.

This model was later reconsidered in Ref. [12]. It has been suggested, on the basis of the analysis of the Nd-probe spectra and of the specific heat data, that the Gd subsystem does not undergo a magnetic phase transition at T_N but only gets polarized by the Fe subsystem. The model summarized in Fig.2.15 has been put forward. At T_N=37 K, the iron magnetic moments order antiferromagnetically in the direction perpendicular to the c-axis and polarize the Gd subsystem. Below T_R=9 K, the magnetic moments order antiferromagnetically along the c-axis. The temperature T_R=9 K corresponds to a first-order spin-reorientation magnetic phase transition [12]. Simultaneously and independently, the same conclusion has been drawn in Ref.[13] where magnetic structures and magnetic phase transitions in $GdFe_3(BO_3)_4$ were studied using antiferromagnetic resonance experiments. This study revealed also a detailed picture of the magnetic structure and anisotropy for different magnetic phases in $GdFe_3(BO_3)_4$ as a function of both temperature and magnetic field. At T_N=38 K, the Fe magnetic subsystem orders into a two-sublattice collinear easy-plane antiferromagnet and polarizes the Gd spins, which also form a two-sublattice antiferromagnetic subsystem. The anisotropy constant of the Gd subsystem has an opposite sign to that of the Fe subsystem. The Gd contribution to the total anisotropy energy grows with lowering the temperature, in conjunction with the growing polarization of the Gd subsystem, and becomes appreciable below ∼20 K. At T_R=10 K the total energy of anisotropy changes its sign which results in the spontaneous spin reorientation transition.

The long-range order of the spins on the iron subsystem manifests itself in the inelastic light scattering experiments with two main features. The first one, as reported in Fig.2.11, is the arising of a low-frequency peak (LFP) at ∼10 cm^{-1} in $NdFe_3(BO_3)_4$ and at ∼18 cm^{-1} in $GdFe_3(BO_3)_4$. These peaks soften and broaden upon approaching T_N. The energy of 10 cm^{-1} in $NdFe_3(BO_3)_4$ has been identified, by absorption spectroscopy of Nd^{3+} crystal-field levels, as the exchange splitting energy of the Nd^{3+} ground Kramers doublet at 5 K arising from the interaction with the ordered Fe sublattice [10]. The temperature dependencies of the frequency and the linewidth of the Raman LFP are the same as those of the ground-state splitting and, respectively, the ground-level width found from optical spectroscopy [10]. Therefore the 10 cm^{-1} Raman mode observed in $NdFe_3(BO_3)_4$ is assigned to spin flip scattering on a single Nd^{3+} moment in the effective field created by the Fe sublattice. Most likely, the 18 cm^{-1} excitation observed in $GdFe_3(BO_3)_4$ has the same origin. The absence of LFP in Raman scattering of $YFe_3(BO_3)_4$ with nonmagnetic Y^{3+} (see Fig. 2.11) is in favor of such interpreta-

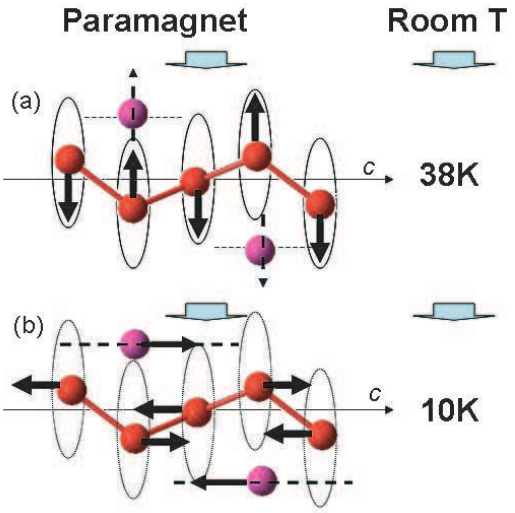

Figure 2.15: *Sketches of the magnetic phase of $GdFe_3(BO_3)_4$. (a) At 37K the Fe ions order antiferromagnetically with a easy-plane anisotropy (sketched as a circle around the Fe ions), at 10K (b) a spin flop transition due to the different direction of the Gd anisotropy occours (see text for discussion).*

tion. The crystal field of $RFe_3(BO_3)_4$ splits the ground-state multiplet of an ion R^{3+} with odd number of electrons into Γ_4 and Γ_{56} Kramers doublets within the D_3 site symmetry. The analysis of Raman selection rules for the ground-state spin flip scattering shows that in the case of the Γ_4 ground state all the components of the Raman tensor are allowed while in the case of the Γ_{56} ground state only the antisymmetric xy-yx component is Raman active. Thus, a relatively strong (xz) Raman LFP of $NdFe_3(BO_3)_4$ points to the Γ_4 symmetry of the Nd^{3+} ground state.

The second major feature of the iron spin ordering is the arising of a broad structured scattering band around 60 cm^{-1} ascribed to two-magnon Raman scattering involving the creation of a pair of magnons with wave vectors $\vec{k}$ and $-\vec{k}$. Below the Néel temperature this is a characteristic feature for all the different compound investigated of the $RFe_3(BO_3)_4$ family (R=Y, Er, Tb, Gd and Nd). Figure 2.11 shows the temperature evolution of this broad signature of magnetic scattering. The spectra reported in Fig.2.11 are found in the (xz+yz) polarization only. No evidence of magnetic scattering is found when the $\vec{k}$ vector of light is parallel to the c-axis (z(xx+yy+xy)z).

As discussed in the previous section, $NdFe_3(BO_3)_4$ does not undergo a structural phase transition and the crystal space group remains the high temperature one ($R32$), while the symmetry of all the other compounds investigated (for R=Gd, Tb, Y, and Er) is reduced to the space group $P3_121$. It is evident from

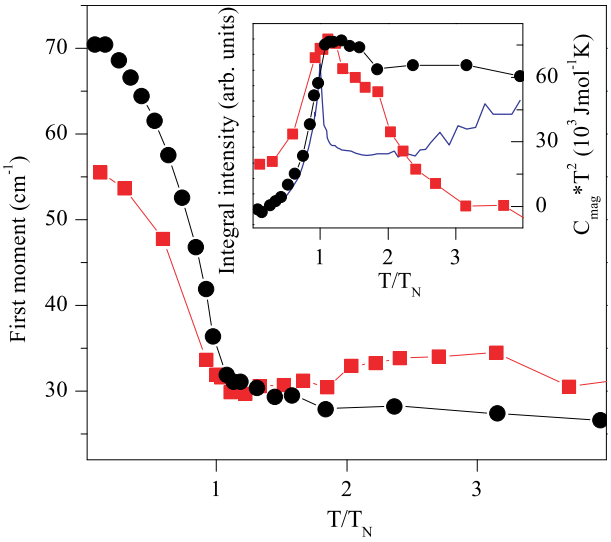

Figure 2.16: *First moment $< \omega >$ of the magnetic excitation vs temperature calculated from 5 to 85 cm^{-1} for $GdFe_3(BO_3)_4$ (circles) and $NdFe_3(BO_3)_4$ (squares). The inset shows the integrated intensity of the magnetic signal at different temperature, compared to the magnetic heat capacity of $YFe_3(BO_3)_4$ (solid line)[9].*

Fig.2.11 that the magnetic scattering spectra of all iron borates are quite similar. So, the presence of inequivalent Fe chains [8] in the low-temperature structure of $RFe_3(BO_3)_4$, R = Gd, Tb, Y, and Er does not strongly affect the magnetic excitation spectra, and the spectra can be analyzed taking into account only the four different magnetic ions present in the *R*32 unit cell (three Fe^{3+} ions and one R^{3+} ion). Still, a rather complicated two-magnon spectrum is expected, strongly depending on the anisotropy parameters. At the lowest temperature reached (T=2.7 K) the two-magnon spectra indeed show a complex structure exhibiting at least three main peaks (Fig.2.11). As the most efficient mechanism of two-magnon scattering in antiferromagnets is usually the exchange-scattering mechanism, and the strongest exchange interaction is between the iron atoms along the helicoidal chains, these peaks presumably arise from three magnon branches representing spin excitations on the iron chains.

The broad magnetic scattering feature of Gd, Tb, Er and Y compounds is approximately centered around $\simeq$70 cm^{-1}, while the one of Nd is centered at lower frequency ($\simeq$60 cm^{-1}). This suggests that the bigger ionic radius of Nd^{3+}, causes the interatomic Fe-Fe distances to be larger, and therefore the exchange interaction to be smaller, this would be consistent with the scaling of T_N with the rare earth's ionic radii [9]. Unfortunately, due to the presence of phonon modes at the same frequency of the magnetic excitation, it is not possible to determine the frequency scaling of the magnetic scattering among the other compounds (Gd,

Tb, Er and Y) to confirm it.

At the temperature of the spin-reorientational transition (T_R), no drastic changes are observed in the magnon spectra. This observation confirms that the observed scattering is mainly due to magnetic excitations on the Fe^{3+} chains, and sheds light on the proposed exotic magnetic ordering of Fe spins for the $GdFe_3(BO_3)_4$ compound. The configuration with 120° angle between nearest neighbor Fe^{3+} spins for $T_N > T > T_R$ which then reorient at T_R into an easy axis antiferromagnet along the c-axis as proposed in [11] is not consistent with our observation. Such a drastic change in the spin configuration would induce a major change in the two-magnon dispersion and inelastic scattering spectra. The picture of a reorientational phase transition at T_R, as proposed in [13, 12], survives assuming an easy-axis/easy-plane anisotropy perpendicular to the c-axis in the temperature region $T_R < T < T_N$. Indeed, considering a simple Heisenberg-type Hamiltonian, where the interaction depends only on the nearest neighbor scalar product, an easy axis anisotropy perpendicular or parallel to the c-axis would produce similar magnetic excitation spectra and therefore similar two-magnon spectra.

A striking feature of the magnetic scattering, as shown in Fig. 2.11(d,e), is the persistence of the magnetic scattering in an anomalous shape up to extremely high temperature above T_N. In the three-dimensional antiferromagnet NiF_2 this "paramagnon scattering" has been observed well into the paramagnetic phase up to $4T_N$ [23]. The first moment of the frequency $< \omega >$ as a function of temperature in NiF_2 and MnF_2 exhibited a fast decrease to lower frequency ($\simeq 10\%$ of the "0 temperature value") at T_N and a subsequent smooth decrease to zero for $T > T_N$, in excellent qualitative agreement with the theory prediction for the moments [24]. Also in the case of $RFe_3(BO_3)_4$ the two-magnon spectrum softens continuously its frequency approaching the Néel temperature (Fig.2.11). Yet, surprisingly, the paramagnon scattering survives at all measured temperatures above T_N (*i.e.* up to about 10 times T_N). As reported in Fig. 2.16, the first moment of the excitation decreases at T_N less than expected and approaches zero only very slowly above T_N. Considering $NdFe_3(BO_3)_4$, the minimum at T_N and subsequent increases with temperature up to 2.5 T_N of the first moment is possibly due to the presence of luminescence lines overlapping with features of the magnetic scattering. This is likely also the origin of the temperature shift to high frequency (lower absolute energy) of the excitation observed at around $80cm^{-1}$.

From a theoretical point of view the presence of quasi-elastic scattering well into the paramagnetic phase of three-dimensional antiferromagnets has been ascribed to two possible origins, namely, spin diffusion [25] and spin density fluctuations or energy diffusion [26]. In the scenario of spin diffusion, absent in a perfect one-dimensional system, the four-spin correlation function (describing the Raman response) is well approximated by a Gaussian shape centered at zero energy. In contrast, for the energy diffusion scenario one expects a lorentzian lineshape in the absence of strong spin-lattice interactions. The integrated intensity I_m in the energy diffusion scenario is expected to follow the magnetic contribution to the

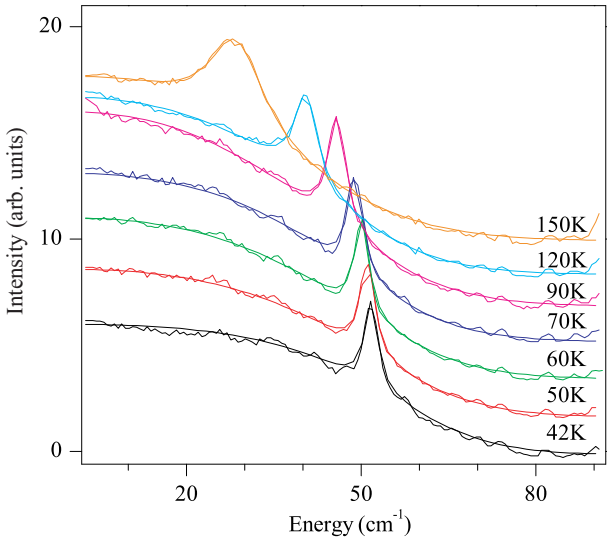

Figure 2.17: *Low frequency Raman scattering above the Néel temperature for $GdFe_3(BO_3)_4$. The different temperature are depicted with an offset for clarity. The paramagnon scattering is present up to almost $4T_N$. The fit is obtained with an fenomenological curve $f(\omega) = \frac{G}{1+aG} + L$, where G is a Gaussian distribution centered at 0 frequency, and L is a Lorenzian distribution to take into account the presence of the vibrational mode (see text for discussion).*

heat capacity C_m as $I_m \propto C_m T^2$[25, 26]. In the presence of strong spin-lattice coupling this later relation is expected to remain valid, even though the low energy scattering is expected to broaden significantly due to the rapid relaxation of the magnetic excitation energy into the lattice.

The shape of the low-energy scattering feature in the paramagnetic phase is different from any previously reported. Neither a Lorenzian nor a Gaussian distribution can fit our data. This anomalous shape of the paramagnon scattering continuum is a common feature of all the compounds investigated; Fig.2.17 depicts the observed spectra of $GdFe_3(BO_3)_4$ as an example. The observation that the spectra can not be modelled with either a Gaussian nor a Lorentzian response might evidence the presence of important spin-lattice interactions, in line with the observations discussed in the previous section. A comparison of the integrated intensity for $GdFe_3(BO_3)_4$ and $NdFe_3(BO_3)_4$ to the magnetic heat capacity determined by Hinatsu *et al.*[9] (see inset fig. 12) for $YFe_3(BO_3)_4$ does not show a fair agreement in the 'paramagnetic' phase, even though there is a good correlation below the phase transition. Apparently energy diffusion, combined with spin-lattice coupling does not explain the observed scattering. On the other hand, as shown in Figure 2.17 the spectra for $GdFe_3(BO_3)_4$ can be fitted nicely at all temperature with a broad phenomenological function consisting of a renormalized

Gaussian distribution $I(\omega) = \frac{G(\omega)}{1+\alpha G(\omega)} + L$, where $G(\omega)$ is a pure Gaussian, and $L(\omega)$ is a lorentzian to account for the phonon line observed in the spectra. This equation is reminescent of the response function of interacting magnons in low dimensional quantum spin systems, although it would be unclear why this would still hold for a $S = 5/2$ system at high temperatures. At present one can not draw a definite conclusion, but the results do strongly suggest that short range order correlations in the spin system survives up to quite high temperatures. Most likely an interplay between the low dimensionality and strong spin-lattice interactions are responsible for the observed unique behavior of the magnetic scattering up to several times T_N, and deserves further studies.

2.4 Summary

In summary, structural, magnetic, and magneto-elastic properties of various members of the $RFe_3(BO_3)_4$ family (R = Gd, Tb, Nd, Er, and Y) have been studied. Making use of x-ray diffraction at 90K it is found that the LT-structure of $GFe_3(BO_3)_4$ has the $P3_121$ symmetry. The scattering spectra observed in the low-temperature phase for $GdFe_3(BO_3)_4$ are fully consistent with the group theoretical analysis calculated using this space group. A detailed analysis of the vibrational Raman spectra of the other compounds (R=Tb, Er and Y) showed that the low temperature phase of those is likely to have the same symmetry as the Gd one's. The $NdFe_3(BO_3)_4$ does not undergo any structural phase transition. The phase transition to the low temperature structure is characterized by the sudden appearance of a strong mode ascribed to the activation of a librational mode of the BO_3 groups. The "1^{st}-order-like" appearance of this vibrational mode and its subsequent "2^{nd}-order-like" temperature evolution led to the discussion in terms of as a weak first-order structural phase transition. At the temperature of the magnetic ordering transition a strong magneto-elastic coupling is revealed for all the compounds. The analysis of the two-magnon Raman scattering in the magnetic phases showed qualitatively similar scattering spectra for the five compounds investigated, evidencing that the structural differences between them do not strongly affect the magnetism and the magnetic excitation spectra. Finally an unprecedented and intriguing paramagnon scattering continuum up to quite high temperatures ($10T_N$) is observed. The origin of this scattering does not seem to be the usual energy diffusion observed in a variety of other magnetic system, and seems to indicate the presence of short-range order spin-spin correlations arising from the low-dimensional nature of these compounds.

2.4.1 Appendix: Allowed Terms in Landau Expansion

To discuss the anomalous "weak first order" character of the phase transition in $RFe_3(BO_3)_4$, it was stated that even terms of the Landau expansion of the free energy in the order parameter are allowed by the crystal symmetry of the family. In this section we give a group theory fundament to that statement proving that the cubic term is indeed allowed by the crystal symmetry. The crystal symmetry of all $RFe_3(BO_3)_4$ in the two phases (only high T for $NdFe_3(BO_3)_4$) have a D_3 point group symmetry. Having the phase transition a structural character the straight forward order parameter considered is the relative atomic displacement of the two phases. In this sense the third order term of the free energy is proportional to $F \propto \delta^3$, and being a number should be invariant under the group symmetry operations. In the group theory language this is nothing more than checking that the representation of a displacement to the third power contain the fully symmetric representation.

$$\Gamma_V \otimes \Gamma_V \otimes \Gamma_V = (A_2 + E) \times (A_2 + E) \times (A_2 + E) = 7A_1 + 8A_2 + 11E \quad (2.7)$$

Where we introduce the representation of a vector $\Gamma_V = A_2 + E$. This is enough to proof that cubic term of the Landau expansion are allowed. The proof for the higher order terms is a trivial extension of this.

Table 2.4: *Crystallographic parameters*

a-Crystal data and details of the structure determination.

	Room Temperature = 293(1) K	T = 90(1) K
Moiety Formula	$GdFe_3(BO_3)_4$	
Formula Weight ($g.mol^{-1}$)	560.04	
Crystal System	Trigonal	
Space group.	$R32$, 155	$P3_121$, 152
a (Å)	9.5203(6)	9.5305(3)
c (Å)	7.5439(5)	7.5479(2)
V (Å^3)	592.15(7)	593.73(3)
Θ range unit cell:min.-max., deg; reflections	3.66-38.70;4767	3.66-38.55; 5439
Formula_Z	3	3
Space group_Z	18	6
Z'(=Formula_Z/SpaceGroup_Z)	1/6	0.5
$\rho(g/cm^3)$	4.712	4.699
F(000) electrons	774	774
$\mu(MoK\alpha)(cm^{-1})$	137.74	137.37

b-Data collection.

$\lambda(MoK\bar{\alpha})$, Å	0.71073	
Monochromator	Graphite	
Measurements device type	Bruker SMART APEX, CCD area-detector diffractometer	
Detector area resolution (pixels/mm)	4096 × 4096/62 × 62 (binned 512)	
Measurement method	φ- and ω-scans	φ- and ω-scans
θ range; min. max.,deg	3.66, 38.70	2.47, 38.58
Index ranges	$h:-16\rightarrow 16; k:-16\rightarrow 16;$ $l:-13\rightarrow 13$	$h:-16\rightarrow 16; k:-16\rightarrow$ $l:-13\rightarrow 13$
Min.- Max. absorption transmission factor	0.0563-0.2519	0.0620-0.2513
X-ray exposure time, h	16.0	16.0
Total data	4700	13868
Unique data	755	2217
Data with criterion: ($F_o \geq 4.0\sigma(F_o)$)	755	1956
$R_{int} = \sum[\lvert F_o^2 - F_o^2(mean)\rvert]/\sum[F_o^2]$	0.0339	0.0338
$R_{sig} = \sum\sigma(F_o^2)/[F_o^2]$	0.0203	0.0189

c-Refinement.

Number of reflections	755	2217
Number of refined parameters	35	95
Isotropic secondary-extinction coefficient, g	0.0371(12)	0.0359(10)
Final agreement factors: $wR(F^2) = [\sum[w(F_o^2 - F_c^2)^2]/[w(F_o^2)^2]]^{1/2}$	0.0374	0.0452
Weighting scheme: a, b $w = 1/[\sigma^2(F_o^2) + (aP)^2 + bP]$ And $P = [max(F_o^2, 0) + 2F_c^2]/3$	0.0272, 0.0	0.0312, 0.0
$R(F) = \sum(\lvert\lvert F_o\rvert - \lvert F_c\rvert\rvert)/\sum\lvert F_o\rvert For F_o > 4.0\sigma(F_o)$	0.0151	0.0167
Absolute-Structure parameter Flack's x	0.50	0.50
$GooF = S = [\sum[w(F_o^2 - F_c^2)^2]/(n-p)]^{1/2}$ n = number of reflections p = number of parameters refined	1.075	0.855
Residual electron density in final Difference Fourier map, e/Å^3	-1.0, 0.6(1)	-0.5,0.8(1)
Max. (shift/s) final cycle	0.001	0.003
Average (shift/σ) final cycle	0.000	0.000

Table 2.5: *Fractional atomic coordinates and Anisotropic Parameters at RT*

Atom	Wyckoff	Schoenflies	x	y	z	U_{eq}(Å)
Gd	3 a	D_3	0	0	0	0.00867(5)
Fe	9 d	C_2	0.21659(5)	1/3	1/3	0.00654(9)
O1	9 e	C_2	0.1442(2)	x	1/2	0.0083(3)
O2	9 e	C_2	0.4087(3)	x	1/2	0.0132(5)
O3	18 f	C_1	0.0254(2)	0.2125(2)	0.1824(2)	0.0095(3)
B1	3 b	D_3	0	0	1/2	0.0066(6)
B2	9 e	C_2	0.5526(3)	x	1/2	0.0077(4)

Atom	U_{11}	U_{22}	U_{33}	U_{23}	U_{13}	U_{12}
Gd	0.00888(8)	0.00888(8)	0.00825(9)	0.0000(-)	0.0000(-)	0.00444(4)
Fe	0.00591(12)	0.00635(14)	0.00750(18)	0.00009(8)	0.00004(4)	0.00317(7)
O1	0.0058(5)	0.0058(5)	0.0109(7)	0.0014(3)	0.0014(3)	0.0011(6)
O2	0.0076(6)	0.0076(6)	0.0182(11)	0.0047(5)	0.0047(5)	0.0009(8)
O3	0.0065(5)	0.0112(5)	0.0111(5)	0.0025(5)	0.0021(4)	0.0046(4)
B1	0.0058(9)	0.0058(9)	0.0081(14)	0.0000(0)	0.0000(-)	0.0029(4)
B2	0.0070(7)	0.0070(7)	0.0093(8)	0.0007(4)	0.0007(4)	0.0036(11)

Table 2.6: *Fractional atomic coordinates and Anisotropic Parameters at T=90 K*

Atom	Wyckoff	Schoenflies	x	y	z	U_{eq}(Å)
Gd	3 a	C_2	-0.33342(1)	x	0	0.00406(4)
Fe1	3 a	C_2	0.11536(5)	x	0	0.00360(6)
Fe2	6 c	C_1	-0.21420(6)	-0.54975(4)	0.34154(2)	0.00366(6)
O1	3 b	C_2	0	-0.07819(15)	1/6	0.0072(3)
O2	6 c	C_1	-0.5832(2)	-0.2709(1)	0.13774(12)	0.00692(17)
O3	6 c	C_1	-0.1194(3)	-0.30445(26)	-0.17980(18)	0.0057(3)
O4	6 c	C_1	-0.1467(3)	-0.36234(16)	0.18479(18)	0.0058(2)
O5	6 c	C_1	0.4755(2)	0.1451(2)	-0.15980(8)	0.0057(3)
O6	3 b	C_2	0.1877(2)	0	5/6	0.0049(3)
O7	6 c	C_1	-0.5235(3)	-0.53811(17)	-0.18533(18)	0.0056(2)
B2a	6 c	C_1	-0.4473(4)	-0.1201(-)	0.15617(14)	0.0053(3)
B2b	3 b	C_2	0	-0.2223(3)	1/6	0.0049(4)
B1	3 b	C_2	0.33204(14)	0	5/6	0.0045(5)

Atom	U_{11}	U_{22}	U_{33}	U_{23}	U_{13}	U_{12}
Gd	0.00409(6)	0.00409(7)	0.00408(7)	0.00010(2)	0.00009(1)	0.00210(3)
Fe	0.00355(10)	0.00355(10)	0.00355(10)	0.00006(4)	0.00006(4)	0.00166(10)
Fe	0.00349(9)	0.00356(11)	0.00378(9)	0.00013(7)	0.00003(5)	0.00166(6)
O1	0.0081(6)	0.0054(4)	0.0089(4)	0.00121(19)	0.0024(4)	0.0040(3)
O2	0.0058(3)	0.0062(3)	0.081(3	0.0012(3)	0.0014(3)	0.0025(3)
O3	0.0062(4)	0.0040(5)	0.0065(4)	0.0006(3)	0.0007(3)	0.0023(4)
O4	0.0054(4)	0.0045(4)	0.0067(4)	0.0007(3)	0.0003(3)	0.0019(4)
O5	0.0051(4)	0.0050(4)	0.0063(5)	0.0007(3)	0.0003(3)	0.0019(5)
O6	0.0044(4)	0.0058(6)	0.0062(5)	0.0019(5)	0.0010(2)	0.0029(3)
O7	0.0047(4)	0.0063(4)	0.0064(4)	0.0008(3)	0.0001(3)	0.0033(4)
B2a	0.0050(6)	0.0067(7)	0.0055(5)	0.0004(5)	0.0001(4)	0.0040(4)
B2b	0.0018(8)	0.0061(6)	0.0055(7)	0.0004(3)	0.0008(6)	0.0009(4)
B1	0.0042(8)	0.0048(9)	0.0046(11)	0.0009(5)	0.0004(2)	0.0024(4)

Table 2.7: *Observed vibrational modes for the high-temperature phase of several rare-earth iron borates.*

External modes ($3A_1 \oplus 11E$)

$NdFe_3(BO_3)_4$			$GdFe_3(BO_3)_4$			$TbFe_3(BO_3)_4$		$ErFe_3(BO_3)_4$		$YFe_3(BO_3)_4$	
A_1	E_{TO}	E_{LO}	A_1	E_{TO}	E_{LO}	A_1	E	A_1	E	A_1	E
180	89	93	180	84	93	180	93	181	84	180	107
298		159	307	160	160	309	159	312	160	312	158
473		193	475	195	198	476	198	472	199	468	200
		232			232		230		225		
	260	266		270	270		270		272		268
	272	281		273	287		287				
	312	332		315	330		330		325		327
	354	356		352	357		355		350		354
		384		391	391		392		395		390
		439		443	443		444		442		441
	475	488			488		480		475		470

Internal modes ($4A_1 \oplus 8E$)

$NdFe_3(BO_3)_4$		$GdFe_3(BO_3)_4$			$TbFe_3(BO_3)_4$		$ErFe_3(BO_3)_4$		$YFe_3(BO_3)_4$	
A_1	E	A_1	E_{TO}	E_{LO}	A_1	E	A_1	E	A_1	E
636	579	638		580	635	579	632	579	631	576
950	625	957	631	633	957	632	960	632		
990	669	990	670	676	988	676	988	675	984	672
1220	734	1230		735	1220	734	1230	730		732
	968			968		966		960		959
	1195									1219
	1218			1212		1214		1220		1230
	1244			1229		1230		1233		1408
	1260		1198	1250		1254				
	1413		1280	1414		1411		1342		

Modes appearing in the low T phase: $20A_1$ (12 ext. and 8 int.) $\oplus$ $40E$ (24 ext. an 16 int.)

$NdFe_3(BO_3)_4$	$GdFe_3(BO_3)_4$		$TbFe_3(BO_3)_4$		$ErFe_3(BO_3)_4$		$YFe_3(BO_3)_4$	
-	A_1	E	A_1	E	A_1	E	A_1	E
-	53	101	54		72		76	
-	144	114			149		150	111
-	203	167		169	202	170	206	173
-	233	206	232	207	234	208		211
-	244	254	247	256		250	246	253
-	263	276	265	278		278		280
-		281		282		284		287
-		305		306		305		307
-	368	310	368	311				
-	385	337		337				335
-		374		375		373		370
-								378
-		395		398				
-	677	472	679	473		470		
-	724	596	723	597				
-		654	953	654				
-		669		670				
-		955		954				
-		968		966				

Bibliography

[1] D. Jaque, J. of Alloys and Compounds **323-324**, 204 (2001).

[2] A. Brenier, C. Tu, Z. Zhu, and B. Wu, Appl. Phys. Lett. **84**, 2034 (2004).

[3] X. Chen, Z. Luo, D. Jaque, J. J. Romero, J. Garcia Solé, Y. Huang, A. Jiang, and C. Tu, J. Phys. :Cond. Mat. **13**, 1171 (2001).

[4] A. K. Zvezdin, S. S. Krotov, A. M. Kadomtseva, G. P. Vorob'ev, Y. F. Popov, A. P. Pyatakov, L. N. Bezmaternykh, and E. Popova, JETP Lett. **81**, 272 (2005).

[5] J. C. Joubert, W. B. White, and R. Roy, J. Appl. Cryst. **1**, 318 (1968).

[6] E. L. Belokoneva, L. I. Alshinskaya, M. A. Simonov, N. I. Leonyuk, T. I. Timchenko, and N. V. Belov, Journal Sructurnoi Khimii (Russian Journal of Structural Chemistry) **20**, 542 (1979).

[7] J. A. Campa, C. Cascales, E. Gutierrez-Puebla, M. A. Monge, I. Rasines, and C. Ruiz-Valero, Chem. Mater. **9**, 237 (1997).

[8] S. A. Klimin, D. Fausti, A. Meetsma, L. N. Bezmaternykh, P. H. M. van Loosdrecht, and T. T. M. Palstra, Acta Cryst. B **61**, 481 (2005), URL`http://xxx.lanl.gov/abs/cond-mat/0502423`.

[9] Y. Hinatsu, Y. Doi, K. Ito, K. Wakeshima, and A. Alemi, J. Solid State Chem. **172**, 438 (2003).

[10] E. P. Chukalina, D. Y. Kuritsin, M. N. Popova, L. N. Bezmaternykh, S. A. Kharlamova, and V. L. Temerov, Phys. Lett. A **322**, 239 (2004).

[11] D. Balaev, L. N. Bezmaternyh, I. A. Gudim, V. L. Temerov, S. G. Ovchinnikov, and S. A. Kharlamova, JMMM **258-259**, 532 (2003).

[12] R. Z. Levitin, E. A. Popova, R. M. Chtsherbov, A. N. Vasiliev, M. N. Popova, E. P. Chukalina, S. A. Klimin, P. H. M. van Loosdrecht, D. Fausti, and L. N. Bezmaternykh, JETP Lett. **79**, 423 (2004).

[13] A. I. Pancratz, G. A. Petrakovskii, L. N. Bezmaternykh, and O. A. Bayukov, JETP **99**, 766 (2004).

[14] A. G. Gavriliuk, S. A. Kharlamova, I. S. Lyubutin, I. A. Troyan, E. S. Ovchinnikov, A. M. Potsjelujko, M. I. Eremets, and R. Böhler, JETP Lett. **80**, 426 (2004).

[15] A. de Andres, F. Agullo-Rueda, S. Taboada, C. Cascales, J. Campa, C. Ruiz-Valero, and I. Rasines, J. Alloys and Compounds **250**, 396 (1997).

[16] L. N. Bezmaternykh, V. L. Temerov, I. A. Gudim, , and N. A. Stolbovaya, Crystallography Reports **50, Suppl. 1**, S97 (2005).

[17] L. N. Bezmaternykh, S. A. Kharlamova, and V. L. Temerov, Crystallography Reports **49**, 855 (2004).

[18] D. L. Rousseau, R. P. Bauman, and S. P. S. Porto, J. of Raman Spectroscopy **10**, 253 (1981).

[19] B. N. Mavrin, Optika i Spektroskopiya **49**, 79 (1980).

[20] G. Herzberg, *Infrared and Raman spectra of polyatomic molecules* (Van Nostrand Reinhold, New York, 1945).

[21] L. D. Landau and E. M. Lifshitz, *Statistical Physics* (Pergamon Press, Oxford, 1980).

[22] A. D. Bruce and R. A. Cowley, *Structural Phase Transitions* (Taylor & Francis, London, 1981).

[23] P. A. Fleury, Phys. Rev. **180**, 591 (1969).

[24] M. G. Cottam and D. J. Lockwood, *Light Scattering in Magnetic Solids* (JohnWilley & Sons, New York, 1986).

[25] P. M. Richards and W. J. Brya, Phys. Rev. B **9**, 3044 (1974).

[26] J. W. Halley, Phys. Rev. Lett. **41**, 1605 (1978).

[27] Bruker (2000). SMART, SAINT, SADABS, XPREP and SHELXTL/NT. Area Detector Control and Integration Software. Smart Apex Software Reference Manuals. Bruker Analytical X-ray Instruments. Inc., Madison, Wisconsin, USA.

[28] A. J. M. Duisenberg, J. Appl. Cryst. **25**, 92 (1992).

[29] A.L. Spek, J. Appl. Cryst. **21**, 578 (1988).

[30] Y. Le Page, J. Appl. Cryst. **20**, 264 (1987).

[31] Y. Le Page, J. Appl. Cryst. **21**, 983 (1988).

[32] H. D. Flack, Acta Cryst. A **39**, 876 (1983).

[33] H. D. Flack, Acta Cryst. A **55**, 908 (1999).

[34] H. D. Flack, Acta Cryst. A **33**, 1143 (2000).

[35] J. B. Goodenough, Phys. Rev. **100**, 564 (1955).

Chapter 3

Symmetry Disquisition on the TiOX Phase Diagram

3.1 Introduction

The properties of low-dimensional spin systems are one of the key topics of contemporary condensed matter physics. Above all, the transition metal oxides with highly anisotropic interactions and low-dimensional structural elements provide a fascinating playground to study novel phenomena, arising from their low-dimensional nature and from the interplay between lattice, orbital, spin and charge degrees of freedom. In particular, low-dimensional quantum spin (S=1/2) systems have been widely discussed in recent years. Among them, layered systems based on a $3d^9$ electronic configuration were extensively studied in view of the possible relevance of quantum magnetism to high temperature superconductivity[1, 3]. Though they received less attention, also spin=1/2 systems based on early transition metal oxides with electronic configuration $3d^1$, such as titanium oxyhalides (TiOX, with X=Br or Cl), exhibit a variety of interesting properties[4, 5]. The attention originally devoted to the layered quasi two-dimensional $3d^1$ antiferromagnets arose from considering them as the electron analog to the high-T_c cuprates[6]. Only recently TiOX emerged in a totally new light, namely as a one-dimensional antiferromagnet and as the second example of an inorganic spin-Peierls compound (the first being $CuGeO_3$)[7, 8, 2].

The TiO bilayers constituting the TiOX lattice are candidates for various exotic electronic configurations, such as orbital ordered[4], spin-Peierls[7] and resonating-valence-bond states[9]. In the case of the TiOX family the degeneracy of the d orbitals is completely removed by the crystal field splitting, so that the only $d-$electron present, mainly localized on the Ti site, occupies a nondegenerate energy orbital (see Fig.3.1(c))[4]. As a consequence of the shape of the occupied orbital (which has lobes oriented in the $b-$ and $c-$directions, where c is

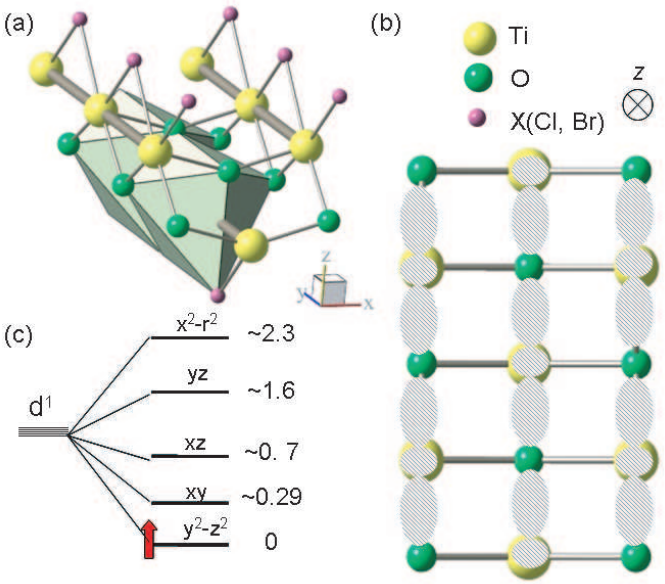

Figure 3.1: *(a) Sketch of the TiOX bilayer. The energy splitting of the Ti d orbital and their symmetry is summarized by the energy scheme in (c). The shape of the ground state d orbital responsible for the one dimensional characteristic of the magnetic properties (see text) is depicted in (b).*

perpendicular to the layers - Fig.3.1 (b)), the exchange interaction between the spins on different Ti ions arises mainly from direct exchange within the TiO bilayers, along the *b* crystallographic direction[4]. This, in spite of the two-dimensional structural character, gives the magnetic system of the TiOX family its peculiar quasi one-dimensional properties[7].

Magnetic susceptibility[7] and ESR [4] measurements at high temperature are in reasonably good agreement with an antiferromagnetic, one-dimensional spin-1/2 Heisenberg chain model. At low temperature (T_{c1}) TiOX shows a first-order phase transition to a dimerised nonmagnetic state, discussed in terms of a spin Peierls state [7, 11, 12]. Between this low temperature spin Peierls phase (SP) and the one-dimensional antiferromagnet in the high temperature phase (HT), various experimental evidence [13, 14, 5, 15] showed the existence of an intermediate phase, whose nature and origin is still debated. The temperature region of the intermediate phase is different for the two compounds considered in this work, for TiOBr $T_{c1} = 28$ K and $T_{c2} = 48$ K while for TiOCl $T_{c1} = 67$ K and $T_{c2} = 91$ K. To summarize the properties so far reported, the intermediate phase ($T_{c1} < T_{c2}$) exhibits a gapped magnetic excitation spectrum[5], anomalous broadening of the phonon modes in Raman and IR spectra[15, 11], and features of a periodicity

incommensurate with the lattice[16, 17, 18]. Moreover, the presence of a pressure induced metal to insulator transition has been recently suggested for TiOCl[28]. Due to this complex phase behavior, both TiOCl and TiOBr have been extensively discussed in recent literature, and various questions still remain open: there is no agreement on the crystal symmetry of the spin Peierls phase, the nature and symmetry of the incommensurate phase is not clear and the anomalous first-order character of the transition to the spin Peierls state is not explained.

Optical methods like Raman spectroscopy are powerful experimental tools for revealing the characteristic energy scales associated with the development of broken symmetry ground states, driven by magnetic and structural phase transitions. Indeed, information on the nature of the magnetic ground state, lattice distortion, and interplay of magnetic and lattice degrees of freedom can be obtained by studying in detail the magnetic excitations and the phonon spectrum as a function of temperature. The present chapter reports on a vibrational Raman study of TiOCl and TiOBr, a study of the symmetry properties of the three phases and gives coherent view of the anomalous first order character of the transition to the spin Peierls phase. Through pressure-dependence measurements of the magnetic susceptibility, the role of magnon-phonon coupling in determining the complex phase diagram of TiOX is discussed. Finally, via a comparison with the isostructural compound VOCl, the previously reported[15, 19] high energy scattering is revisited, ruling out a possible interpretation in terms of magnon excitations.

3.2 Experiment

Single crystals of TiOCl, TiOBr, and VOCl have been grown by a chemical vapor transport technique. The crystallinity was checked by X-ray diffraction[14]. Typical crystal dimensions are a few mm^2 in the $ab-$plane and 10-100 μm along the $c-$axis, the stacking direction[17]. The sample was mounted in an optical flow cryostat, with a temperature stabilization better than 0.1 K in the range from 2.6 K to 300 K. The Raman measurements were performed using a triple grating micro-Raman spectrometer (Jobin Yvon, T64000), equipped with a liquid nitrogen cooled CCD detector (resolution 2 cm^{-1} for the considered frequency interval). The experiments were performed with a 532 nm Nd:YVO_4 laser. The power density on the sample was kept below 500 W/cm^2 to avoid sample degradation and to minimize heating effects.

The polarization was controlled on both the incoming and outgoing beam, giving access to all the polarizations schemes allowed by the back-scattering configuration. Due to the macroscopic morphology of the samples (thin sheets with natural surfaces parallel to the $ab-$planes) the polarization analysis was performed mainly with the incoming beam parallel to the $c-$axis (c(aa)$\bar{c}$, c(ab)$\bar{c}$ and c(bb)$\bar{c}$, in Porto notation). Some measurements were performed with the incoming light polarized along the $c-$axis, where the $k-$vector of the light was parallel to the $ab-$plane and the polarization of the outgoing light was not controlled. These

measurements will be labeled as $x(c\star)\bar{x}$.

The magnetization measurements were performed in a Quantum Design Magnetic Property Measurement System. The pressure cell used is specifically designed for measurement of the DC-magnetization in order to minimize the cell's magnetic response. The cell was calibrated using the lead superconducting transition as a reference, and the cell's signal (measured at atmospheric pressure) was subtracted from the data.

3.3 Results and Discussion

The discussion will start with a comparison of Raman experiments on TiOCl and TiOBr in the high temperature phase, showing the consistency with the reported structure. Afterwards, through the analysis of Raman spectra the crystal symmetry in the low temperature phases will be discussed, and in the final part a comparison with the isostructural VOCl will be helpful to shed some light on the origin of the anomalous high energy scattering reported for TiOCl and TiOBr[15, 19].

3.3.1 High Temperature Phase

The crystal structure of TiOX in the high temperature (HT) phase consists of buckled Ti-O bilayers separated by layers of X ions. The HT structure is orthorhombic with space group Pmmn. The full representation[10] of the vibrational modes in this space group is:

$$\Gamma_{tot} = 3A_g + 2B_{1u} + 3B_{2g} + 2B_{2u} + 3B_{3g} + 2B_{3u}. \tag{3.1}$$

Among these, the modes with symmetry B_{1u}, B_{2u}, and B_{3u} are infrared active in the polarizations along the c, b, and a crystallographic axes[11], respectively. The modes with symmetry A_g, B_{2g}, and B_{3g} are expected to be Raman active: The A_g modes in the polarization (aa), (bb), and (cc); the B_{2g} modes in (ac) and the B_{3g} ones in (bc).

Fig.3.2 shows the room temperature Raman measurements in different polarizations for TiOCl and TiOBr, and Fig.3.3 displays the characteristic Raman spectra for the three different phases of TiOBr, the spectra are taken at 100 (a), 30 (b) and 3K (c). At room temperature three Raman active modes are clearly observed in both compounds for the $c(aa)\bar{c}$ and $c(bb)\bar{c}$ polarizations (Fig.3.2), while none are observed in the $c(ab)\bar{c}$ polarization. These results are in good agreement with the group theoretical analysis. The additional weakly active modes observed at 219 cm^{-1} for TiOCl and at 217 cm^{-1} for TiOBr are ascribed to a leak from a different polarization. This is confirmed by the measurements with the optical axis parallel to the ab-planes ($x(c\star)\bar{x}$) on TiOBr, where an intense mode is observed at the same frequency (as shown in the inset of Fig.3.3(a)). In

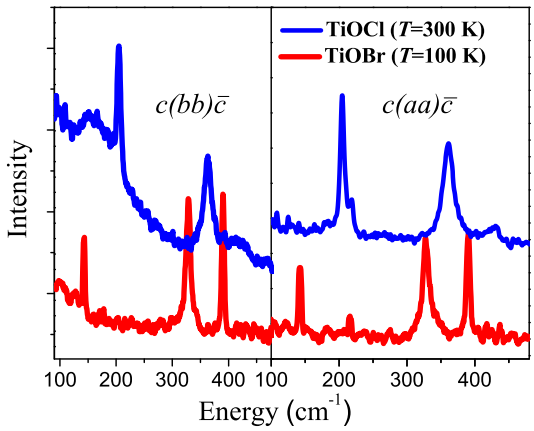

Figure 3.2: *Raman spectra of TiOCl and TOBr in the high temperature phase.*

addition to these expected modes, TiOCl displays a broad peak in the $c(bb)\bar{c}$ polarization, centered at around 160 cm^{-1} at 300K; a similar feature is observed in TiOBr as a broad background in the low frequency region at 100K. As discussed for TiOCl[15], these modes are thought to be due to pre-transitional fluctuations. Upon decreasing the temperature, this "peaked" background first softens, resulting in a broad mode at T_{c2} (see Fig.3.3(b)), and then locks at T_{c1} into an intense sharp mode at 94.5 cm^{-1} for TiOBr (Fig.3.3(c)) and at 131.5 cm^{-1} for TiOCl.

The frequency of all the vibrational modes observed for TiOCl and TiOBr in their high temperature phase are summarized in Table 3.1. Here, the infrared active modes are taken from the literature[11, 8] and for the Raman modes the temperatures chosen for the two compounds are 300K for TiOCl and 100K for TiOBr. The observed Raman frequencies agree well with previous reports[15]. The calculated values reported in Table 3.1 are obtained with a spring-model calculation based on phenomenological longitudinal and transversal spring constants (see Appendix). The spring constants used were optimized using the TiOBr experimental frequencies (except for the ones of the B_{3g} modes due to their uncertain symmetry) and kept constant for the other compounds. The frequencies for the other two compounds are obtained by merely changing the appropriate atomic masses and are in good agreement with the experimental values. The relative atomic displacements for each mode of A_g symmetry are shown in Table 5.1. The scaling ratio for the lowest frequency mode (mode 1) between the two compounds is in good agreement with the calculation of the atomic displacements. The low frequency mode is mostly related to Br/Cl movement and, indeed, the ratio $\nu_{TiOCl}/\nu_{TiOBr} = 1.42$ is similar to the mass ratio $\sqrt{M_{Br}}/\sqrt{M_{Cl}}$. The other modes (2 and 3) involve mainly Ti or O displacements, and their frequencies scale with a lower ratio, as can be expected.

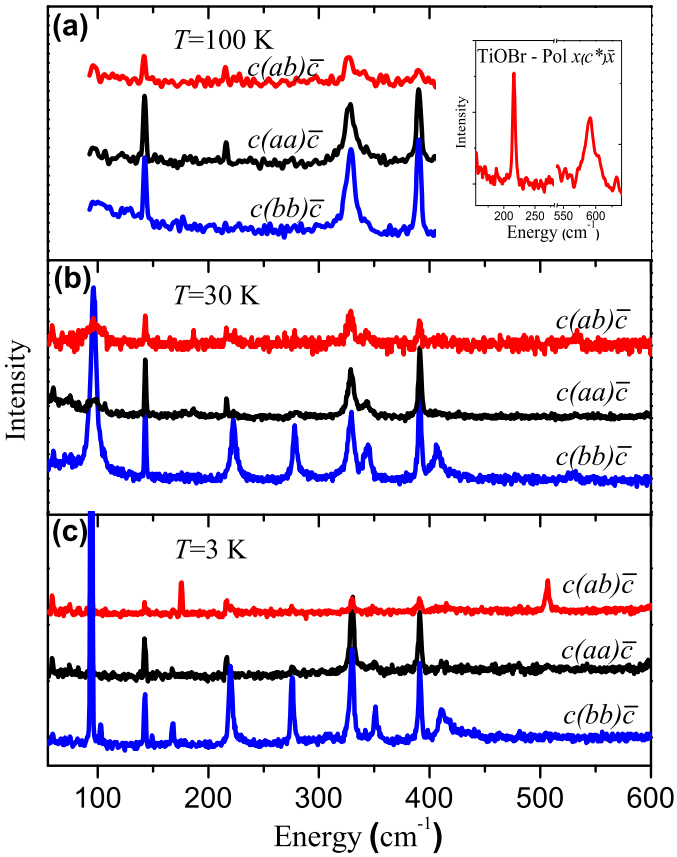

Figure 3.3: *(Color online) Polarization analysis of the Raman spectra in the three phases of TiOBr, taken at 3 (a), 30 (b) and 100K (c). The spectra of TiOCl show the same main features and closely resemble those of TiOBr. Table 3.4 reports the frequencies of the TiOCl modes. The inset shows the TiOBr spectrum in the $x(c*)\bar{x}$ polarization (see text).*

3.3.2 Low Temperature Phases

Although the symmetry of the low temperature phases has been studied by X-ray crystallography, there is no agreement concerning the symmetry of the SP phase; different works proposed two different space groups, $P2_1/m$[18, 16, 17] and $Pmm2$[20].

The possible symmetry changes that a dimerisation of Ti ions in the $b-$direction can cause are considered in order to track down the space group of the TiOX crystals in the low temperature phases. Assuming that the low temperature phases belong to a subgroup of the high temperature orthorhombic space group $Pmmn$,

Table 3.1: *(a)Vibrational modes for the high temperature phase in TiOCl, TiOBr and VOCl. The calculated values are obtained with a spring model. The mode reported in italics in Table 3.1 are measured in the $x(c\star)\bar{x}$ polarization they could therefore have either B_{2g} or B_{3g} symmetry (see experimental details).*

(a)	TiOBr		TiOCl		VOCl	
	Exp.	Cal.	Exp.	Cal.	Exp.	Cal.
A_g $(\sigma_{aa}, \sigma_{bb}, \sigma_{cc})$	142.7	141	203	209.1	201	208.8
	329.8	328.2	364.8	331.2	384.9	321.5
	389.9	403.8	430.9	405.2	408.9	405.2
$B_{2g}(\sigma_{ac})$		105.5		157.1		156.7
		328.5		330.5		320.5
		478.2		478.2		478.2
$B_{3u}(IR, a)$	77[1]	75.7	104[2]	94.4		93.7
	417[1]	428.5	438[2]	428.5		425.2
$B_{3g}(\sigma_{bc})$	*60*	86.4		129.4		129.4
	216	336.8	*219*[3]	336.8		327.2
	598	586.3		586.3		585.6
$B_{2u}(IR, b)$	131[1]	129.1	176[2]	160.8		159.5
	275[1]	271.8	294[2]	272.1		269.8
$B_{1u}(IR, c)$		155.7		194.1		192.4
		304.8		301.1		303.5

there are different candidate space groups for the low temperature phases. Note that the assumption is certainly correct for the intermediate phase, because the transition at T_{c2} is of second-order implying a symmetry reduction, while it is not necessarily correct for the low temperature phase, being the transition at T_{c1} is of first-order.

Fig.3.4 shows a sketch of the three possible low temperature symmetries considered, and Table 3.3 reports a summary of the characteristic of the unit cell together with the number of phonons expected to be active for the different space groups. Depending on the relative position of the neighboring dimerised Ti pairs, the symmetry elements lost in the dimerisation are different and the possible space groups in the SP phase are P2/c (Table 3.3(a)), P2$_1$/m (b) or Pmm2 (c). The first two are monoclinic groups with their unique axis perpendicular to the TiO plane (along the $c-$axis of the orthorhombic phase), and lying in the TiO plane ($\|$ to the $a-$axis of the orthorhombic phase), respectively. The third candidate (Fig.3.4(c)) has orthorhombic symmetry.

The group theory analysis based on the two space groups suggested for the SP phase (P2$_1$/m[16] and Pmm2[20]) shows that the number of modes expected to be Raman active is different in the two cases (Table 3.3(b) and (c)). In particular, the 12 fully symmetric vibrational modes (A_g), in the P2$_1$/m space group, are

Table 3.2: *The ratio between the frequency of the A_g Raman active modes measured in TiOBr and TiOCl is related to the atomic displacements of the different modes as calculated for TiOBr (all the eigenvectors are fully c−polarized, the values are normalized to the largest displacement).*

(b)	Mode	ν(TiOBr)	ν_{Cl}/ν_{Br}	Ti	O	Br
	1	142.7	1.42	0.107	0.068	1
	2	329.8	1.11	1	0.003	0.107
	3	389.9	1.11	0.04	1	0.071

expected to be active in the $\sigma_{xx}, \sigma_{yy}, \sigma_{zz}$ and σ_{xy} polarizations, and $6B_g$ modes are expected to be active in the cross polarizations (σ_{xz} and σ_{yz}). Note that in this notation, z refers to the unique axis of the monoclinic cell, so σ_{yz} corresponds to $c(ab)c$ for the HT orthorhombic phase. For Pmm2 the 11 A_1 vibrational modes are expected to be active in the $\sigma_{xx}, \sigma_{yy}, \sigma_{zz}$ polarizations, and only one mode of symmetry A_2 is expected to be active in the cross polarization (σ_{xy} or $c(ab)c$). The experiments, reported in Table 3.4 for both compounds and in Fig.3.3 for TiOBr only, show that 10 modes are active in the $c(aa)c$ and $c(bb)c$ in the SP phase (Fig.3.3(c)), and, more importantly, two modes are active in the cross polarization $c(ab)c$. This is not compatible with the expectation for Pmm2. Hence the comparison between the experiments and the group theoretical analysis clearly shows that of the two low temperature structures reported in X-ray crystallography[17, 20], only the P$2_1/m$ is compatible with the present results.

As discussed in the introduction, the presence of three phases in different temperature intervals for TiOX is now well established even though the nature of the intermediate phase is still largely debated[14, 8, 17]. The temperature dependence of the Raman active modes for TiOBr between 3 and 50 K, is depicted in Fig.3.5. In the spin-Peierls phase, as discussed above, the reduction of the crystal symmetry[18] increases the number of Raman active modes. Increasing the temperature above T_{c1} a different behavior for the various low temperature phonons is observed. As shown in Fig.3.5, some of the modes disappear suddenly at T_{c1} (labeled L_T), some stay invariant up to the HT phase (R_T) and some others undergo a sudden broadening at T_{c1} and slowly disappear upon approaching T_{c2} (I_T). The polarization analysis of the Raman modes in the temperature region $T_{c1} < T < T_{c2}$ shows that the number of active modes in the intermediate phase is different from that in both the HT and the SP phases. The fact that at $T = T_{c1}$ some of the modes disappear suddenly while some others do not disappear, strongly suggests that the crystal symmetry in the intermediate phase is different from both other phases, and indeed confirms the first-order nature of the transition at T_{c1}.

In the X-ray structure determination [17], the intermediate incommensurate phase is discussed in two ways. Firstly, starting from the HT orthorhombic (Pmmn) and the SP monoclinic space group (P$2_1/m$ - unique axis in the TiO

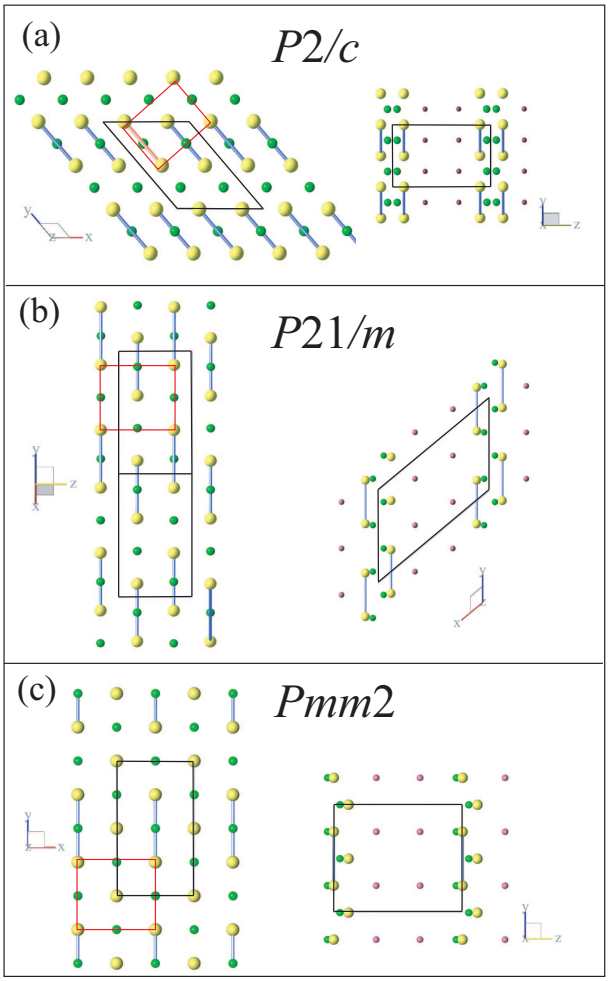

Figure 3.4: *(Color online) Comparison of the possible low temperature symmetries. The low temperature structures reported are discussed, considering a dimerisation of the unit cell due to Ti-Ti coupling and assuming a reduction of the crystal symmetry. The red rectangle denotes the unit cell of the orthorhombic HT structure. Structure (a) is monoclinic with its unique axis parallel to the orthorhombic c−axis (space group P2/c), (b) shows the suggested monoclinic structure for the SP phase ($P2_1/m$), and (c) depicts the alternative orthorhombic symmetry proposed for the low T phase Pmm2.*

planes, ∥ to a), the modulation vector required to explain the observed incommensurate peaks is two-dimensional for both space groups. Secondly, starting from another monoclinic space group, with unique axis perpendicular to the TiO bilayers (P2/c), the modulation vector required is one-dimensional. The latter

Table 3.3: *Comparison between the possible low temperature space group.*

(a)	Space group P$2/c$
	Unique axis $\perp$ to TiO plane, C_{2h}^4
	4TiOBr per unit cell
	$\Gamma = 7A_g + 6A_u + 9B_g + 11B_u$
	$7A_g$ Raman active $\sigma_{xx}, \sigma_{yy}, \sigma_{zz}, \sigma_{xy}$
	$11B_g$ Raman active σ_{xz}, σ_{yz}
	$6A_u$ and $9B_u$ IR active
(b)	Space group P$2_1/m$
	Unique axis in the TiO plane, C_{2h}^2
	4 TiOBr per unit cell
	$\Gamma = 12A_g + 5A_u + 6B_g + 10B_u$
	$12A_g$ Raman active $\sigma_{xx}, \sigma_{yy}, \sigma_{zz}, \sigma_{xy}$
	$6B_g$ Raman active σ_{xz}, σ_{yz}
	$5A_u$ and $10B_u$ IR active
(c)	Space group P$mm2$
	4 TiOBr per unit cell
	$\Gamma = 11A_1 + A_2 + 4B_1 + 5B_2$
	$11A_1$ Raman active $\sigma_{xx}, \sigma_{yy}, \sigma_{zz}$
	A_2 Raman active σ_{xy}
	$4B_1$ and $5B_2$ Raman active in σ_{xz} and σ_{yz}

Table 3.4: *Vibrational modes of the low temperature phases.*

			spin Peierls phase				
(a)	TiOBr	$A_g(\sigma_{xx}, \sigma_{yy})$	94.5	102.7	142.4	167	219
			276.5	330	351	392	411*
		$A_g(\sigma_{xy})$	175,6	506.5			
	TiOCl	$A_g(\sigma_{xx}, \sigma_{yy})$	131.5	145.8	203.5	211.5	296.5
			305.3	322.6	365.1	387.5	431*
		$A_g(\sigma_{xy})$	178.5	524.3			
			Intermediate phase				
(b)	TiOBr (30K)	$A_g(\sigma_{xx}, \sigma_{yy})$	94.5	142	221.5	277	328.5
			344.5	390.4			
	TiOCl (75K)	$A_g(\sigma_{xx}, \sigma_{yy})$	132.8	206.2	302	317.2	364.8
			380	420.6			

* The broad line shape of this feature suggests it may originate from a two-phonon process.

average symmetry is considered (in the commensurate variety) in Fig.3.4(a) and Table 3.3(a).

In the IP, seven modes are observed in the σ_{xx}, σ_{yy} and σ_{zz} geometry on both compounds (see Table 3.4(b)), and none in the σ_{xy} geometry. This appears to

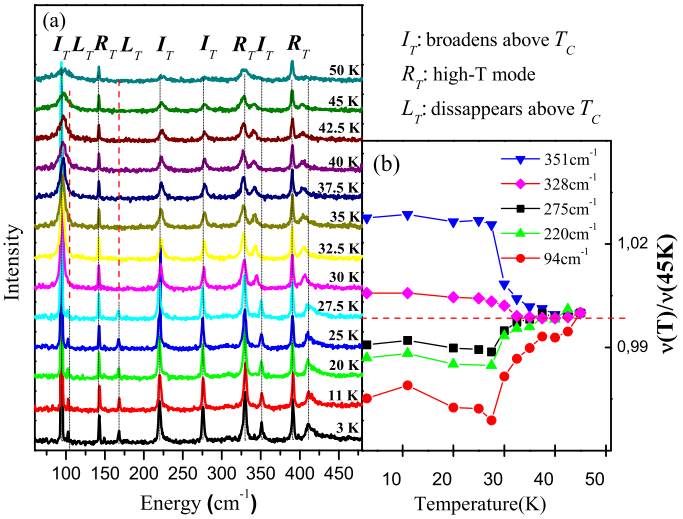

Figure 3.5: *(Color online) The temperature dependence of the Raman spectrum of TiOBr is depicted (an offset is added for clarity). The 3 modes present at all temperatures are denoted by the label R_T. The modes characteristic of the low temperature phase (disappearing at $T_{c1} = 28$ K) are labelled L_T, and the anomalous modes observed in both the low temperature and the intermediate phase are labelled I_T. The right panel (b) shows the behavior of the frequency of I_T modes, plotted renormalized to their frequency at 45 K. It is clear that the low-frequency modes shift to higher energy while the high-frequency modes shift to lower frequency.*

be compatible with all the space groups considered, and also with the monoclinic group with unique axis perpendicular to the TiO planes (Table 3.3(a)). Even though from the evidence it is not possible to rule out any of the other symmetries discussed, the conjecture that in the intermediate incommensurate phase the average crystal symmetry is already reduced, supports the description of the intermediate phase as a monoclinic group with a one-dimensional modulation[17], and moreover it explains the anomalous first-order character of the spin-Peierls transition at T_{c1}. The diagram shown in Fig.3.6 aims to visualize that the space group in the spin-Peierls state ($P2_1/m$) is a subgroup of the high temperature $Pmmn$ group, but not a subgroup of any of the possible intermediate phase space groups suggested (possible $P2/c$). This requires the phase transition at T_{c1} to be of first order, instead of having the conventional spin-Peierls second-order character.

Let us return to Fig.3.5(b) to discuss another intriguing vibrational feature of the intermediate phase. Among the modes characterizing the intermediate phase (I_T), the ones at low frequency shift to higher energy approaching T_{c2}, while the ones at high frequency move to lower energy, seemingly converging to a central frequency ($\simeq$300 cm^{-1} for both TiOCl and TiOBr). This seems to indicate an interaction of the phonons with some excitation around 300 cm^{-1}. Most likely

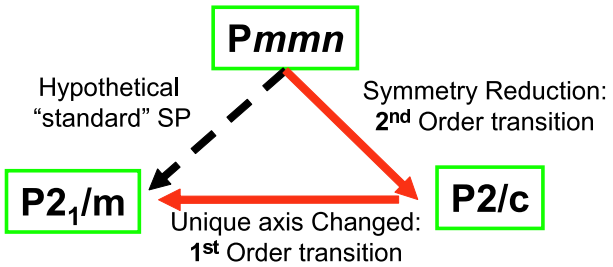

Figure 3.6: *(Color online) The average crystal symmetry of the intermediate phase is proposed to be monoclinic with the unique axis parallel to the c−axis of the orthorhombic phase. Hence the low temperature space group is not a subgroup of the intermediate phase, and the transition to the spin-Peierls phase is consequently of first order.*

this is in fact arising from a strong, thermally activated coupling of the lattice with the magnetic excitations, and is consistent with the pseudo-spin gap observed in NMR experiments[5, ?] of ≈430 K (≃300 cm^{-1}).

3.3.3 Magnetic Interactions

As discussed in the introduction, due to the shape of the singly occupied $3d$ orbital, the main magnetic exchange interaction between the spins on the Ti ions is along the crystallographic $b-$direction. This, however, is not the only effective magnetic interaction. In fact, one also expects a superexchange interaction between nearest and next-nearest neighbor chains (J_2 and J_3 in the insert of Fig.3.7(a))[21]. The situation of TiOX is made more interesting by the frustrated geometry of the interchain interaction, where the magnetic coupling J_2 between adjacent chains is frustrated and the exchange energies can not be simultaneously minimized. Table V reports the exchange interaction values for the three possible magnetic interactions calculated for TiOBr. These magnetic interactions were computed with a DFT Broken symmetry approach[22] using an atom cluster including the two interacting atoms and all the surrounding ligand atoms, in addition the first shell of Ti^{3+} ions was replaced by Al^{3+} ions and also included in the cluster. The calculations were performed with the Gaussian03 package[23] using the hybrid exchange-correlation functional B3LYP[24] and the 6-3111G* basisset.

Table 3.5: *Calculated Exchange interactions in TiOBr*

TiOBr
$J_1 = -250$ K
$J_2 = -46.99$ K
$J_3 = 11.96$ K

Although the computed value for the magnetic interaction along the $b-$axis is

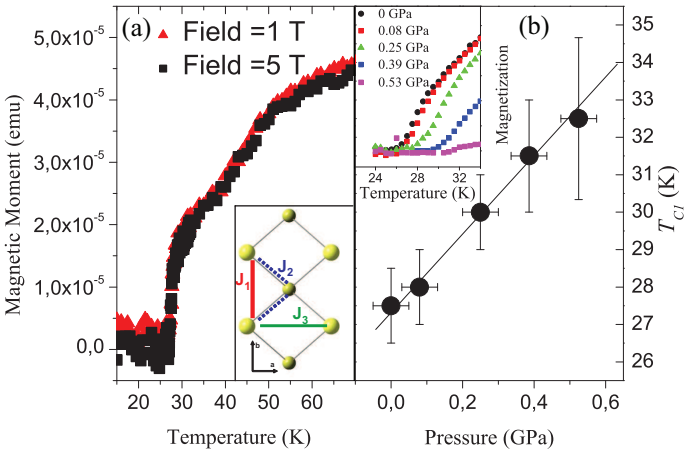

Figure 3.7: *(Color online) (a) Magnetization as a function of temperature measured with fields 1 T and 5 T (the magnetization measured at 1 T is multiplied by a factor of 5 to evidence the linearity). The inset shows the main magnetic interactions (see text). (b) Pressure dependence of T_{c1}. The transition temperature for transition to the spin-Peierls phase increases with increasing pressure. The inset shows the magnetization versus the temperature after subtracting the background signal coming from the pressure cell.*

half of the value obtained from the magnetic susceptibility fitted with a Bonner-Fisher curve accounting for a one-dimensional Heisenberg chain, it is possible to extract some conclusions from the ab-initio computations. The most interesting outcome of the results is that in addition to the magnetic interaction along the $b-$axis, there is a relevant interchain interaction ($J_1/J_2 = 5.3$) in TiOBr. Firstly, this explains the substantial deviation of the Bonner-Fisher fit from the magnetic susceptibility even at temperature higher than T_{c2}. Secondly, the presence of an interchain interaction, together with the inherent frustrated geometry of the bilayer structure, was already proposed in literature[14] in order to explain the intermediate phase and its structural incommensurability.

The two competing exchange interactions J_1 and J_2 have different origins: the first arises from direct exchange between Ti ions, while the second is mostly due to the superexchange interaction through the oxygen ions[21]. Thus, the two exchange constants are expected to depend differently on the structural changes induced by hydrostatic pressure, J_1 should increase with hydrostatic pressure (increases strongly with decreasing the distance between the Ti ions), while J_2 is presumably weakly affected due only to small changes in the Ti–O–Ti angle (the compressibility estimated from the lattice dynamics simulation is similar along the a and b crystallographic directions). The stability of the fully dimerized state is reduced by the presence of an interchain coupling, so that T_{c1} is expected to be correlated to J_1/J_2. Pressure dependent magnetic experiments have been performed to monitor the change of T_{c1} upon increasing hydrostatic pressure.

The main results, shown in Fig.3.7, indeed is consistent with this expectation: T_{c1} increases linearly with pressure; unfortunately it is not possible to address the behavior of T_{c2} from the present measurements.

3.3.4 Electronic Excitations and Comparison with VOCl

The nature of the complex phase diagram of TiOX was originally tentatively ascribed to the interplay of spin, lattice and orbital degrees of freedom[8]. Only recently, infrared spectroscopy supported by cluster calculations excluded a ground state degeneracy of the Ti d orbitals for TiOCl, hence suggesting that orbital fluctuations can not play an important role in the formation of the anomalous incommensurate phase[25, 26]. Since the agreement between the previous cluster calculations and the experimental results is not quantitative, the energy of the lowest $3d$ excited level is not accurately known, not allowing to discard the possibility of an almost degenerate ground state. For this reason a more formal cluster calculation has been performed using an embedded cluster approach. In this approach a TiO2Cl4 cluster was treated explicitly with a CASSCF/CASPT2 quantum chemistry calculation. This cluster was surrounded by eight Ti^{3+} TIP potentials in order to account for the electrostatic interaction of the cluster atoms with the shell of the first neighboring atoms. Finally, the cluster is embedded in a distribution of point charges fitting the Madelung's potential produced by the rest of the crystal inside the cluster region. The calculations were performed using the MOLCAS quantum chemistry package[27] with a triple quality basis set; for the Ti atom polarization functions were also included. The calculations

Table 3.6: *Crystal field splitting of $3d^1$ Ti^{3+} in TiOCl and TiOBr (eV).*

	TiOCl	TiOBr
xy	0.29-0.29	0.29-0.30
xz	0.66-0.68	0.65-0.67
yz	1.59-1.68	1.48-1.43
$x^2 - r^2$	2.30-2.37	2.21-2.29

reported in Table 3.6, confirmed the previously reported result[25] for both TiOCl and TiOBr. The first excited state d_{xy} is at 0.29-0.3 eV (> 3000 K) for both compounds, therefore the orbital degrees of freedom are completely quenched at temperatures close to the phase transition.

A comparison with the isostructural compound VOCl has been carried out to confirm that the phase transitions of the TiOX compounds are intimately related to the unpaired S=1/2 spin of the Ti ions. The V^{3+} ions have a $3d^2$ electronic configuration. Each ion carries two unpaired electrons in the external d shell, and has a total spin of 1. The crystal field environment of V^{3+} ions in VOCl is similar to that of Ti^{3+} in TiOX, suggesting that the splitting of the degenerate d orbital could be comparable. The electrons occupy the two lowest

t_{2g} orbitals, of $d_{y^2-z^2}$ (responsible for the main exchange interaction in TiOX) and d_{xy} symmetry respectively. Where the lobes of the latter point roughly towards the Ti^{3+} ions of the nearest chain (Table 3.6). It is therefore reasonable to expect that the occupation of the d_{xy} orbital in VOCl leads to a substantial direct exchange interaction between ions in different chains in VOCl and thus favors a two-dimensional antiferromagnetic order. Indeed, the magnetic susceptibility is isotropic in the plane at high temperatures and well described by a quadratic two-dimensional Heisenberg model, and at $T_N = 80$ K VOCl undergoes a phase transition to a two-dimensional antiferromagnet[29].

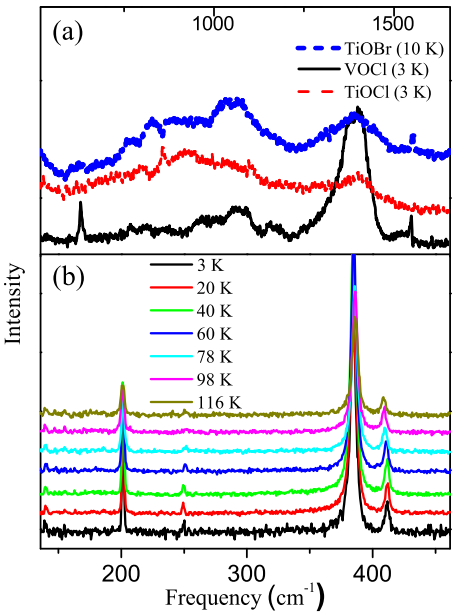

Figure 3.8: *(Color online) Raman scattering features of VOCl. (a) High energy scattering of TiOCl/Br and VOCl, and (b) temperature dependence of the vibrational scattering features of VOCl. No symmetry changes are observed at $T_N = 80$ K.*

The space group of VOCl at room temperature is the same as that of TiOX in the high temperature phase (Pmmn), and, as discussed in the previous section, three A_g modes are expected to be Raman active. As shown in Fig.3.8(b), three phonons are observed throughout the full temperature range ($3 - 300$ K), and no changes are observed at T_N. The modes observed are consistent with the prediction of lattice dynamics calculations (Table 3.1).

In the energy region from 600 to 1500 cm^{-1}, both TiOBr and TiOCl show a similar highly structured broad scattering continuum, as already reported in literature[15, 19]. The fact that the energy range of the anomalous feature is consistent with the magnetic exchange constant in TiOCl (J=660 K) suggested

at first an interpretation in terms of two-magnon Raman scattering [15]. Later it was shown that the exchange constant estimated for TiOBr is considerably smaller (J=406 K) with respect to that of TiOCl while the high energy scattering stays roughly at the same frequency. Even though the authors of ref.[19] still assigned the scattering continuum to magnon processes, it seems clear that the considerably smaller exchange interaction in the Br compound (J=406 K) falsifies this interpretation and that magnon scattering is not at the origin of the high energy scattering of the two compounds. Furthermore, the cluster calculation (Table 3.6) clearly shows that no excited crystal field state is present in the energy interval considered, ruling out a possible orbital origin for the continuum. These observations are further strengthened by the observation of a similar continuum scattering in VOCl (see fig. 3.8(a)) which has a different magnetic and electronic nature. Therefore, the high energy scattering has most likely a vibrational origin. The lattice dynamics calculations, confirmed by the experiments, show that a "high" energy mode ($\simeq$600 cm^{-1}) of symmetry B_{3g} (Table 3.1) is expected to be Raman active in the σ_{yz} polarization. Looking back at Fig.3.3, the inset shows the measurements performed with the optical axis parallel to the TiOX plane, where the expected mode is observed at 598 cm^{-1}. The two phonon process related to this last intense mode is in the energy range of the anomalous scattering feature and has symmetry A_g ($B_{3g} \otimes B_{3g}$). The nature of the anomalies observed is therefore tentatively ascribed to a multiple-phonon process. Further detailed investigations of lattice dynamics are needed to clarify this issue.

3.4 Conclusion

The symmetry of the different phases has been discussed on the basis of inelastic light scattering experiments. The high temperature Raman experiments are in good agreement with the prediction of the group theoretical analysis (apart from one broad mode which is ascribed to pre-transitional fluctuations). Comparing group theoretical analysis with the polarized Raman spectra clarifies the symmetry of the spin-Peierls phase and shows that the average symmetry of the incommensurate phase is different from both the high temperature and the SP phases. The conjecture that the intermediate phase is compatible with a different monoclinic symmetry (unique axis perpendicular to the TiO planes) could explain the anomalous first-order character of the transition to the spin-Peierls phase. Moreover, an anomalous behavior of the phonons characterizing the intermediate phase is interpreted as evidencing an important spin-lattice coupling. The susceptibility measurements of TiOBr show that T_{c1} increases with pressure, which is ascribed to the different pressure dependence of intrachain and interchain interactions. Finally, we compared the TiOX compounds with the "isostructural" VOCl. The presence of the same anomalous high energy scattering feature in all the compounds suggests that this feature has a vibrational origin rather than a magnetic or electronic one.

3.5 Appendix: Details of the spring model calculation

The spring model calculation reported in the chapter, was carried out using the software for lattice-dynamical calculation UNISOFT[30] (release 3.05). In the calculations the Born-von Karman model was used; here the force constants are treated as model parameters and they are not interpreted in terms of a special interatomic potential. Only short range interactions between nearest neighbor ions are taken into account. Considering the forces to be central forces, the number of parameters is reduced to two for each atomic interaction: the longitudinal and transversal forces respectively defined as $L = \frac{d^2V(\bar{r}_{i,j})}{dr^2}$ and $T = \frac{1}{r}\frac{dV(\bar{r}_{i,j})}{dr}$. A custom made program was interfaced with UNISOFT to optimize the elastic constants. Our program proceeded scanning the n dimensional space (n = number of parameters) with a discrete grid, to minimize the squared difference between the calculated phonon frequencies and the measured experimental frequencies for TiOBr, taken from both Raman and infrared spectroscopy. The phonon frequencies of TiOCl and VOCl were obtained using the elastic constants optimized for TiOBr and substituting the appropriate ionic masses. The optimized force constants between different atoms are reported in N/m in the following Table.

Table 3.7: *Elastic constants used in the spring model calculation. The label numbers refer to Fig. 3.9, while the letters refer to the different inequivalent positions of the ions in the crystal.*

Number	Ions	Longitudinal (L) (N/m)	Transversal (T) (N/m)
1	Ti(a)-Ti(b)	18.5	32.7
2	Ti(a)-O(a)	18.5	11.1
3	Ti(a)-O(b)	53.1	9.5
4	Ti(a)-X(a)	29.0	4.4
5	O(a)-O(b)	20.6	7.3
6	X(a)-O(a)	18.5	3.5
7	X(a)-X(b)	11.7	0.7

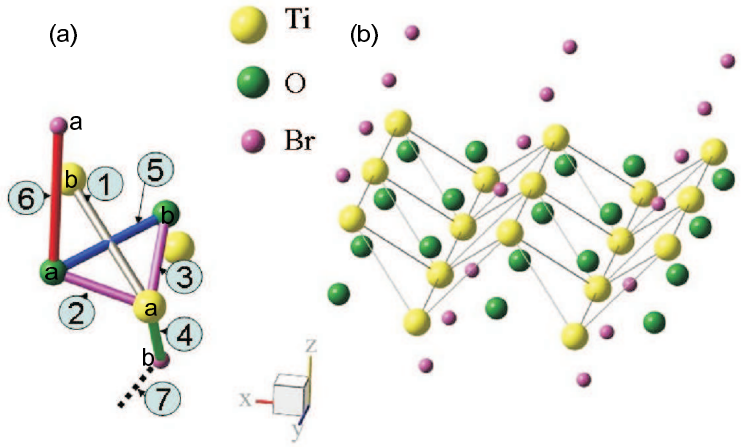

Figure 3.9: *(Color online) Sketch of the bilayer structure (b) and of the interactions introduced in the spring model calculation (a).*

Bibliography

[1] M. Imada, A. Fujimori, and Y. Tokura, Rev. Mod. Phys. **70**, 1039 (1998).

[2] L. Pisani, R. Valenti, B. Montanari, and N. M. Harrison, Phys. Rev. B **76**, 235126 (2007).

[3] E. Dagotto, Rep. Prog. Phys. **62**, 1525 (1999).

[4] V. Kataev, J. Baier, A. Möller, L. Jongen, G. Meyer, , and A. Freimuth, Phys. Rev. B **68**, 140405 (2003).

[5] T. Imai and F. C. Choub, cond-mat **0301425** (2003), URL `http://arxiv.org/abs/cond-mat/0301425`.

[6] C. H. Maule, J. N. Tothill, P. Strange, and J. A. Wilson, J. Phys. C **21**, 2153 (1988).

[7] A. Seidel, C. A. Marianetti, F. C. Chou, G. Ceder, and P. A. Lee, Phys. Rev. B **67**, 020405 (2003).

[8] G. Caimi, L. Degiorgi, P. Lemmens, and F. C. Chou, J. Phys. Cond. Mat. **16**, 5583 (2004a).

[9] R. J. Beynon and J. A. Wilson, J. Phys. Cond. Mat. **5**, 1983 (1993).

[10] D. L. Rousseau, R. P. Bauman, and S. P. S. Porto, J. of Raman Spectroscopy **10**, 253 (1981).

[11] G. Caimi, L. Degiorgi, N. N. Kovaleva, P. Lemmens, and F. C. Chou, Phys. Rev. B **69**, 125108 (2004b).

[12] M. Shaz, S. van Smaalen, L. Palatinus, M. Hoinkis, M. Klemm, S. Horn, and R. Claessen, Phys. Rev. B **71**, 100405 (2005).

[13] J. Hemberger, M. Hoinkis, M. Klemm, M. Sing, R. Claessen, S. Horn, and A. Loidl, Phys. Rev. B **72**, 012420 (2005).

[14] R. Rückamp, J. Baier, M. Kriener, M. W. Haverkort, T. Lorenz, G. S. Uhrig, L. Jongen, A. Möller, G. Meyer, and M. Grüninger, Phys. Rev. Lett. **95**, 097203 (2005a).

[15] P. Lemmens, K. Y. Choi, G. Caimi, L. Degiorgi, N. N. Kovaleva, A. Seidel, and F. C. Chou, Phys. Rev. B **70**, 134429 (2004).

[16] L. Palatinus, A. Schoenleber, and S. van Smaalen, Acta Cryst. C **61**, 148 (2005).

[17] S. van Smaalen, L. Palatinus, and A. Schoenleber, Phys. Rev. B **72**, 020105(R) (2005).

[18] A. Schoenleber, S. van Smaalen, and L. Palatinus, Phys. Rev. B **73**, 214410 (2006).

[19] P. Lemmens, K. Y. Choi, R. Valenti, T. Saha-Dasgupta, E. Abel, Y. S. Lee, and F. C. Chou, New Journal of Pysics **7**, 74 (2005).

[20] T. Sasaki, T. Nagai, K. Kato, M. Mizumaki, T. Asaka, M. Takata, Y. Matsui, H. Sawa, and J. Akimitsu, Sci. Tech. Adv. Mat. **7**, 17 (2006).

[21] R. Macovez (2006), unpublished.

[22] L. Noodleman and J. G. Norman, J. Chem. Phys. **70**, 4903 (1979).

[23] M. J. F. et al. (2004).

[24] A. D. Becke, J. Chem. Phys. **98**, 5648 (1993).

[25] R. Rückamp, E. Benckiser, M. W. Haverkort, H. Roth, T. Lorenz, A. Freimuth, L. Jongen, A. Möller, G. Meyer, P. Reutler, et al., New Journal of Physics **7**, 1367 (2005b).

[26] D. V. Zakharov, J. Deisenhofer, H. A. K. von Nidda, P. Lunkenheimer, J. Hemberger, M. Hoinkis, M. Klemm, M. Sing, R. Claessen, M. V. Eremin, et al., Phys. Rev. B **73**, 094452 (2006).

[27] G. Karlstro, R. Lindh, P. Malmqvist, B. Roos, U. Ryde, V. Veryazov, P. Widmark, M. Cossi, B. Schimmelpfennig, P. Neogrady, et al., Comput. Mater. Sci. **28**, 222 (2003).

[28] C. A. Kuntscher, S. Frank, A. Pashkin, H. Hoffmann, A. Schönleber, S. van Smaalen, M. Hanfland, S. Glawion, M. Klemm, et al., cond-mat **0718**, 4126v1 (2007).

[29] A. Wiedenmann, J. R. Mignod, J. P. Venien, and P. Palvadeau, JMMM **45(2-3)**, 275 (1984).

[30] G. Eckold, *Unisoft - a program package for lattice dynamical calculations: Users manual* (1992).

Chapter 4

Time Resolved Raman Spectroscopy

The aim of this chapter is to describe the experimental setups used in the different sections of this thesis.

The first part will be devoted to give a brief description of the continuous wave (CW) Raman experiment and will briefly discuss the characterization of the setup. The rest of the chapter is devoted to give an overview on the different experiments performed while studying the dynamical Raman response. We will start with an overview of the basic idea of the dynamical Raman experiments, reviewing the literature on the subject and introducing the main technical and fundamental limitations of the technique. We will continue by describing the two different approaches we have been using to access the fast Raman response (μs time scale) of the organic salt EdoTTF-PF_6 and the ultrafast Raman response on a silicon single crystal (ps time scale). We will give a full characterization of the two setups and we will conclude with some still preliminary results.

4.0.1 A Bit of History

The discovery of Kerr-Lens mode locking in the beginning of the 90s[1] has boosted the field of ultrafast spectroscopy. The possibility of studying ultrafast dynamics with relatively cheap table-top experiments has in the last 15 years stimulated the development of the dynamical version of most of the traditional "equilibrium" spectroscopies, ranging from time resolved photoemission, reflectivity, absorption, ellipsometry, dichroism, magneto-optical Kerr effect, and many others[2, 6, 7]. Over the past few years, topics of major interest ranging from optically induced phase transitions, non-thermal processes, and ultrafast optical switching behavior have been addressed, to mention only the condensed matter physics ones. These techniques generally give a good insight into the electronic and/or charge

properties, but usually lack information on the structural characteristic. An exception to this is coherent phonon generation, where in some particular cases the coherent response of the material gives access to structural information[8]. To address more specifically the ultrafast structural properties, there are several groups concentrating on the development of time resolved x-ray (or electron) diffraction experiments at synchrotrons[9, 13, 16] or XFEL facilities and even by using table top laser systems[10].

Time resolved Raman spectroscopy (TRRAS) is a cheap, promising and powerful alternative tool for studying structural, magnetic and possibly electronic dynamics. Even though it is not directly sensitive to the atomic positions but to the symmetry, through the analysis of low energy excitation on ultrafast time scale, TRRAS allows us to extract independent information on structural, magnetic and electronic properties. There are the peculiar and quite unique properties of TRRAS. i) The first is that by monitoring the ratio stokes/antistokes (in the limits described in the introduction), it is possible to measure directly the temperature of the excitation investigated, and thereby to disentangle the thermodynamics of the different excitations. ii) The second one is that TRRAS allows us to measure the "strength" of the crystalline potential in real time (see Chapter 5). Through the frequency of the excitation, it is possible to follow directly how the perturbation is modifying the energy landscape in real time and, thereby, to address in real time the mechanism of the evolution.

In this sense TRRAS provides a unique tool to study thermal vs non-thermal processes, with the possibility of decoupling coherent effects from the thermally induced ones.

In the last 25 years, different groups have tried to develop different schemes to achieve a dynamical Raman spectroscopy, but none have ever managed to get a reliable configuration applicable to different scientific cases. Mentioned here are only a few of the different schemes attempted. Von der Linde et. al. [14] with a system based on a synchronously mode-locked rhodamine 6G dye laser were able to measure directly the time evolution of the non-equilibrium population of the *incoherent* optical phonon on GaAs. A few years later, using a similar system with improved time resolution, J. A. Kash et. al. were able to temporally resolve the growth of the optically induced nonequilibrium LO-phonon in GaAs. As mentioned before with the discovery of Ti:sapphire passive mode-locking techniques, most of the dynamical spectroscopies were improved and setups making use of the new lasers were developed. On the contrary, the development of a time resolved Raman spectroscopy based on Ti:sapphire lasers has been inhibited and slow. This is, in the author opinion, due to two main reasons. The first is that kerr lens mode locking works "easily and stably" in the femtosecond regimes, suggesting that a high time resolution could be achieved ($<$ 100fs). It is clear though that this is achieved at the cost of frequency resolution, so that excitation in the low energy region ($< 100\text{cm}^{-1}$) would be hidden under the spectral width of the laser pulse. This fact, as low energy excitations are *the key* in thermodynamics, would strongly limit the thermodynamic insight of the

technique. The second, and maybe less relevant reason, is that Ti:sapphire mode-locked lasing is characterized by the presence of a background luminescence of the order of 10^{-6} with respect to the fundamental laser line (spread on all Ti:sapphire band). Considering that the characteristic cross section of a Raman experiment is of the $10^{-8,-10}$ order, this makes necessary some "optical precaution" before using Ti:sapphire lasers for Raman experiments.

4.1 Our Setups

4.2 CW Raman Setup

For the CW Raman experiments the samples were mounted in an optical flow cryostat, with a temperature stabilization better than 0.1 K in the range from 2.6 K to 500 K (Oxford-Microstat). The Raman measurements were performed using a triple-grating micro-Raman spectrometer (T64000 - Jobin Yvon), equipped with a liquid nitrogen cooled CCD. The resolution of the spectrometer was depending on the wave length, but better than 2cm^{-1}in all the frequency range we investigated. The spectrometer has been used mainly in the subtractive configuration fig.3.3(a), allowing us to investigate a wide spectral range from $\simeq$4cm^{-1}up to 9000cm^{-1}. The low frequency limit was depending on the sample characteristics and on the light polarization investigated. Typically we were able to resolve low energy excitation down to 5-8cm^{-1}in the parallel polarizations ($x(yy)x$ in the Porto notation) and to 3-5cm^{-1}in perpendicular polarizations ($x(yz)x$). The spectrometer was coupled to a confocal microscope fig.3.3(b). The spatial resolution of the microscope is variable changing the objective focal distance. The most of the experiment were performed with a long focal distance 50x objective (LMPLFLN-50x) allowing us to access the samples placed inside the cryostat. The size of the beam focus was tested using a knife-edge technique using a custom made aluminium thin layer (>100nm) deposited on a microscope glass and mounted on a micrometer translation stage. The measured diameter was less than 5μm. The excitation line used was mainly a diode pump, frequency doubled Nd:YVO_4 (Coherent - verdiV5). The beam diameter was about 3mm with a divergence of about 0.5mrad.

The overall technical characteristic and capabilities of the system we set up are the following:

-Spectral Range 4-9000cm^{-1}(the lower limit depend strongly on the sample characteristics and on the polarization configuration)

-Energy resolution <2cm on all the range and $\simeq$1cm^{-1}in the near infrared

-Excitation lines: 532 and 676nm (+Ti Sapphire tunable from 750-850nm)

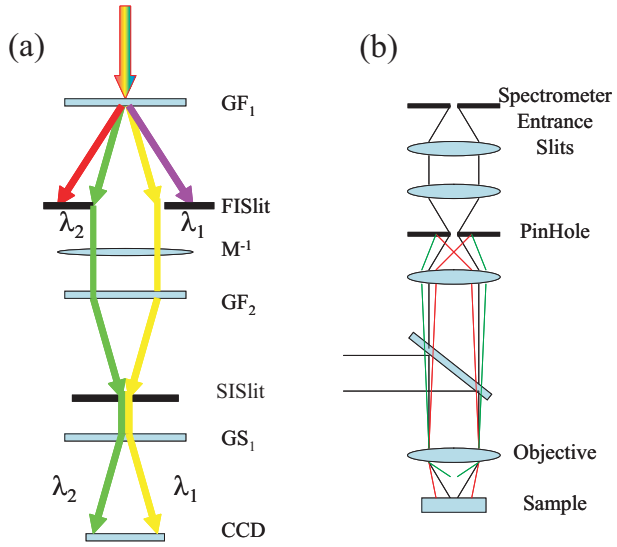

Figure 4.1: *(a) Conceptual optical scheme of the subtractive configuration of the spectrometer. The first grating (GF1) spatially disperses the light, so that the first intermediate slit (FISlit) can select the spectral window we want to investigate (allowing us to block the laser line). The second grating (GF2) recombines the light containing only the spectral component we are interested, imaging the entrance slit on the second intermediate slit (SISlit). In a different chamber the light is once more dispersed by a third grating (GS1) on a CCD camera. (b) Optical scheme of the confocal microscopy. The configuration drawn allow to block most of the light scattered outside the beam focus.*

-Spatial Resolution $<5\mu m$ (depending on the objective)

-Temperature continuously variable from $2.5 - 500$ K (relative accuracy $\approx 0{,}1$ K)

4.2.1 Low Time and High Frequency resolution

The setup used for measuring the fast time resolved Raman of EdoTTF-PF_6 is described in Fig.4.2(a). It consist of an amplified Ti:Sapphire laser (Hurricane Spectraphysics) used as pump and a CW Nd:YVO_4 laser at 532nm (Coherent - verdiV5) used as probe. The probe pulse are produced through a mechanical chopper synchronized to the electronic of the pump laser (see next section for the chopper characteristics and production). The CW laser is focused un the chopper slits, so that only pulses of the continuous light are allowed through. The chopper has 60 counter (windows) on the external wheel so that the angular speed results 1/60 of the repetition rate of the pulsed laser $\omega \approx 16Hz$. The width of the slits is about 30μs that in time corresponds to a open-time-window of $\sim 6\mu$s. The convolution of the slit geometry with the laser spatial profile in the focus beam results in pulses of $\sim 10\mu$s. The delay between the pump and the probe pulses is

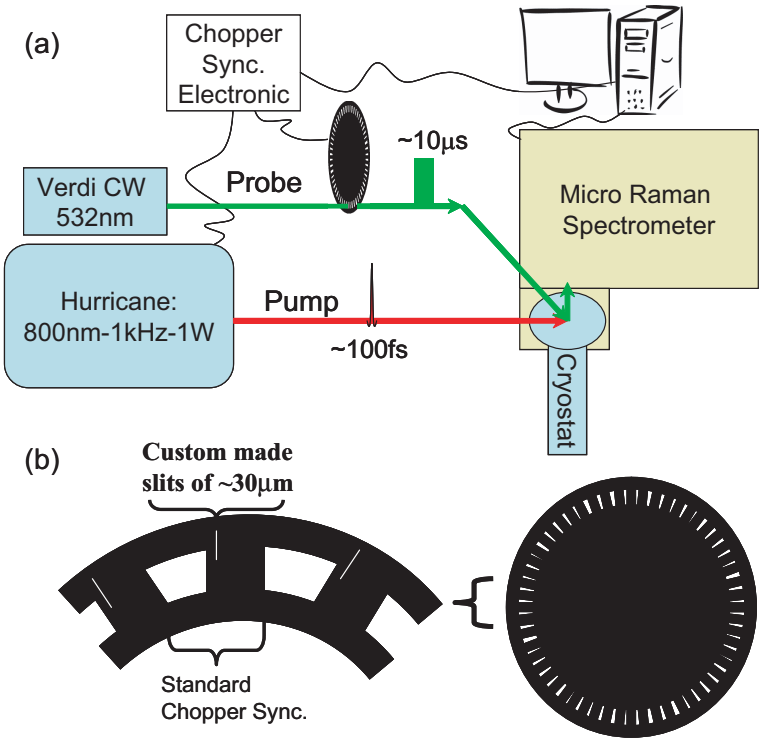

Figure 4.2: *(a)Sketch of the optical scheme of the experiment. An amplified Ti:Sapphire laser at 1kHz repetition rate and 800nm wavelength (Spectra Physics - Hurricane) it's used as pump, while the probe pulse it's obtained slicing a CW at 532nm with the custom produced mechanical chopper (b) produced as described in the text. The time delay between the pump and the probe is controlled through the electronic of the chopper.*

controlled via the phase between the chopper rotation and the reference triggering used for the synchronization. The frequency resolution of the system is the same as described for the continuous wave system.

Production of the chopper

To produce the chopper with the characteristics required, equally spaced (angularly spaced) fenditures of 30-40μm, with a constant phase respect to the chopper external periodicity, a new technique was implemented. A commercial chopper wheel was synchronized with the amplified Ti:Sapphire laser and the laser was focused with a short focal distance lens. The short focal distance allows us to achieve extremely high intensity, and to generate plasma in air. The plasma was

focussed on the syncronously rotating wheel so that the holes drilled in the metal would be equally spaced at the angular distance $\Delta\Theta = \omega * \Delta\ t$, where $\omega = 16Hz$ (1/60 of the laser repetition rate) and $\Delta\ t$=1ms (distance between two pulses). The chopper produced in this way have 60 equally spaced fenditures 30μm wide on the rotation period fig.4.2(b). This allow us to produce phase stable light pulses of 10μs time duration with 1kHz repetition rate.

4.2.2 High Time and Low frequency Resolution

The ultrafast Raman experiment were performed making use of a 80MHz Ti:sapphire laser (Mira 900). The laser was able to work in two different regimes, able to produce 100fs or 1,5ps pulses. The technique used to modelock the mira laser is known as the *Kerr Lens Modelocking*. The optical cavity is designed to utilize changes in the spatial profile of the laser produced by self focusing due to the optical Kerr effect in the active media, the Ti:spphire crystal. Making use of the maximized overlap between the pump gain profile and the cavity beam profile the cavity is designed to maximize the gain of the modelocked operation mode (the modelocked pulse having high peak intensity maximize the self focusing and it becomes the more stable lasing mode of the cavity: the mode locked is done passively). The main difference between the femtosecond and picosecond lasing cavities resides in the way the intracavity group dispersion is compensated. While in the femtosecond regime the cavity dispersion is compensated with the normal two prism configuration, in the picosecond regime the phase compensation is achieved via a Gires-Tournois interferometer end mirror cavity. For the detailed description of the two lasing modes of the Mira900 cavity we refer to the laser manual[20]. The setup described in the following part would work with both the lasing modes.

The setup of a dynamical Raman experiment able to access low energy excitations, whose statistic is expected to be more affected by the thermodynamic characteristic of the systems under investigation (see introduction), with a fast time response faced two main problems.

i) the first one is of technical nature. The general spectral characteristic of a Ti:sapphire laser is that, together with the laser pulses earlier described, a luminescence background is emitted on all Ti:sappphire luminescence band (that range from the visible to the near infrared). The intensity of the luminescence background is extremely weak respect to the laser one and therefore usually negligible for most of the spectroscopy applications (the background is $I_{Background} \approx 10^{-6} I_{Laser}$). This is not the case for Raman spectroscopy. Considering that the typical cross section of a Raman process is $10^{(-8)} - 10^{(-10)}$, respect to the excitation line, the background is expected to be much more intense than the Raman signal.

ii) The second more fundamental problem is due to the indetermination principle. A fast time response require broad laser spectra, and therefore strongly limit the accessibility to low energy excitations.

The system we have designed to trade off between time and frequency resolution and at the same time to solve the background problem is described in fig.4.3(a). The laser beam is spatially dispersed by an optical grating, sent to a spherical mirror, and back to the grating so that on the outgoing beam (after a second pass on the grating) the gaussian profile is restored. To cut the spectral window allowed a slit is placed on the dispersed beam. To avoid to introduce vertical cuts in the spectra (that would result in tails in the time profile) we used a slit consisting of two parallel screws, to obtain the effect of a soft spectral cut. Such a filter allowed us a continue tunability between frequency and time resolution. Fig.4.3 (b) show, as an example, a calculated spectra for High-Time-Low-Energy (red) and Low-Time-High-Energy (black) resolution.

After the spectral filter described the time dependence in our experiments is obtained with a standard pump&probe technique (Fig.4.3(c)). Making use of a beam splitter the beam is divided into two, one more intense (pump) and a second weaker (probe). The delay between the pump and the probe is controlled through a remote controlled delay line. The polarization and the intensity of the beams are controlled independently through $\lambda/2$ plates and neutral density filters. The pump and the probe beams are recombined with a second beam splitter and coupled into the Raman microscope. The scattered light is collected in a back scattering configuration and coupled into the Raman monocromator after a second polarizer allowing only the probe polarization through. To characterize the system we performed Time Resolved Raman measurements on Silicon.

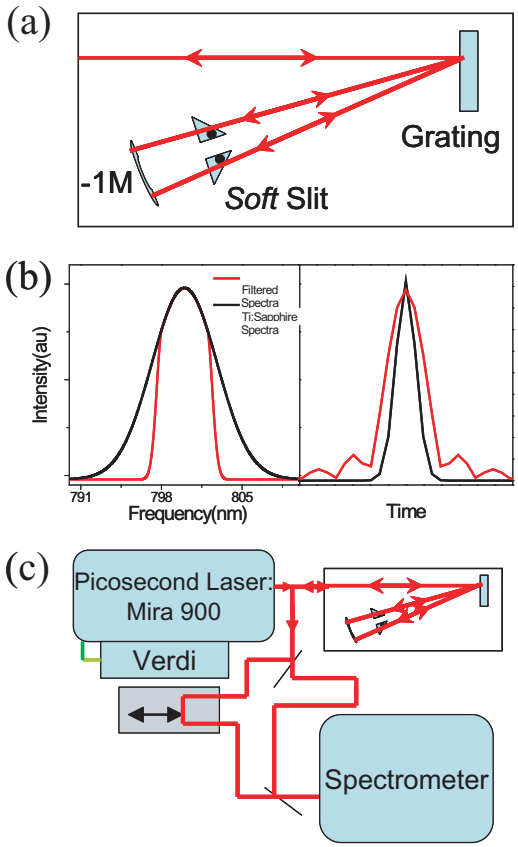

Figure 4.3: *(a) Optical scheme of the spectral filter designed. The laser beam is spatially dispersed by a grating (1200g/mm) (it's fourier transformed), a "soft" slit select the bandwidth, a spherical mirror reflect back all the spectra components at different angle, and finally a grating recompose all the spectral component restoring the gaussian beam profile (it does the antifourier transform of the pulses). The "soft" slit effect is desirable to avoid introducing step cuts in the spectral distribution, this would produce anomalous pulse-shape in the time profile of the pulses. A soft cut is achieved simply introducing a screw profile on the fenditure edges. (b) Relation between spectral and time distribution for to different openings of the spectral filter.(c) General layout of the pump and probe experiment.*

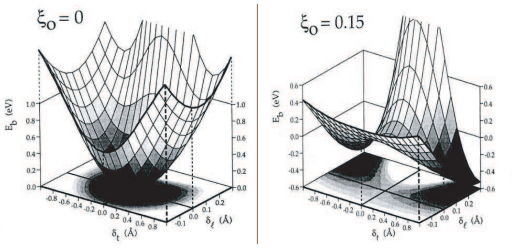

Figure 4.4: *Potential shape calculated for bulk silicon[12], with no electron excited in the conduction band (left) and with an excitation density 15% of the number of atoms. The picture is taken from the reference [12] (P. Stampfli, K. H. Bennemann, Copyright (1993) by the American Physical Society.).*

Silicon

The study of non thermal processes, optically induced phase transition and ultrafast optical switches is a topic of major interests in the last years of condensed matter physics. The dynamical properties of highly non equilibrium electron-hole plasmas generated with extremely short light pulses in insulating materials have been the subject of an enormous ensemble of scientific literature belonging to different research fields. From the fundamental point of view, the accessibility with relatively easy experiments to the ultrafast relaxation processes of highly non equilibrium plasmas could help developing a formulation of highly non equilibrium thermodynamics. Just to give an example of interdisciplinary interests, the exciton formation dynamics in magnetic field, analogue of electron-ion recombination in Hydrogen plasma, crucial for the behavior of fusion reactor, could be studied with a low energy "toy model" material as CuO[11]. Moving back to the silicon case, the role of the electron/hole plasma in initiating and driving processes like optically induced melting have been clarified in different experimental and theoretical works[12, 4, 5, 3]. To illustrate this we consider Fig.4.4 taken from Ref.[12]. It show the calculated crystal potential as a function on the atomic position. In the left panel (Fig.4.4(a)) the crystal potential calculated at the equilibrium is depicted, while the right panel (Fig.4.4(b)) reports the one calculated with an electronic excitation density of 15% respect to the atomic density. It appear clear that, while the unexcited crystal (a) is stable (the crystal potential has a minimum at the atom position), the excited one (b) becomes unstable and the diamond structure is no longer stable. This indicate that the silicon single crystal under this excitation conditions is bound to undergo to a nonthermal melting, on a time scale faster than the one required for energy transfer from the electrons to the lattice. This is what we would call a non thermal phenomena.

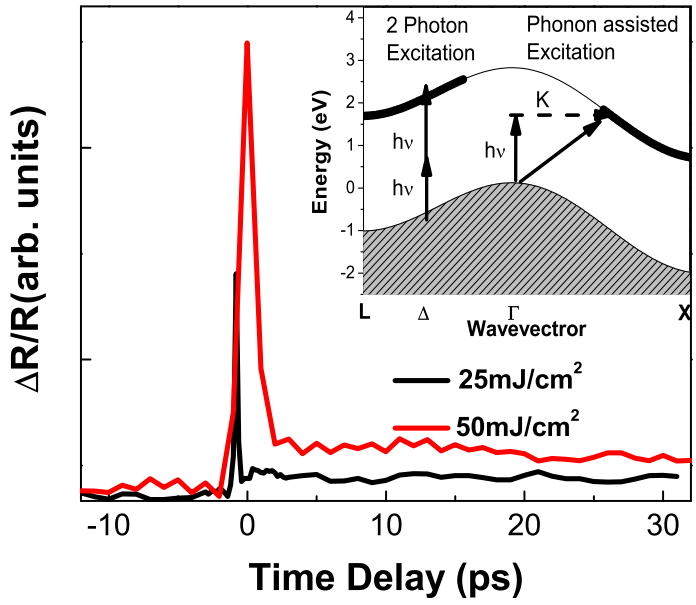

Figure 4.5: *(b)Time resolved reflectivity in response of Silicon, with two different excitation intensity. The insert depict the excitation processes possible: two photon absorption (in the Γ point, or linear phonon assisted absorption in the X valley.)*

For excitation densities below the melting threshold different optical measurements have been performed to investigate the ultrafast fast carrier dynamics on silicon. The following picture has emerged[18, 19, 17]. At the early time after irradiation momentum relaxing scattering processes (carrier-carrier and carrier-phonon) dephase the excited carrier states on a time scale substantially faster than 100fs. Carrier-carrier scattering processes result in a well defined electron temperatures within 100-300fs. Electron-phonon scattering also thermalize the excited carrier with the lattice, within a few hundred fs. On a longer time scale bulk and surface recombination processes operate to transfer the electron back to the valence band, and at the same time, together with these "local" dynamical processes, diffusion or band bending induced transport may occur.

Fig.4.5 shows two time resolved reflectivity traces for two different excitation intensity (25 and 50 mJ/cm^2). The reflectivity traces were measured with a 1kHz

Ti:Sapphire amplified system. The pulse length is 150fs. The two traces clearly show a different response for the two excitation energies. The results obtained are consistent with those reported previously[17]. Our measurements confirm for excitation energy ≈1.5eV the existence of two different excitation regimes for low and high pump fluency. The first peculiar thing to notice is the different ultrafast relaxation time for the two regimes. For low excitation power (black curve) the ultrafast coherent peak relaxes following the pulse autocorrelation, and the reflectivity traces shows a minimum and a subsequent raise leading to a second maximum ≈1ps after the pump pulse. In the high pump power regime (red curve) the reflectivity relaxation appear to be slower with an observed decaying time of a few picosecond. On the long time scales (>10ps) both traces converge to an slow relaxing offset lasting more than the explored time.

The different behavior of the reflectivity traces can be understood in terms of the different leading excitation processes in the two regimes. As sketched in the insert of Fig.4.5 the carrier excitation processes for intense pump are dominated by two photon absorption in the conduction band (left sketch of the insert of Fig.4.5), and therefore will excite electron on an extended region of the Brillouin zone. On the contrary in the low intensity limit the leading absorption processes as for linear spectroscopy is phonon assisted (right sketch of the insert in Fig.4.5) and will excite carriers in a limited part of the Brillouin zone close to the X point. The reflectivity changes are measured at 800nm, where the transient response function is dominated by the population dynamics in the X valley of the conduction band. In this picture, the electrons excited only in the X valley (low intensity) thermalize within few hundreds fs, leading the fast response in the reflectivity traces to decay on the same scale (Fig.4.5, black curve). On the other end, carriers excited on an extended region of the Brillouin zone (high fluency) relax into the X valley of the conduction band with a "slow" (few ps) momentum exchanging scattering processes and only subsequently can give rise to a thermally distributed population. This is at the origin of the different response for different excitation power regime.

On the longer time scale (from 10ps to more than 100ps) the optical response is dominated by the dynamics of the electron at the X point of the Brillouin zone by now in thermal equilibrium with the lattice. Fig.4.6(a) sketches the two main electron hole recombination processes. The electron-hole recombination via phonon excitation sketched (on the left) will result in lattice heat, while recombination of the Auger type are not expected to contribute to the lattice heat, but only to the electronic heat. On the same time scale heat diffusion and/or band bending induced transport could take place.

Making use of time resolved Raman spectroscopy we investigate how the carrier's slow de-excitation affect the lattice temperature for excitation processes dominated by the direct phonon assisted absorption (low peak energy). The excitation intensity used is $\simeq$15mJ/cm^2. This value would correspond (with a 100 fs

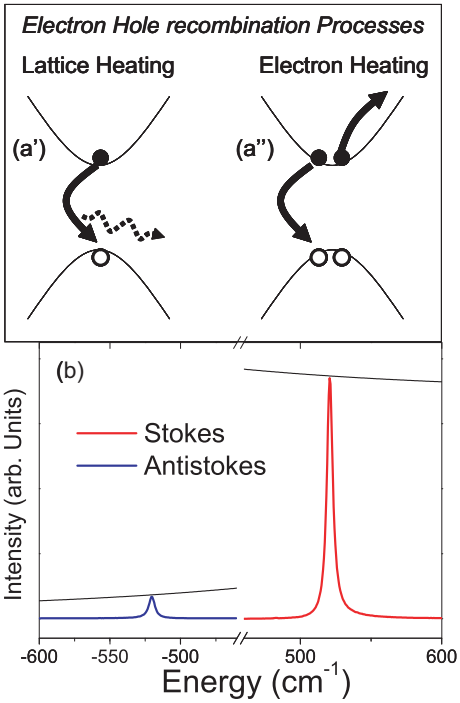

Figure 4.6: *(a) Sketch of the two electron hole recombination processes. The electron hole recombination mediated by phonon excitation (a') results in lattice heating, while Auger relaxation (a") will cause only the heating of the electronic gas. (b) Continuous Wave Raman feature of Silicon. The black curves represent the statistic of Stokes and Antistokes process.*

pulse) to the low intensity region. The excitation dynamics investigated are therefore mostly direct phonon-assisted absorption, and the two-photon contribution is negligible.

The Raman experiments where performed on a silicon wafer of thickness 254-300μm P doped with 5% of Boron ions Covered with 500nm SiO_2. The face Orientation was (1,0,0). The full representation of the vibrational mode of silicon is $\Gamma = F_{1u} + F_{2g}$ of whom only the F_{2g} is Raman active. Fig.4.6(b) shows the Stokes and Antistokes line of this vibrational mode obtained with the CW Raman set-up. From the ratio between the two it is possible to determine the temperature (in this case room temperature) with an accuracy of $\pm 3K$. The black lines are the calculation of the expected relative intensity of stokes and Antistokes ($n(\omega, T)$ for the Antistokes and $n(\omega, T) + 1$ for the Stokes line - see introduction).

The pump and the probe measurement were performed at room temperature (293K) into a microscope with a 100X magnification objective. The spot size was measured to be $1\mu m^2$. The pump power on the sample was 10mW, while the

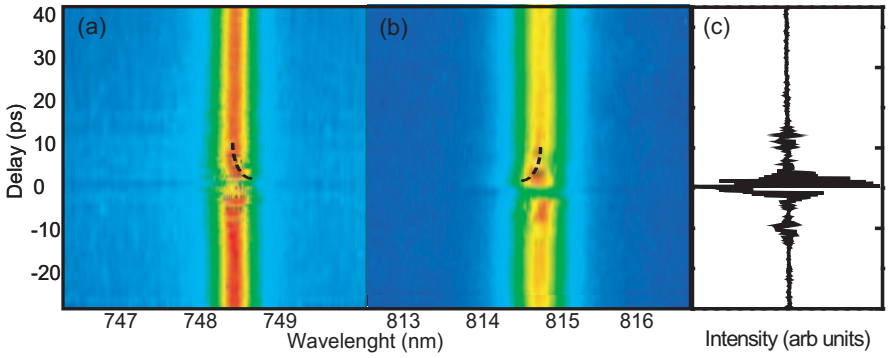

Figure 4.7: *(a,b)Time dependent Antistokes and Stokes Raman mode of silicon. (c) Autocorrelation measured at the sample position with parallel polarization.*

probe beam was 1mW. The excitation power result then to be 0.13nJ per pulse resulting in an excitation density of 15mJ/cm^2. The two beam were perpendicularly polarized and the scattered light was analyzed through a polarizer, so to select only the scattered light from the probe beam. The polarization control, due to the quality of the polarizer and the short focal distance of the objective, was $\approx 3-4$ %, so that the scattered light collected would come 30% from the pump beam (being the pump beam 10 times more intense than the probe one).

Fig.4.5 (a,b) report the Antistokes and Stokes lines for different time delays between pump and probe. The dynamical Raman response shows quite clearly an interference pattern when the pump and probe are overlapped in time. The pump and probe beams are orthogonally oriented and therefore they shouldn't displace any interference. As a consistency check we measure directly the reflected light in the spectrometer for overlapped pulses, and no interference was observed. Hence, the coherent feature observed is ascribed to the interference of the Raman scattered light from the pump and the one scattered from the probe not being completely orthogonal in the focus of the objective. The transient Raman features lasts for a time comparable to the autocorrelation between two pulses (with parallel polarization) at the sample position (Fig.4.7 (c)), making clear that the time duration of the "coherent artifact" matches the autocorrelation between the laser pulses.

As shown in the beginning of the chapter (Fig.4.4) ab-initio calculations suggest that the lattice potential for Silicon single crystal becomes softer if the conduction band is populated, to the extent where a critical density of excitation is reached and the crystal form is no longer stable. With a sufficiently high population of the conduction band the equilibrium atom position is no longer a stable

equilibrium position of the crystal potential. A phonon softening in the first few ps after irradiation was also observed measuring the coherent response in ultrafast reflectivity[7] and was interpreted as the "dressing of a quasi-particle", the real time dressing of an excitation with manybody interactions[7].

An overestimation for the electron density we reach in our measurements is 8-10% assuming that all the energy absorbed create excited electrons with a lifetime longer than the pulse duration. No non-thermal melting is expected under such condition. As shown in Figure 4.7(a,b)(exaggerate by the dashed black line), within the autocorrelation curve the central frequency of the phonon shift to lower frequency (both in the stokes and antistokes measurements). Indicating that the excitation of electrons in the conduction band results in a perturbation on the lattice eigenfrequency. As made clear by the dashed black lines, the phonon softening appears only at positive delay (still within the autocorrelation). This seem to indicate a dependence of the of the phonon perturbation on the number of excited electrons $n(t)$: $n(t) = \int_{-\infty}^{t} f(t')e^{-\frac{t-t'}{\tau}}dt'$, where $f(t')$ is the intensity profile of the pump pulse and τ is the decaying time of the excitation. It is clear from this expression that the function $n(t)$ will have a delayed peak respect to $f(t)$, so that the phonon softening will become more visible only in the positive part of the autocorrelation between pump and probe pulses. Unfortunately, due to the interference present in the measurements, no quantitative analysis can be performed and the information we can extract for the fast time scale (the first 5ps after irradiation) is of qualitative nature. Nevertheless the qualitative softening of the phonon frequency observed, seem to indicate a softening of the crystal potential approaching the non-thermal melting.

Fig. 4.8(a) depict the time resolved Raman spectra reported in Fig.4.7(b) subtracted of the average of the negative time curves. The color scale goes from the blue of the negative values to the yellow/red of the positive ones. This plot aim to evidence, together with the fast perturbation previously discussed, also a long lasting small positive shift of the phonon frequency. The integrated intensity of the Raman lines is shown in black curve and the temperature variation calculated from this is depicted in red. The temperature variation in time was derived comparing the intensity of the Raman line at a certain time to an average of the negative time intensity, making use of the statistics described in the introduction[1]. The energy per pulse is of the order of 0.13nJ. The excited volume, calculated using an absorption coefficient of 500 cm^{-1} and a spot size of $\approx 5\mu m^2$, is $\approx 2\mu m^3$. The silicon heat capacity of 20J/mol K and an excited volume of $\approx 10\mu\ m^3$ it's possible to estimate the expected temperature changes due to the laser pump in about 70K. The observed temperature raise is substantially smaller than the expected one ($\simeq 20\%$ of it). This is consistent with the proposed picture that the recombination processes of excited carriers in the X valley are of the Auger Kind. They don't result in effective lattice heating. The CW Raman experiments in temperature show that the phonon frequency shift at a rate of $\frac{d\nu}{dt} \approx 0.03 cm^{-1}/^{\circ}K$.

[1]The statistical analysis is based on the assumption of a constant Raman tensor in time

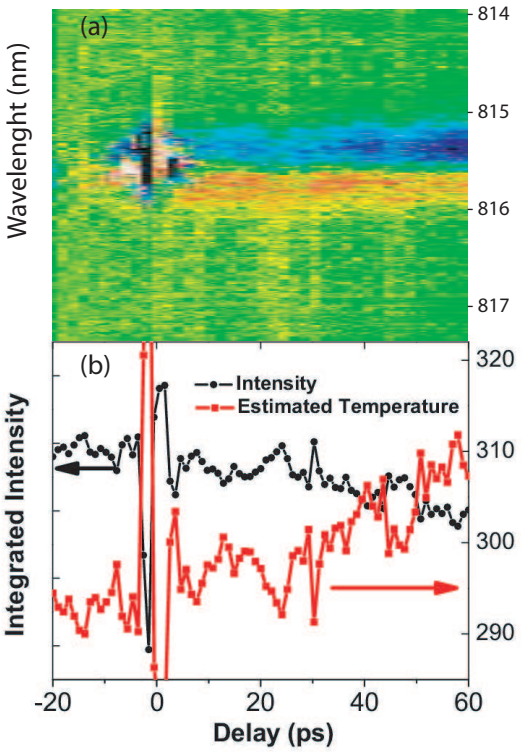

Figure 4.8: *(b)Integrated intensity of the time-dependent Raman traces for the stokes line(black dots), and temperature variation estimated (red dots)- See text for discussion. (a) The difference between the stokes line and the average of stokes line at negative frequency is reported to evidence the frequency shift following the irradiation.*

As shown in Fig. 4.8 (a), the observed shift is consistent with this value. The analysis of the frequency shift measured (the first momentum of the excitation) are between 0,3-0,5cm^{-1}, in agreement with the shift expected for the temperature variation estimated from the statistic[2].

To summarize, making use of time resolved Raman spectroscopy we were able to study the relaxation processes in silicon in the ps range. We could follow in real time the lattice temperature, measured through the Raman scattering statistic

[2]The laser pulsewidth is of 15 cm^{-1}, substantially larger than the fitted shift. Nevertheless the qualitative agreement between the frequency shift calculated from estimated temperature changes and the real temperature shift is a good indication of being in a state in thermal equilibrium.

and qualitatively confirmed by the frequency shift observed. We showed that in the ultrafast relaxation processes (following the irradiation with a light pulse of 15mJ/cm^2) the temperature of the Silicon lattice increase only $\simeq$20% of the expected value. This support the picture of the absorption being dominated by phonon assisted processes, where the carriers are excited in the X-valley of the conduction band, and thermalize into a non-luminescent long-living state. On the time scale investigated, no contribution to the lattice heating ascribed to these carriers is observed.

4.3 Conclusion

In summary, the characteristics of the continuous wave Raman setup are reviewed in the first part of the chapter, and the two different approaches to achieve a dynamical version of it are described. i) The setup for measuring the Raman response on the μsec time scale is based on an amplified Ti:Sapphire laser with 1kHz repetition rate, used as pump, coupled with a CW laser, used as probe. Through a custom made mechanic chopper synchronized to the trigger of the Ti:Sapphire, the CW laser is sliced into 10μsec pulses at 1kHz repetition rate. The time delay between the pump and the probe is controlled electronically through the phase of the chopper synchronization. ii) The setup for measuring the ultrafast Raman response on on the ps time scale is based on a ps laser (mira 900) followed by a geometrical filter allowing us to clean the laser beam from the background luminescence. The dynamical response is achieved introducing a mechanical delay between pump and probe, and a polarization control in front of the detection system allowed us to distinguish between the signal coming from photons scattered from the pump from those scattered from the probe.

Bibliography

[1] D. E. Spence, P. N. Kean, and W. Sibbett, Opt. Lett. **16**, 42-44 (1991).

[2] E. Beaurepaire, J.-C. Merle, A. Daunois, and J.-Y. Bigot, Phys. Rev. Lett. **76**, 4250 (1996).

[3] S. I. Kudryashov,and V. I. Emelyanov, JETP Letters **73 N5**, 228-231 (2001).

[4] H. W. K. Tom, G. D. Aumiller,and C. H. Brito-Cruz, Phys. Rev. Lett. **60**, 1438 (1988).

[5] S. L. Johnson, P. A. Heimann, A. M. Lindenberg, H. O. Jeschke, M. E. Garcia, Z. Chang, R. W. Lee, J. J. Rehr,and R.W. Falcone, Phys. Rev. Lett. **91**, 157403-1 (2003).

[6] F. Banfi, C. Giannetti, G. Ferrini, G. Galimberti, S. Pagliara, D. Fausti,and F. Parmigiani, Phys. Rev. Lett. **94**, 37601 (2005).

[7] M. Hase, M. Kitajima, A. C. Constantinescu,and H. Petek, Nature **51**, 426 (2003).

[8] A. Cavalleri, Th. Dekorsy, H. H. W. Chong, J. C. Kieffer,and R. W. Schoenlein, Phys. Rev. B **70**, 161102 (2004).

[9] H. Ihee, M. Lorenc, T. K. Kim, Q. Y. Kong, M. Cammarata, J. H. Lee, S. Bratos,and M. Wulff, Science **309**, 1223 (2005).

[10] K. Sokolowski-Tinten, D. von der Linde, J. Phys.: Condens. Matter **16**, R1517R1536 (2004).

[11] D. Fishmann, P. H. M. van Loosdrecht, In progess., (2008).

[12] P. Stempfli, K. H. Bennemann, Phys. Rev. B **49**, 7299-7305 (1993).

[13] D. M Fritz,and D. A. Reis, B. Adams, Science **315**, 633 (2007).

[14] D. von der Linde,and J. Kuhl, H. Klingenberg, Phys. Rev. Lett., 1505 (180).

[15] J. A. Kash,and J. C. Tsang, J. M. Hvam, Phys. Rev. Lett.**54**, 1151 (1985).

[16] P. Baum,and D. S. Yang, A. H. Zewail, Science**318**, 788 (2007).

[17] T. Sjodin,and H. Petek, H. L. Dai, Phys. Rev. Lett.**81**, 5664 (1998).

[18] A.J. Sabbah,and D.M. Riffe, Phys. Rev. B**66**, 165217 (2002).

[19] A. J. Riffe Sabbah,and D.M. Riffe, J. Appl. Physics**88**, 6954 (2000).

[20] Coherent Inc., *Operator's Manual The Coherent Mira Model 900-P Laser* .

Chapter 5

Bismuth and Antimony: Toward the Simple Cubic Phase?

5.1 Introduction

Nearly all of the elemental metals crystallize into a cubic (FCC, BCC) or hexagonal closed packed (HCP) structure. An exception to this is found in the elemental crystals of Bismuth, Antimony and Arsenic, which crystallize into the α-Arsenic structure (A7) with rhombohedral space group R$\bar{3}m$. The structure of the A7 compounds is shown in Fig.5.1 (a). It can be described as a distorted simple cubic structure, where the (111) planes of atoms have an alternating displacement along the [111] direction. The structural anomaly of the semimetals Bi, Sb, and As has been widely discussed in the past[16, 7], and is found to originate from a strong electron phonon coupling. In one dimension, this type of distortion is the well known Peierls distortion[1]. The ideas leading to the formulation of the theory for the Peierls distortion actually originate from the structure of the A7 compounds and was initially dubbed the Jones-Peierls mechanism[1]. The mechanism is based on the observation that the distortion leads to the presence of two non-symmetry-related sites for the atoms within the unit cell. This, as argued by Harry Jones, introduces a small band-gap in the electronic structure over extended regions of the Brillouin zone which stabilizes the structure: The elastic energy cost for the deformation is compensated by the electronic energy gain due to the opening of the gap (see Fig.5.2 (a)). The presence of the small gap in extended regions of the Brillouin zone is also responsible for the semimetallic behavior of the A7 elemental compounds.[20, 1] For a more detailed explanation see the appendix at the end of this chapter.

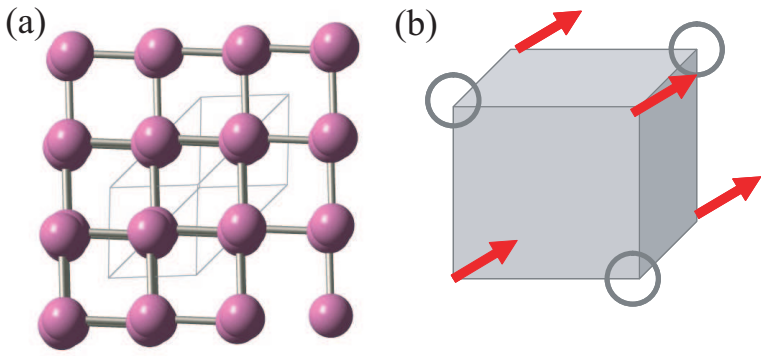

Figure 5.1: *(a)Sketch of the A7 crystal structure. The rhombohedral unit cell is indicated by the thin lines. (b) The $R\bar{3}m$ structure viewed as a deformation of the simple cubic space group.*

From a Raman scattering point of view, the A7 metals are of particular interest. The Peierls distortion from the cubic phase has the same displacement pattern as the Raman active A_g phonon mode in the A7 structure in which the atoms vibrate along the distortion direction (see Fig. 5.4). Intuitively, one immediately understands that this phonon and the Peierls gap are intimately related. In fact, this A_g mode would be the 'hard' mode of a hypothetical phase transition from the cubic phase to the A7 structure. Hypothetical, because none of the A7 compounds actually shows this transition, since the transition temperature is higher than the melting temperature of the compounds. With increasing pressure both Bi and Sb approach the primitive simple cubic phase, but no undistorted simple cubic phase has been reported at the thermodynamical equilibrium.[19] The A_7 metals thus provide a beautiful playground for studying the intricate interplay between electronic and vibrational degrees of freedom in the Peierls physics. This is particularly true for experiments addressing both electronic and vibrational excitations. Indeed, both Bi and Sb have served as archetypical cases in studies of coherent excitations in absorbing materials. The main observation in transient optical pump-probe reflectivity experiments has been that these materials show a fast reflectivity response which is strongly modulated by a coherent 3.1 THz excitation. The frequency of the intense coherent response is close to the A_g phonon frequency, and has therefore been assigned to coherent excitation of this particular phonon mode.[5, 12] The frequency of the coherent oscillation is, however, not constant in time; it increases upon increasing pump-probe delay. In high pump power experiments[10] it was found that the initial frequency of the oscillation is about 2.5 THz, which, upon increasing pump-probe delay, slowly ($\simeq$5ps) approaches the value 3.1 THz which is the frequency observed in continuous wave Raman exper-

iments (see section 5.3.1). This effect was originally ascribed to the non-linearity (anharmonicity) of the crystal potential. Generating coherent phonon excitations using an intense pump pulse leads to a large collective atomic displacement. This should allow for the "exploration" of the static crystal potential far from the equilibrium position: The further the atoms are from the equilibrium positions, the more the anharmonic terms of the crystal potential will influence their motion. It has been argued that this induces the observed softening of the oscillation frequency at early times, as well as the increase of the frequency as the amplitude of the coherent motions decreases due to relaxation and dephasing processes.[10] Later, an alternative, more intriguing, explanation for the phonon softening was suggested based on electronic screening of the crystal potential[11]. This second scenario rekindled the hope of accessing a number of intriguing non-equilibrium phenomena arising from the impact of a high-density electron population of the conduction band on the crystal structure. Time resolved x-ray diffraction suggested that intense irradiation could lead to non thermal melting phenomena, due to the electron-phonon interaction induced flattening of the crystal potential after the pump irradiation[20]. More recently the melting scenario was falsified by the suggestion coming from density functional theory calculations, supported by new x-ray diffraction experiments, that a high enough light induced population of the conduction band should lead to a phase transition from the A7 structure toward a more symmetrical cubic symmetry[2]. The suggested mechanism is sketched in Fig.5.2(b): The optically induced population of the conduction band makes the mechanism stabilizing the Peierls distorted structure less effective. When the population of the conduction band increases, the electronic energy gain obtained from distorting the structure reduces until eventually (for a population around 2,7%) the A7 structure is no longer stable, and the crystal undergoes a transition into the undistorted cubic phase.

In spite of the effort devoted so far to distinguish between the two scenarios outlined above, both from the experimental and theoretical side, no consensus has been reached so far. A clear experimental distinction between the two proposed scenarios could come from the actual observation of an induced cubic phase, but unfortunately this has not been observed to date. A second experimental approach is to use an experiment which does not require a coherent lattice excitation to detect the changes in the materials due photo-excitation into the conduction band. This approach is pursued in the current chapter which presents results of a ultrafast time resolved Raman spectroscopy study of Bismuth and Antimony single crystals. This technique is sensitive to transient changes in the crystal structure through transient changes in the spontaneous vibrational Raman response. Two distinct dynamics will be unraveled: A fast non-thermal one occurring in the first few picoseconds after irradiation, and a slower thermal one which lasts for more than 100ps. In addition to this, a simple phenomenological model, based on a

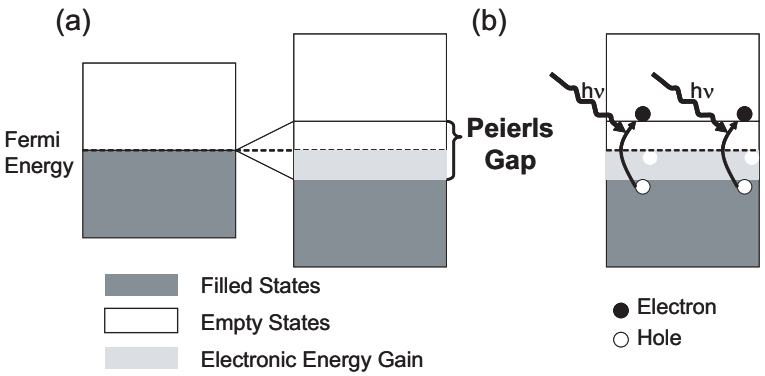

Figure 5.2: *(a) Schematic view of the Peierls distortion mechanism. Opening a gap at the Fermi level leads to electronic energy gain proportional to the light grey area. This electronic energy gain compensates the elastic energy "paid" to create the lattice distortion. (b) Sketch of the suggested mechanism for the optically induced destabilization of the A7 structure. The light induced population of the conduction band reduces the electronic energy gain leading to a reduction of the lattice distortion.*

Landau expansion of the free energy, will be presented which is capable of describing both the phonon softening as well as the eventual collapse of the Peierls state upon photo-excitation. Finally, at the end of this chapter some experiments using excitation powers close to the damage threshold will be discussed, which seem to show a periodic phase transition from the Peierls state to presumably a disordered phase.

5.2 Theoretical considerations

As discussed in the previous section, electronic population of the conduction band leads to a destabilization of the Jones-Peierls phase. The DFT calculations by Fritz *et al.* [3] nicely exemplified this in a quantitative manner. Here, a more simple, phenomenological approach is followed to give a quantitative description of the phonon softening as a function of the dynamical electronic population $n(t)$ of the conduction band, following the approach suggested by Zeiger *et al.*[4]. Starting from a hypothetical high symmetry cubic structure, the A7 structure arises from a structural phase transition with the amplitude of the displacement of the atoms along the cube's body diagonal, q, (see Fig. 5.1 (b)) as the order parameter. This corresponds to the atomic displacement associated to the Raman active A_{1g} phonon. In terms of this order parameter, a Landau expansion of the free energy $E(q)$ may be written as:

$$E(q) = -an_0q^2 + bn_0q^4 + \dots \tag{5.1}$$

Where n_0 is the number of unit cell for unit volume. Note that in this expression the temperature dependence of the coefficients in the expansion is not included explicitly, since this is less relevant for the present discussion. It will be assumed that there is a non-zero order parameter, hence that the system is in the distorted A7 phase. The equilibrium position in the distorted phase is obtained by minimizing the free energy with respect to q, and is given by $q_0 = \sqrt{\frac{a}{2b}}$. From the equation of motion $\mu n_0 \ddot{q} = -\frac{dE}{dq}$, where μ is the reduced mass of the vibration ($\mu = \frac{1}{2}m_X$, X=Bi,Sb,..) one easily finds the vibrational frequency of the order parameter excitation (the A_{1g} Raman mode) to be $\omega_0 = \sqrt{\frac{4a}{\mu}}$.

Optically induced excitation of n electrons over the Peierls gap results in two additional contributions to the free energy:

i) A term proportional to the number of excited carriers n to account for the electronic energy. This term can be taken as $\propto \Delta n$, where Δ is the Peierls gap.

ii) A term accounting for the electron-phonon coupling, *i.e.* to the amplitude of the lattice distortion through the excited electronic population. This term may be written as cq^2n.

Inclusion of these terms in the Landau expansion gives:

$$E(q) = -an_0q^2 + bn_0q^4 + (\Delta + cq^2)n(t). \tag{5.2}$$

Obviously, there is now an additional *positive* quadratic term in the expansion, which will change both the equilibrium structure, as well as the frequency of the order parameter oscillations. When the product $cn(t)$ is large enough, the equilibrium structure will actually be the cubic phase, rather than the A7 structure. Thus, the population of the conduction band could cause the Peierls gap to collapse, provided that the density of excited charges is high enough. The shape of the free energy Eq.5.2 is depicted in Fig.5.3 as a function of the displacement q and excited electron density n. The equilibrium position and the frequency of the vibrational mode as a function of the electron population are easily calculated. The new equilibrium position follows from $\frac{dE(q)}{dq} = -2an_0q + 4bn_0q^3 + 2cqn = 0$ to be

$$q_n = \sqrt{\frac{a}{2b} - \frac{cn}{2n_0b}} = \sqrt{q_0^2 - \frac{c}{2n_0b}n}. \tag{5.3}$$

As expected, the equilibrium[2] distortion depends on the number of electrons excited in the conduction band. In the limit of small $n << \frac{2n_0bq_0^2}{c}$, q_n depends linearly on n:

$$q(n) = q_0 - \frac{c}{n_0bq_0^2}n. \tag{5.4}$$

[2]The term equilibrium here does not refer to a truly thermodynamic equilibrium, but rather to the transient "equilibrium" structure as a function of the conduction band electron density $n(t)$.

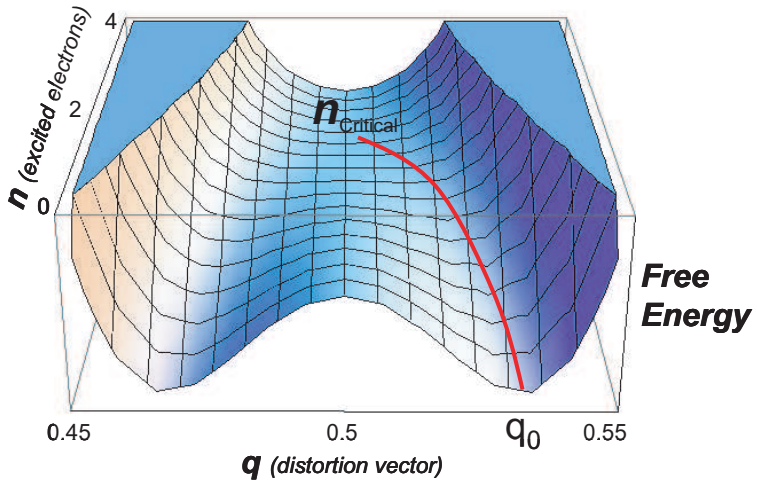

Figure 5.3: *Two dimensional potential landscape as a function of the distortion q, and the density of electrons in the conduction band. The red line shows the equilibrium position as a function of the conduction band electron density.*

The phonon frequency (in the harmonic approximation) will also depend on the number of electrons as (see Appendix for a detailed calculation):

$$\omega_n = \sqrt{\omega_0^2 - 4c\frac{n}{n_0}} \tag{5.5}$$

Again, in the low density limit ($n << \frac{n_0\omega_0^2}{4c}$) the phonon frequency depends linearly on the number of excited electrons:

$$\omega(n)_{n<<1} = \omega_0 - \frac{8c}{n_0\omega_0^2}n, \tag{5.6}$$

in agreement with earlier results.[3]

5.3 Results and Discussion

5.3.1 Conventional Raman experiments

The full representation of the vibrational modes of A7 structure is:

$$\Gamma_{tot} = A_{1g} + A_{1u} + E_g + E_u \tag{5.7}$$

where the A_{1g} and E_g modes are Raman active and the A_{1u} and E_u are acoustic modes. The Raman tensor for the A_{1g} mode has only diagonal components and is expected to be active in a parallel configuration only. In contrast, the E_g tensor

has both diagonal and off diagonal components, making modes with this symmetry active in both parallel and crossed polarizations. Fig. 5.4 shows polarized room temperature Raman spectra measured in the $a(cc)a$ and $a(cb)a$ polarization[1]. for an Antimony and a Bismuth single crystal. For Bismuth, the selection rules are fully respected: the A_{1g} mode appears only in the parallel configuration, while the E_g is active in both (black curve in Fig.5.4). In case of Sb the A_g mode, even though less intense, appears also in the cross polarization measurement. This could be due to the presence of some local surface or bulk disorder in the Antimony crystals.

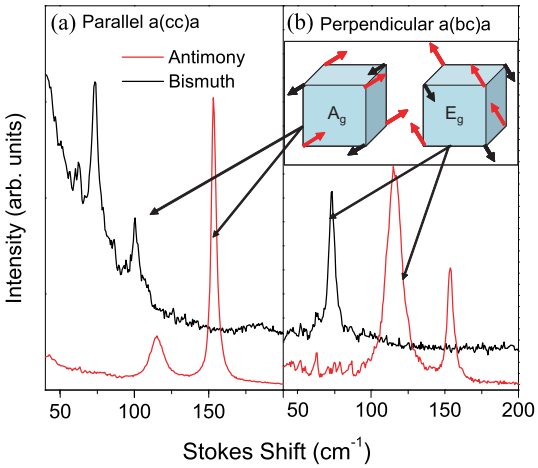

Figure 5.4: *Polarized Raman spectra of Bismuth and Sb single crystals in a parallel (a) and a perpendicular (b) polarization at room temperature. The inset displays a sketch of the atomic motions of the A_g and E_g Raman active modes.*

The atomic displacements associated to the Raman active modes are depicted in the inset of Fig.5.4. The A_{1g} phonon corresponds to a displacement of the nuclei along the body diagonal of the "cubic" structure, giving rise to a sort of breathing mode of the (111) planes. This is the order parameter oscillation discussed in the previous section. In contrast, the E_g mode corresponds to a shear vibration of the planes with respect to each other. Even though both modes will be coupled to the electronic degrees of freedom, it seems, in view of the A7 distortion, natural to expect that the A_{1g} mode will be more strongly coupled to the electronic structure, or, in other terms, that the population of this mode will strongly affect

[1]We use the Porto notation throughout, where the polarization and geometry of the experiment is given relative to the crystal axis. The first and last letter indicate the direction of the k-vector of the incoming and scattered light, respectively, while polarization of these is indicated by the symbols within the brackets

the electronic properties of the crystal. Vice versa, one expects that excitation of a high density of carriers into the conduction band will lead to a perturbation to this mode as discussed in the previous section. On the contrary, for the E_g mode, that does not change the distance between the planes, the coupling to the electronic degrees of freedom is expected to be much weaker.

5.3.2 Initial Results on Bismuth and Antimony

The measurement in real time of the Raman response, in a all optical pump and probe experiment, would shed some light on the lattice behavior in the early time (¡10ps) after laser irradiation in adsorbing materials. The potential landscape with a high density of excited electron will be mapped making use of this powerful technique. Thus the following part of this contribution is going to be centered on first dynamical measurements of the spontaneous Raman response in A7 compounds. Fig.5.5 (a) shows the measurements of the dynamical Raman Raman response for different pump intensity. The measurements were performed in a triple grating monochromator (T64000, Jobin Yvon). The excitation laser was a 80MHz Ti:sapphire laser (Mira 900) lasing in the ps regime. The laser light were filtered with a custom designed optical scheme (for a detailed description see Chapter 4). Making use of a beam splitter the beam is divided into two, one more intense (pump) and a second weaker (probe). The delay between the pump and the probe is controlled through a remote controlled delay line. The pump and the probe beams are recombined with a second beam splitter and coupled into the Raman microscope in a collinear configuration. The scattered light is collected in a back scattering configuration and coupled into the Raman monocromator. A second polarizer, allowing through only the probe polarization, is placed in front of the spectrometer. The fact that the A_g Raman tensor has only diagonal elements allow the polarization selection of the light scattered from the pump and the probe. Fig.5.5(a) clearly shows that the A_g mode shift at lower frequency upon laser irradiation. To quantify the dynamical shift of the mode, the first moment of the excitation is plotted in Fig.5.5(c). The first moment is defined as $\sum \nu I(\nu)$ and give a value of the average frequency of the mode. It appear clear that the mode frequency shift to lower frequency immediately after the pump irradiation.

The higher the pump intensity the larger is the shift observed. In the high fluency limit two different dynamics become visible. Pointing to Fig.5.5(c), the trace relative to a pump intensity of 17mJ/cm^2 shows that after the first 10ps the central frequency of the mode relaxes back, bit it doesn't reach the equilibrium position. It reach a frequency lower than the equilibrium one and stays there for all the time time window investigated. Fig.5.5(b) shows the transient reflectivity traces measured in the same excitation density region. All the reflectivity traces reported are also characterized by two main characteristic dynamics. The fast increase of

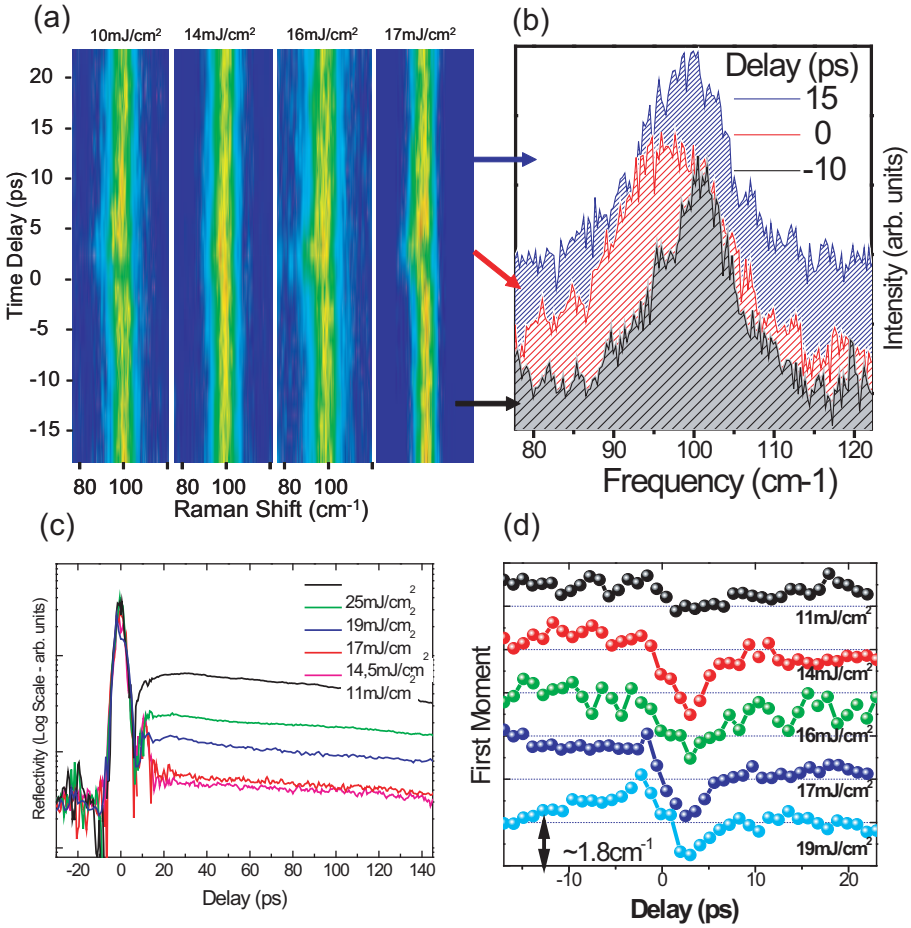

Figure 5.5: *(a) False color plot of the Pump and probe Raman measurement of the Bismuth A_g mode at different excitation intensity. (b) Typical spectra at different time delays (-10, 0 and 15ps). (c) Transient reflectivity measurements at 780nm. (d) First moment of the Raman of the spectra features in (a). The data are reported with an offset for clarity.*

the reflectivity lasts for a time comparable to the autocorrelation between the two pulses and subsequently the reflectivity display a minimum followed by a slow raise lasting for the all time interval measured.

The poor quality of the transient Raman response were due to the small cross section of the A_g phonon in Bismuth. Moreover the relatively low melting temperature and heat conductivity of Bismuth didn't allow to explore the high intensity dynamics. Piling up effects due to the high repetition rate of the laser didn't

allow to explore entirely the non equilibrium dynamics. For all this reasons the focus of our research has been moved to the Bismuth "twin brother" crystal, Antimony. As sketched in the introduction, the physical processes underling the semimetallic behavior of Antimony are similar to the one of Bismuth. Nevertheless a few differences in the thermodynamical properties make Sb more suitable for the experiments, Table 5.1 summarizes them. The melting threshold of Sb single crystal and the heat conductance are higher than in Bi, indicating that the non-equilibrium region accessible before piling up effects between successive pulses is expected to be larger. In addition to that the A_g mode of Sb single crystals is at slightly higher frequency and has a larger Raman cross section, making the experiments easier and less time demanding.

Table 5.1: *Comparison between some of the physical properties of Bismuth and Antimony.*

Property	Bismuth	Antimony
Heat capacity	25,52J/mol K	25,23J/mol K
Heat conductance	7,93W/m K	24,4W/m K
Melting temperature	544.4 K	903.78

Fig.5.6 reports the transient Raman response for excitation intensity between 2,7 and 8,4mJ/cm^2. The dynamics observed are similar to those reported in Bismuth. The two distinct dynamics observed in Bi emerge clearer from the Sb measurements. An ultrafast softening of the A_g mode is followed by a slow relaxation lasting for all the time window explored. In order to make these two distinct dynamics more evident in Fig.5.6(b) the same measurements are plotted subtracted of an average of the spectra at a negative time delay.

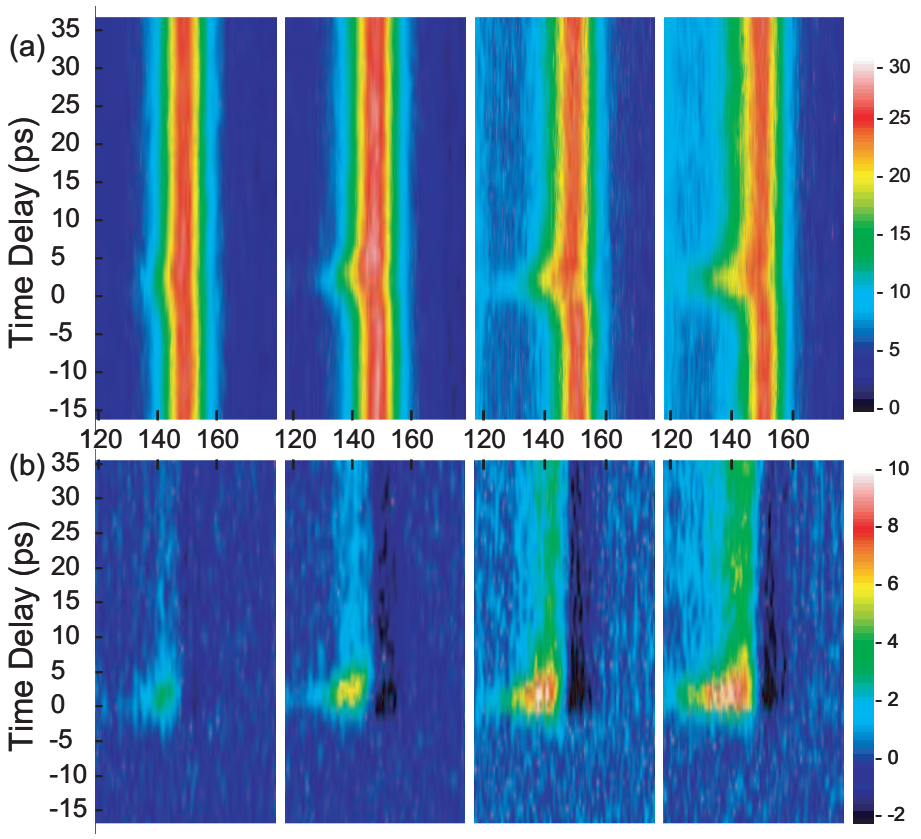

Figure 5.6: *(a)False color plot of the Pump & probe Raman measurements on the A_g mode of Antimony for different pump intensity.(b) False color plot of the Raman spectra for different pump intensities. An average of the negative spectra has been subtracted to make more evident two different dynamics observed on the phonon frequency. The intensity color scale of the two low power measurements is 10 times larger than the high energy ones (blue negative - red positive).*

5.3.3 Detailed analysis on Antimony

Increasing the pump intensity the phonon softening in the fast time scale in the first 5/8ps after pump irradiation increases. The same measurements are plotted in Fig.5.8 with the aim of evidencing the differences between the phonon shape for different pump excitation density. When the probe pulse arrive on the sample 15ps before the pump one (Fig.5.8(c)), as expected, no perturbation of the phonon mode is observed at the power investigated. This clearly indicate that the overall heating effects of the pump are small and that in 12ns (the repetition rate of our laser), the heating effects are diffused away from the laser spot. Only the high excitation density spectra (Fig.5.8(c) - blue curve) shows that at the negative time delay the phonon mode displays a small frequency shift ($<<1\text{cm}^{-1}$) due to the average heating effects. On the other end, the transient effects result clearly visible on the positive time delay for all the time window investigated. Fig.5.8(a) reveals that increasing the pump power the A_g phonon mode 25ps after the pump irradiation shift to lower frequency.

To quantify these two dynamics the first moment of the spectra are plotted in Fig.5.7. The pump perturbation induces a frequency shift within the first few ps of the phonon mode proportional to the Pump intensity. Fig.5.7(b) depict the frequency shift related to the two dynamics.

Let us first discuss the average shift at the positive delay (25ps). The temperature dependence of the Raman spectra showed that the frequency of both the A_{1g} and E_g modes decrease linearly increasing the temperature[18]. The magnitude of this frequency softening was explained through the thermal expansion that would lead to a phonon softening. On the other hand to explain the strong line-width increase with temperature an additional broadening arising from electron-phonon coupling was necessary. In absolute value the E_g mode was found to be broader than the A_{1g} one at all temperature for both the compounds. The comparison between the line-width at finite and "zero" temperature Γ_T/Γ_{4K} shows that the relative increase is larger for the A_{1g} mode. In the analysis proposed the broadening was ascribed to the electron-phonon coupling considered to be a temperature independent constant. A recent optical study[21] demonstrates through the observation of the lowering of the plasmon frequency in temperature that the charge transfer from electron to hole pocket is significant. As shown in Fig.5.7(b), the shift of the phonon frequency at a positive time is found to depend linearly on the pump intensity (red stars). This evidence, together with the slow relaxation observed lead to the interpretation of the "25ps" phonon shift in terms of a thermally induced shift of the phonon frequency. The higher is the energy released into the system from the pump pulse, the higher is the local temperature expected, and therefore the largest is the phonon shift expected. The relaxation time of this slow dynamic will be dominated by the heat diffusion, too slow for being observed in the time-window explored. An estimation of the temperature raise induced by the

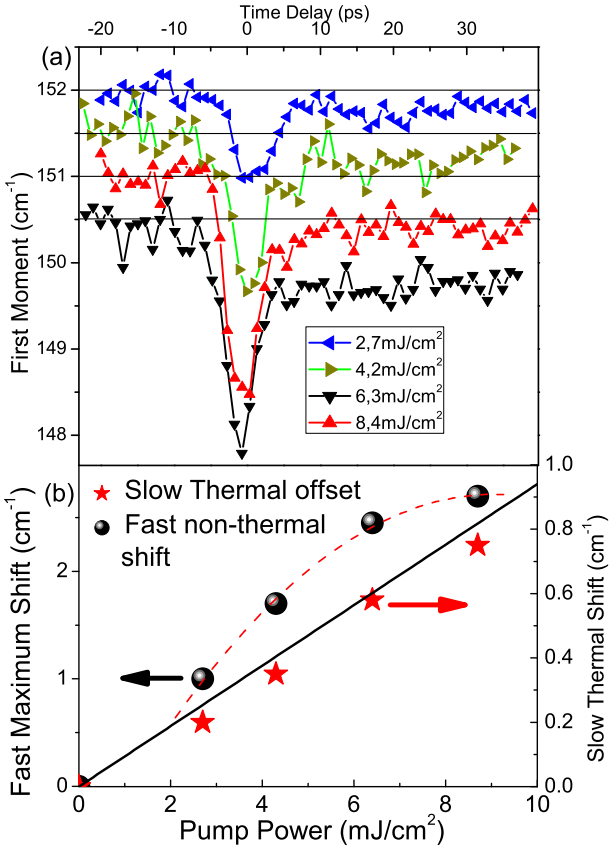

Figure 5.7: *(a) Time dependence of the first moment A_g Raman mode for Sb single crystal. The different pump intensity are plotted with an offset for clarity.(b) The maximum ultrafast non thermal shift (balls) is plotted versus the pump intensity. The dashed line (red in the color version) is the result of a fit to the data with a quadratic function. The average of the thermal shifts at positive times (between 15 and 35 ps) is plotted vs the pump intensity (stars). The thick line (black in the color version) is the result of the calculated shift of the Raman line due to the temperature raise induced by the pump energy (see text).*

pump pulse in the Sb is given by $\frac{dT}{dE_{pump}} \approx 8\frac{Kcm^2}{mJ}$. The temperature dependence of the Raman mode is $\frac{d\nu}{dT} \approx 0.012\frac{cm^{-1}}{K}$. The two equation together results in an

shift dependence on the excitation power of:

$$\frac{d\nu}{dE} = \frac{d\nu}{dT}\frac{dT}{d\nu} = 0,096\frac{cm^{-1}}{mJ/cm^2} \tag{5.8}$$

The calculated dependence is plotted in Fig.5.7(b) (black line). The good agreement between the observed experimental shift and the calculated one confirms the interpretation of the slow dynamics as a thermal shift due to the heat induced by the pump excitation.

On the contrary, the ultrafast dynamic observed in the first 10ps after pump irradiation cannot be ascribed to a temperature changes into the sample. The thermodynamical constants of Sb clearly show that the temperature required for such a phonon softening are not reachable with the excitation density used. To give a deeper insight into this ultrafast response revealed by the first momenta of the Raman spectra a detailed analysis of the lineshape of the excitation has been performed.

Time-dependent lineshape of the A_{1g} optical phonon

Damaging threshold To gain a deeper understanding on the optically induced phase transition in Bismuth and Antimony, we measured the Raman spectra for pump and probe overlapped in time and space. The results are reported in Fig.5.9 (a). The measurements of the damaging threshold was carried on alternating the pump & probe measurements with an unperturbed measurement. For pump intensity up to 12,5mJ/cm^2 no permanent damage was observed in the Raman feature. Above this threshold an irreversible changing in the sample was observed. It should be mentioned that the damage produced is not visible under an optical microscope, but it appears in the Raman measurements as an increase in the Raman cross section (+50%) for the A_g mode. This suggest that the damage optically induced in this regime could be a order-disorder transition.

Lineshape Before discussing the dynamical phonon response let us look back at Fig.5.8(b) and consider the power dependence of the phonon lineshape for pump and probe overlapped in time. Even below the damaging threshold (I<12mJ/cm^2) in the first few picoseconds after pump irradiation a dramatic changes occurs in the phonon lineshape and its central frequency. Fig.5.10 depict the lineshape of the Raman response for pump and probe overlapped in time and space. At low excitation densities the A_{1g} phonon mode can be nicely fitted with a single Lorentian distribution at all time delay. On the contrary, at high excitation density the response results to have no longer the simple Lorentian lineshape. As depicted in the left panel of Fig.5.10 an additional component at low energy

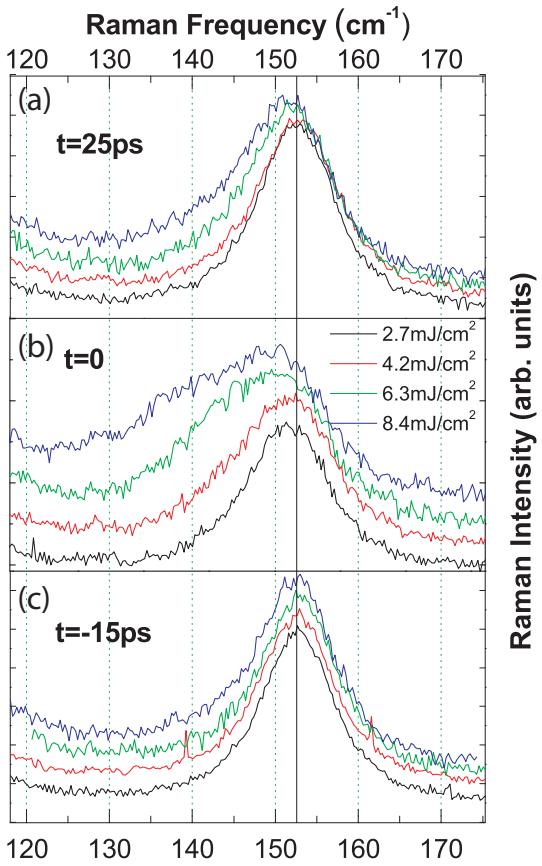

Figure 5.8: *Phonon line shape for different pump intensity for positive (a), zero (b), and negative time delay (c).*

(L2) become visible. This indicated that, even below the damaging threshold two excitation regimes can be distinguished. The first one, for low excitation density (I¡5mjcm^2), where the Raman response can be described simply by a shift of the A_{1g}, and the second one for intermediate excitation density (5¡I¡12mJ/cm^2) where a simple phonon shift no longer reproduce the Raman results. For excitation density of 8,4mJ/cm^2, a fit of the Raman response at different time allowing the central frequency, width, and intensity of both L1 and L2 to vary revealed that the central frequency and width of L2 would vary in time of less than 10% around the central frequency of 138cm^{-1}. For this reason we propose that the additional component is at a fixed frequency in time.

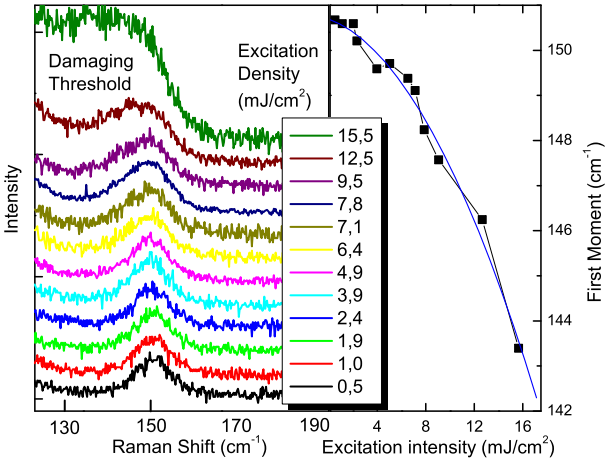

Figure 5.9: *(a)Pump power dependence of the Raman at zero delay between the pump and the probe. (b) The first momentum for the spectra at different intensity is plotted. The spectra continuously shift toward lower frequency. The damaging threshold is found to be above 12.5mJ/cm^2.*

Figure 5.11 showed the fit parameter obtained with a fixed L2 central frequency (138cm^{-1}) and width (8cm^{-1}) and a free L1 (width, intensity and central frequency). Fig.5.11(b) showed the central frequency obtained for the the A_{1g} (L1) phonon. The two dynamics discussed, in the previous section, making use of the first moment of the spectra are confirmed. The A_{1g} phonon (L1) undergo an ultrafast non-thermal softening followed by the relaxation into a thermal state lasting for all the time-window investigated. The thermal softening is confirmed to be linear with the pump power, while the non thermal dynamic confirmed the previously discussed sub-linear behavior. Fig.5.11 (a) depict the time dependent intensity of the L2 Lorentian features for different pump excitation density. It is revealed that L2 gives a contribution to the Raman mode only above the threshold of $\simeq$5mJ/cm^2, while it is not present in the low excitation density limit.

As anticipated in the introduction the phase diagram of Antimony single crystals under pressure is quite complicated and still debated. Increasing the pressure the structure approaches closely at 7GPa the simple cubic phase. The Raman response in this low pressure regime revealed a continuous softening of the A_{1g} phonon mode from the 153cm^{-1} at ambient pressure to $\simeq$130cm^{-1} at 7GPa. Between 7 and 9GPa the Raman measurements revealed the appearance

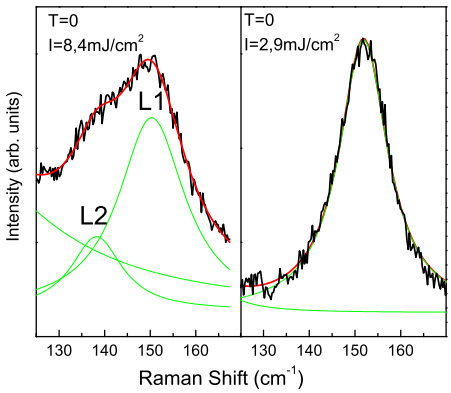

Figure 5.10: *Phonon lineshape in the first picoseconds after pump irradiation (t=0). In the right panel the experimental lineshape measured in the low excitation density limit (2,9mJ/cm^2) is depicted. The fit is obtained with two lorentian distribution (one for the phonon response and the second, centered at low frequency, to account for the background). The left panel show the experimental phonon response in the high excitation density limit (8,4mJ/cm^2). The spectra are no longer reproduced by two lorentian distribution but a third is needed (L2).*

of additional lines corresponding to the incommensurate monoclinic host-guest Sb-IV structure[22]. This suggest the coexistence between the Sb-I and Sb-IV phases.[22] Above 9GPa the tetragonal host-guest incommensurate phase SII become stable.[23] This phase is revealed in Raman spectroscopy by the presence of a band composed of 5 additional modes between 80 and 170cm^{-1}.

In view of the Peierls physics described in section 5.2, in the low excitation density limit the optical population of the conduction band "acts as applying pressure". i.e. The Peierls physics consists of the electronic energy gain compensating the lattice energy loss in the distortion ($E_{tot} = E_{lattice} - E_{electrons}$). In this sense applying pressure will make the lattice stiffer and will increase the cost of the distortion. From the Peierls point of view this will result in the same effects as reducing the electronic energy gain through the population of the conduction band. Clearly the simple physics described in section 5.2 can't account for all the phases revealed, different structural dynamics not included in the simple model described makes the cubic phase unreachable. Nevertheless, the phase diagram reach of host-guest structure (both Sb-II and Sb-IV are host-guest phases) suggests that localization phenomena and phase coexistence in Antimony single crystal can be energetically favored. In view of this, the coexistence of two different phonon frequency is ascribed to a local collapse of the Peierls gap. In the low intensity limit the population of the conduction band would cause a "delocalized"

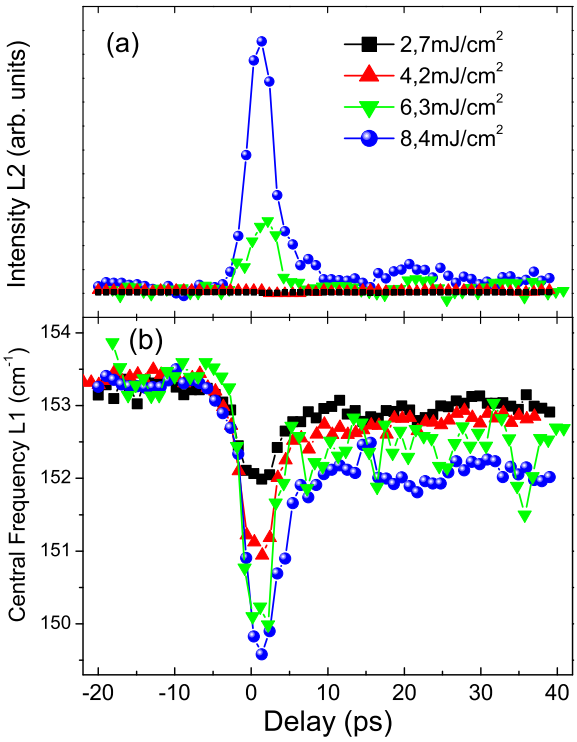

Figure 5.11: *(a) Time dependence of the intensity of the L2 peak for different pump intensity. A threshold behavior is revealed, the L2 appear only above 5mJ/cm^2. (b) Time traces of the central frequency of the L1 mode.*

Peierls band collapse. Increasing the electron density could cause a local collapse of the Peierls gap limiting the electronic delocalization. This would explain the coexistence of the two phonon modes observed in the ultrafast Raman response. Further theoretical investigation would be needed to confirm the "physical feasibility" of this new intriguing state.

High excitation density Fig. 5.12(a) reports the transient Raman response for a measurements just below the damaging threshold (11mJ/cm^2). An anomalous modulation of the Raman response is revealed and made more evident by the plot in Fig.5.12(c), where an average of the negative spectra have been subtracted from the response in (a). It should be mentioned that after the measurements the sample resulted damaged in the sense defined earlier: no damage was visible

in an optical microscope, but enhanced Raman activity of the A_g mode revealed a permanent modification of the crystal structure. Fig.5.12(b) shows the Raman response at different times after the pump irradiation. The measurement at a different times are reported to make clear the spectral features at different times.

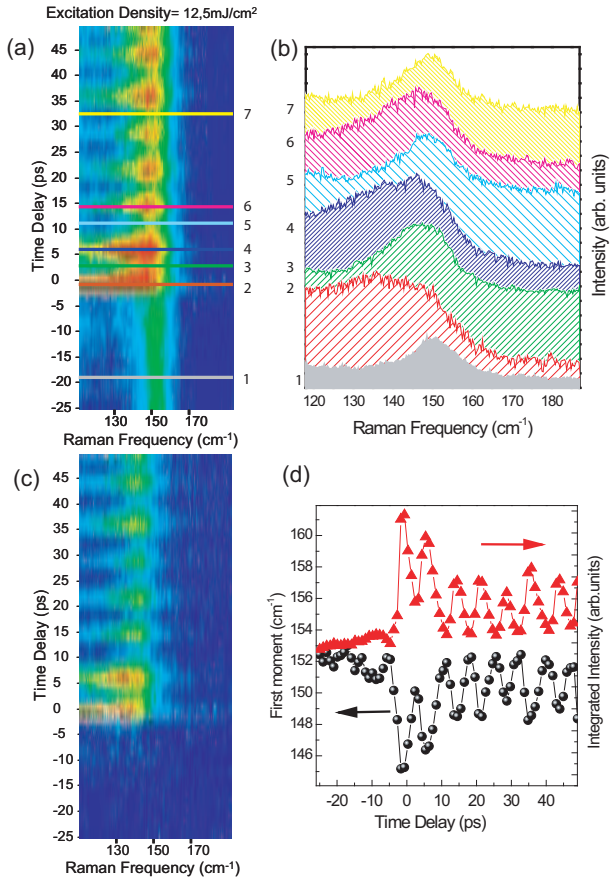

Figure 5.12: *(a) Transient Raman response for high pump excitation density 11mJ/cm^2. The response appear to be modulated with the anomalous periodicity of 7,2ps. (b) The Raman response at different times is plotted with an offset for clarity (the lines in (a), with number associated, indicates the time where the spectra in (b) are taken). (c) Transient Raman, as in (a), subtracted of an average of the spectra at negative times. (d) First moment and integrated intensity of the experimental feature.*

The anomalous periodic modulation of the Raman feature remain unexplained at the present date. Fig.5.12(d) shows the calculated first moment and of the

intensity of the Raman scattering feature. It's clearly visible that the central frequency and the intensity are anticorrelated, the higher the intensity, the lower the first moment of the spectra. To give a tentative explanation of this feature we performed the fit using three Lorentian distributions, one accounting for the background and two to reproduce the equilibrium (L1) and induced (L2) spectral characteristic. As described before the central frequency and width of L2 was kept constant at 138cm^{-1} and 13cm^{-1}. The only parameters allowed to vary were the characteristic of L1 and the intensity of L2. Fig.5.13 (a) shows that the fit parameters obtained. The extremely good agreement at all time delay is demonstrated by the low and roughly constant χ^2 (defined as $\chi^2 = \sum_i \frac{(I_i^{exp} - I_i^{fit})^2}{n_{points} - n_{parameters}}$).

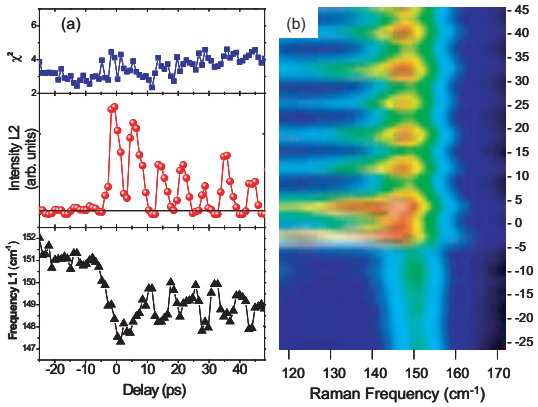

Figure 5.13: *(a) Fit parameters obtained with the function described in the text. The central frequency of L2 was kept constant at 138cm^{-1} with a width of 13cm^{-1}. The top panel reports the $\chi^{(}2)$ of the fit demonstrating the good agreement between the data and the fit at all time delays. The middle and bottom panels depict the intensity of L2 and the central frequency of L1, respectively. (b) Two dimensional plot of the fit obtained.*

The central and bottom panels of Fig.5.13 (a) plot the intensity of L2 and the central frequency of L1. Following this analysis, the periodic modulation of the the Raman response demonstrates a periodic switching between the two phases. Tentatively, the modulation could be ascribed to the interplay between the two phases. When the electron density exceeds the critical value, domains of the perturbed ("possibly cubic" or disordered) phase could start interacting. The beating between the two phases could be at the origin of the anomalous modulation of the Raman response. Further theoretical and experimental work should be carried out to give fundament to this new intriguing scenario. From the theoretical point of view the relative stability of the two phases should be calculated and the existence of locally distorted configuration equivalent in energy to the

undistorted one should proved. From the experimental point of view the limiting factors of our experiments were two. Firstly, the high repetition rate (80MHz) of the laser used produce piling up effects due to successive pulses allowing us only a partial exploration of the high excitation density limit. Secondly, the experiment with pump and probe at the same frequency (perpendicularly polarized) didn't allow the analysis of the E_g mode, whose Raman tensor has both diagonal and off diagonal elements. Time resolved Raman experiments with a lower repetition rate and two different colors (pump and probe) would help unraveling the physics underling the anomalous beating observed.

5.4 Conclusions

In conclusion the transient spontaneous Raman response have been measured in Bismuth and Antimony single crystals. On the phonon response two different dynamics were distinguished: a fast non thermal one in the first 10ps is followed by a slow relaxing dynamic lasting for all the time window investigated. The slow response have been proven to be due to the thermodynamical perturbation of the system. The fast non-thermal dynamics was described in terms of a the collapse of the Peierls gap. In the spirit of the Landau theory of phase transition the Jones-Peierls distorted natural phase is considered to be derived from a non thermally accessible cubic phase. The phonon lineshape observed in the fast dynamics revealed the appearance of a new phonon mode at the threshold excitation density of 5mJ/cm^2. This was interpreted as the evidence of the coexistence between the A7 structure (pushed towards the simple cubic undistorted phase) and a new non-thermodynamic phase possibly due to the local collapse of the Peierls gap. An anomalous periodic modulation of the Raman response for excitation density close to the damaging threshold has been tentatively ascribed to the periodic beating between the two phases. Further investigation are suggested to give fundament to this intriguing scenario.

5.5 Appendix A: The Jones-Peierls mechanism

The Jones-Peierls mechanism is based on the idea that the distorted lattice has a lower frequency, leading to the presence of two non-symmetry-related site for the atoms within the unit cell. The number of orbital states in the new zone is equal to the number of cells, and therefore half the number of atoms. In this picture the symmetry of the distorted lattice ("*neglecting the distortion*") is that of a face centered cubic lattice. Fig. 5.14 reveals the comparison between the two unit cells and Brillouin zone. In particular, Fig 5.14 (d) depict the the comparison between the Brillouin zone of the simple cubic (SC) versus the face centered cubic (FCC) ones. It is noticeable that the FCC Brillouin zone is inscribed into the SC one. Jones argued that the new surface of discontinuity illustrated in Fig.5.14 (d) is very near to the surface of constant energy surface in the undeformed lattice. This means that in Bi and Sb the Fermi surface would very nearly coincide with the new boundary. This introduces a small band-gap over extended regions of the Brillouin zone and is responsible for the semimetal character of Bi and Sb.

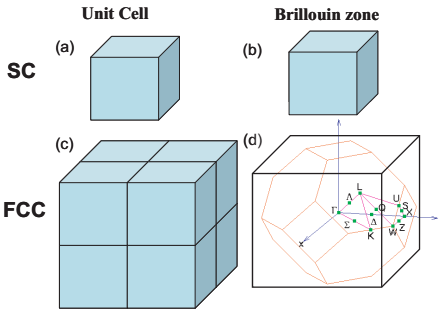

Figure 5.14: *Sketch of the simple cubic primitive cell (a), with the relative Brillouinzone scaled by a factor 2π (b). The face centered cubic unit cell is depicted in (c). The Brillouin zone for the SC and FCC cubic cell are compared in (d). See text for the discussion.*

5.6 Appendix B: The Phonon frequency from the free energy

To calculate the phonon frequency for a fixed number of electrons excited in the conduction band we Taylor-expand the free energy in the vicinity of the equilibrium position q_n.

$$E_{q\simeq q_n}(n) = E(q_n) + E'(q_n)(q - q_n) + \frac{E''(q_n)}{2}(q - q_n)^2 + ho. \tag{5.9}$$

The first term of Eq.5.9 is a q-independent shift of the energy and will not affect the vibrational frequency. The second one vanishes, being q_n an "equilibrium" position $E'(q_n) = 0$. The only term determining the vibrational frequency is the last one. The equation of motion is:

$$\mu n_0 \ddot{q} = -\frac{dE}{dq} = (4an_0 - 4c_2 n)(q - q_n) \tag{5.10}$$

This is the standard harmonic oscillator equation, where the frequency is reported in Eq.5.5.

Bibliography

[1] *More surprises in theoretical physics* (Princeton University Press, New Jersey, 1991).

[2] D. M. Fritz, D. A. Reis, B. Adams, Science **315**, 633 (2007).

[3] E. D. Murray, D. M. Fritz, J. K. Wahlstrand, S. Fahy, D. A. Reis, Phys. Rev. B **72**, 060301(R) (2005).

[4] H. J. Zeiger, J. Vidal, T. K. Cheng, E. P. Ippen, G. Dresselhaus, M. S. Dresselhaus, Phys. Rev. B **45**, 768 (1992).

[5] T. H. Cheng, S. D. Brorson, A. S. Kazeroonian, J. S. Moodera, G. Dresselhous, M. S. Dresselhous, E. P. Ippen, Appl. Phys. Lett. **57**, 1004 (1990).

[6] G. A. Garret, T. F. Albrecht, J. F. Whitaker, R. Merlin, Phys. Rev. Lett. **77**, 3661 (1996).

[7] A. B. Shick, J. B. Ketterson, D. L. Novikov, A. J. Freeman, Phys. Rev. B **60**, 15484 (1999).

[8] M.F. DeCamp, D. A. Reis, P. H. Bucksbaum, R. Merlin, Phys. Rev. B **64**, 092301 (2001).

[9] O. Degtyareva, V. V. Struzhkin, R. J. Hemley, Solid State Comm. **141**, 164 (2006).

[10] M. Hase, M. Kitajima, S. Nakashima, K. Mizoguchi, Phys. Rev. Lett. **88**, 067401 (2002).

[11] S. Fahy, D. A. Reis, Phys. Rev. Lett. **93**, 109701 (2004).

[12] M. Hase, K. Mizoguchi, H. Harima, S. Nakashima, Phys. Rev. B **58**, 5448 (1998).

[13] T. J. Fox, R. P. Howson, D. C. Emmony, J. Phys. D **7**, 1864 (1974).

[14] O. V. Misochko, M. Hase, M. Kitajima, J. Phys.: Condens. Matter **16**, 1879 (2004).

[15] P. Stampfli, K. H. Bonnemann, Phys. Rev. B **49**, 7299 (1994).

[16] V. S. Edel'man, ADVANCES IN PHYSICS **25**, 555 (1976).

[17] V. M. Kopylov, L. P. Mezhov-Deglin, ZhETF Pis. Red. **14**, 32 (1971).

[18] J. Höhne, U. Wenning, . Schulz, S. Hüfner, Z. Physik B **27**, 297-302 (1977).

[19] H. Iwasaki, T. Kikegawa, Acta Cryst. B **53**, 353-357 (1997).

[20] K. Socolovski-Tinten, C. Blome, J. Blums, Nature **422**, 287 (2003).

[21] R. Tediosi, N. P. Armitage, E. Giannini, D. van der Marel, Phys. Rev. Lett. **99**, 016406 (2007).

[22] O. Degtyareva, V. V. Struzhkin, R. J. Hemeley, Solid State Comm. **141**, 164-167 (2007).

[23] M. I. McMahon, O. Degtyareva, R. J. Nelmes, S. van Smaalen, L. Palatinus, Phys. Rev. B **75**, 184114 (2007).

Chapter 6

Evidence of a Non-Thermal Phase in $(EDO\text{-}TTF)_2PF_6$

6.1 Introduction

The organic charge-transfer salts with composition A_2B, where the A molecule is an electron donor (hole acceptor) and the B an acceptor (hole donor), provided a beautiful playground for studying the interplay between the electronic, vibrational and spin degrees of freedom. The presence of competing on-site and nearest neighbor Coulomb repulsion, a variety of hopping parameters and important charge-lattice coupling leads to a huge variety of ground states. Indeed a variety of different phenomena have been reported, such as Metal-Insulator transitions[1], superconductivity[8], magnetic frustration[10] and even ferroelectricity[11].

Recently, a quasi-1D, $\frac{1}{4}$-filled A_2B organic salt $(EDO\text{-}TTF)_2PF_6$ has been synthesized[2] and found to undergo a metal to insulator (M-I) transition at relatively high temperature (T_c = 278 K) (Fig.6.1). The ionic crystal consists of negatively charged PF_6(-1e) groups and positively charged EDO-TTF molecules (+0,5e per molecule). The EDO-TTF molecules have an almost flat shape and are stacked head to tail along the metallic c-axis (see Fig.6.1). The PF_6 anions are located between the EDO-TTF planes and have interactions with the ethylene groups. The metallic behavior at high temperature originates from the charge delocalization along the EDO-TTF chain. Lowering the temperature K the system becomes insulating at $T_c = 278$ via a first order phase transition. At this transition half of the EDO-TTF molecules bend and simultaneous charge ordering (CO) takes place: the flat molecules acquire a positive charge $\simeq$ 1e and the bent ones become neutral (Fig.6.1,(a)). At the M-I transition the unit cell doubles, but the overall symmetry does not change: both phase belong to the $P\bar{1}$ space group. From the experimental point of view the M-I transition results in markable changes in the resistivity[2], Raman spectra[12], and optical properties[4]. The thermody-

namical properties suggest that the first order character of the phase transition results from a catastrophic cooperation of multiple instabilities: Peierls instability, charge order, and anion ordering[5]. Fig.6.1(b) depicts the charge distribution of the metallic phase, where all the EDO-TTF molecules have a positive charge of $\frac{1}{2}$e, we will denote this charge state as $|..\frac{1}{2}\frac{1}{2}\frac{1}{2}\frac{1}{2}\frac{1}{2}\frac{1}{2}\frac{1}{2}\frac{1}{2}..>$. As shown in Fig.6.1(a), the charge ordered state consists of two neighboring singly charged molecules followed by two neutral ones, we'll denote this state as $|..01100110..>$. The fact that the charge ordered state is not the Coulomb favorable one $|..01010101..>$ already demonstrate that a Wigner-like model is too simplistic to describe the ground state physics of this system and that the elastic energy, and eventually the dipole interaction between the molecules should be taken into account (see Appendix).

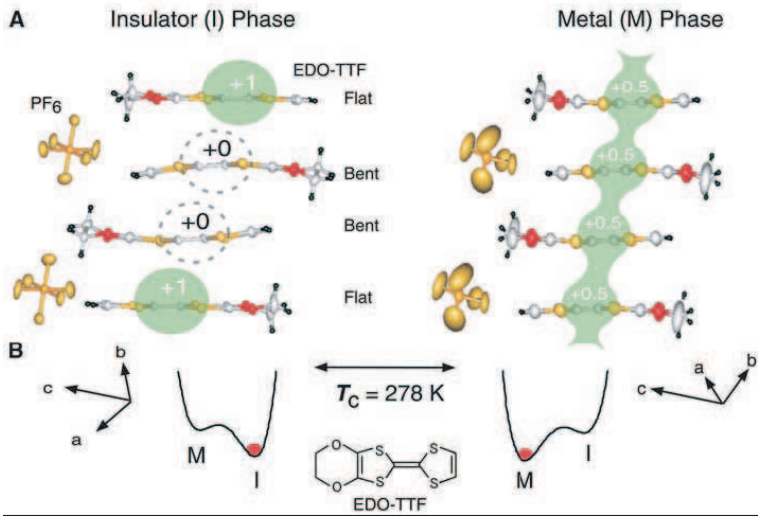

Figure 6.1: *(a) Sketch of the structural deformation reported at the Metal-Insulator Phase transition happening at 278K. The figure depicts the structural changes happening at T_c together with a sketch of the molecular charge state. (b) Schematic for the free energy changes associated to the metal-insulator transition (The figure is reprinted from Ref.[1], Copyright (2005) by Science).*

Recently a pump and probe study of the $(EDO\text{-}TTF)_2PF_6$ crystals revealed that an ultrafast, photoinduced phase transition from the insulator phase to the metal one can be induced with very weak excitation intensity[1]. Two striking feature were revealed. The first one was the strong collectiveness of the induced phase transformation: irradiating the sample with 100fs light pulses at 800 nm with a density of one photon per 500 molecules already switches half of the material from the insulating to the metallic state. The second one was the huge coherent response observed in the first few ps of the transient reflectivity at the

characteristic frequency of intramolecular vibrational modes. These evidences led to the discussion of the optically induced phase transition in terms of cooperative melting of charge order assisted by coherent phonon generation. The observed anomalous broadening of some vibrational modes was ascribed to dynamical fluctuations of the site-charge density due to the correlation effects[4]. The strong absorption feature at 800 nm, measured in the linear regime, was assigned by a Hubbard calculation to a transition from the the ground state ($|..0011001100..>$) to an excited state characterized mainly by a $|..002000200..>$ charge state. How this photo induced state results in a metallic one is still debated; we remind that the high temperature metallic phase is characterized by a $|..\frac{1}{2}\frac{1}{2}\frac{1}{2}\frac{1}{2}\frac{1}{2}\frac{1}{2}\frac{1}{2}\frac{1}{2}..>$ charge distribution. The transient metallic phase is induced immediately after the irradiation (within a few ps), and it relax back to the insulating state quite slowly in $\approx 100\mu$sec. Our low frequency continuous wave (CW) Raman measurements revealed the presence of low frequency Raman modes, assigned with the help of semi-empirical calculations, to molecular vibrations corresponding to the bending distortion observed in the x-ray measurements. This strongly suggest that the strong "coherent" response observed in the first few ps could indeed play a key role in the photo-induced phase transition. In addition to this the dynamical Raman spectra measured will help in addressing the structural characteristics in real time after irradiation. The time resolution of the setup used is $\approx 10\mu$sec so that the aim is not to map how the phase transition is induced (to fast for our time resolution), but to follow the recovery of the ground state.

6.2 Transport Measurments

The thermal CO transition at $\simeq$280K is characterized by a dramatic change in the resistivity. A two point resistivity measurement was performed. The transport properties were characterized with a two point measurements on a single crystal of 500 μm. The measurements were performed while cooling the sample in a flow cryostat. The low field resistivity was measured for temperature across the phase transition with a constant applied voltage of 1 V, while the I-V curves were measured driving variable currents in the sample and measuring the related voltage. The inset of Fig.6.2 reports the low voltage resistivity as function of temperature. It is clear that at the phase transition temperature the resistivity shows a sudden change of 3 order of magnitude as previously reported in [2]. The hysteresis observed between the cooling (red) and heating (blue) measurement is a clear indication of the first order character of the phase transition. It should be noted that the resistivity of the high temperature phase measured after the cooling process was twice the one before the cooling (the difference is not visible on the logarithmic scale of the inset). This indicate that the cooling process could cause a substantial increase of the density of defects in the crystal. The main panels of Fig.6.2 shows the conductivity as a function of applied voltage for different temperatures below the phase transition. For temperatures close

to the phase transition the conductivity shows an Ohmic behavior over a wide voltage range. At 260K, for example, the conductivity is constant over nearly all the voltage range explored. It shows some non linearity only for extremely low ($<10^{-4}$ V) and high ($>$ 10V) applied fields. The high field anomaly is due to experimental artifacts. This non-linearity is probably due to heating effects: the increased power dissipation in the sample leads to a temperature increase, and thereby to a reduced resistance. Let us focus now on the low field measurements.

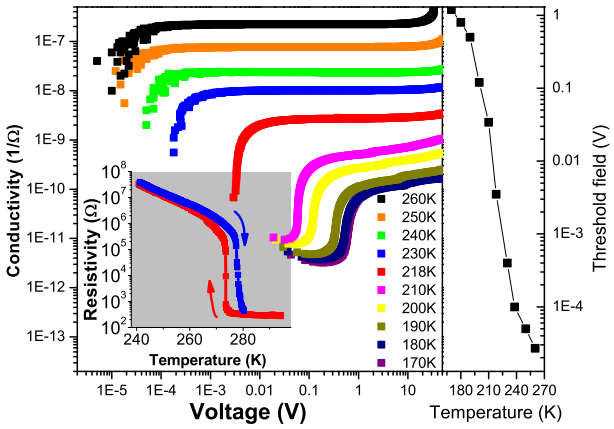

Figure 6.2: *Transport characterization of the two phases. The conductivity measured as a function of the applied voltage for different temperatures below the MI phase transition. In the inset the resistivity measured at different temperature (V= 2.5 V).*

At low temperature two conduction regimes are clearly visible. In the first one, dominating at low applied fields, the conductivity is low (see for instance the lower curves in Fig.6.2). Upon increasing the fields the conductivity remains constant up to a critical field. At this critical field the conductivity abruptly increases entering a second Ohmic regime, where the conductivity is again constant for further increasing of the field. The change in resistivity between the two regimes depend on the temperature and are up to almost two order of magnitude. The threshold field necessary to enter the high conductance regime decreases with increasing temperature. Close to T_c the conductivity in low field is only slightly smaller than the one in high field, and it become difficult to detect the threshold field within the experimental error. For temperature above 240K the decrease of the conductivity at low fields could be either an experiment artifact (due to the small field applied) or a precursor of the threshold behavior.

Nonlinearities in the conductivity are a typical feature in low dimensional charge ordered materials[13]. In the charge ordered ground state they only ex-

hibit ohmic conductivity below a certain threshold field. Below this, the charge density modulation is pinned by lattice, impurities, defects, and grain boundaries and the conductivity is solely due to a strongly temperature dependent quasi-particle transport. For fields above the threshold field, the conductivity becomes strongly enhanced and nonlinear due to the contribution of the now moving depinned charge order modulation. Increasing the temperature would reduce the pinning of the charge order modulation increasing thereby the threshold field[13]. In analogy with that, in the charge ordered phase of EDO-TTF_2PF_6 the transport is dominated by electron hopping between EDO-TTF molecules. The presence of charge order domains or defects in the crystal would result in similar localization effects, finally leading to a "threshold" behavior of the conductivity. Close to T_c the localization effects would be weak due to the screening of the impurities and an extended Ohmic behavior is revealed. Decreasing the temperature two effects could be responsible to the increase of the threshold field plotted in Fig.6.2(b). The increasing number of defects (shown also in the low field temperature dependence), together with the reduced thermal screening of them could increase the localization effects, finally resulting in an increase of the threshold field.

6.3 Raman Spectroscopy

6.3.1 CW-Low Frequency Raman Mode

As mentioned in the introduction, the transient reflectivity measurements performed to investigate the photo-induced metal to insulator transition revealed in the first picoseconds after pump irradiation the presence of an intense coherent response[1]. This, together with the measured low excitation threshold ($\simeq$1Photon/500molecules) suggested the cooperativity of the photo-induced phenomena. The periodicity of the coherent response measured was 0,5ps, corresponding in the frequency domain to $\simeq 80 cm^{-1}$. Our Raman measurements, shown in Fig.6.3, confirm the results previously reported[12] and revealed the presence of a series of Raman active modes at low frequency. The assignment of the low frequency modes in organic molecular crystals is hampered by the coexistence of "molecular" and "crystal" modes. EDO-TTF molecules are quite extended and therefore exhibits quite a number of low frequency molecular modes. Table 6.1 reports a comparison between the experimental frequencies and the calculated ones. The calculation reported are done for single molecule in the neutral and charge state. A semi-empirical approximation optimized for organic molecule is used (PM3). This comparison allows a tentative assignments of the experimental frequencies to particular vibrational modes. The two lowest frequency modes (25 and $39 cm^{-1}$) are assigned to the lowest modes coming out the theoretical calculation. The calculations showed that they correspond to an vibrational mode perpendicular to the molecular plane of the neutral and charged molecules (Tab.6.1, a sketch). The same is for the modes at 57 and 110 wave number (b).

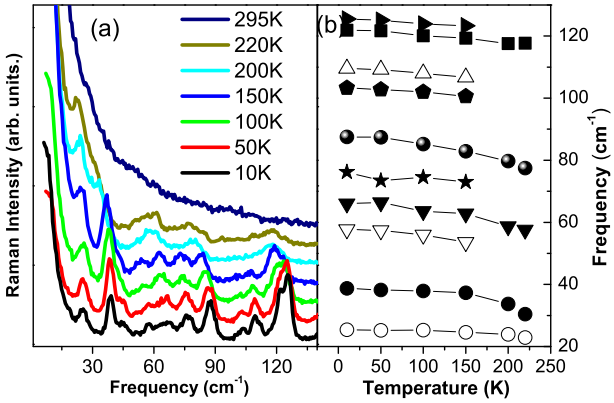

Figure 6.3: *(a) Low frequency Raman spectra at different temperature across the metal-insulator transition (unpolarized spectra). (b) Temperature dependence of the frequency of the different modes in (a).*

The 95 and 99 mode are vibrational modes in the molecular plane (d), while 117 and 128 are again vibrational modes perpendicular to the molecular planes with multiple node (c). From this assignment appears that in the energy region of the 67, 76 and 86cm^{-1} features no intramolecular mode is present in the single molecule calculations. Even though it is not possible to exclude that the crystal environment change significantly the intramolecular vibrational frequency, our measurements and calculation suggest that these modes should be assigned intermolecular vibrations, either the EDO-TTF¡-¿EDO-TTF or the EDO-TTF¡-¿PF$_6$. The 86cm^{-1} feature, as discussed, is the mode appearing in the giant coherent response observed in the time domain. The optically induced phase transition was suggested to be a cooperative effect mediated by this vibrational mode. Indeed, our measurements and calculations suggest that the $86cm^{-1}$ wave number mode has a itermolecular nature, therefore involving extended region of the crystal.

Table 6.1: *Experimental frequencies compared with the single molecule theoretical calculation. The energies are reported in cm^{-1}. The first columns report the experimental values, while the second and the third one the calculated value for the neutral and +1e charged EDO-TTF molecule. The motion associated to the vibrational frequency indicated in the forth column refers to the sketch in the right figure.*

E_{exp}	Neutral EdoTTF	+1e EdoTTF	Sketch
25	20		(a)
39		48	(a)
57	58		(b)
67			ext.
76			ext.
86			ext.
103	95		(d)
110		98	(b)
122		99	(d)
	117		(c)
126		128	(c)

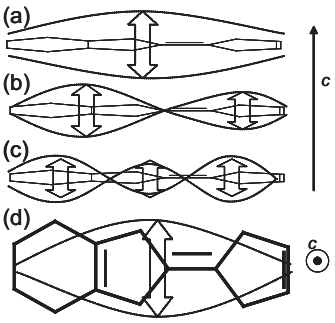

6.3.2 High Frequency

The charge order nature of the phase transition described ([6]) indicate the presence of two different charge state in the insulating low temperature phase. The frequency of the phonon mode associated to the C=C double bond is expected to be sensitive to the overall charge state of the EDO-TTF molecules. Fig.6.4 shows the temperature dependence of the C=C vibrational frequency. The inset in the graph shows a sketch of the C=C mode. At 180K the presence of two different vibrational frequency at 1407 and 1480cm^{-1} has been interpreted as a confirmation of the presence of two different charge state of the EDO-TTF molecule in the charge ordered state. The low and high frequency modes are assigned to different C=C vibration of the positively charged molecule[4]. Increasing the temperature a new vibrational mode at 1415cm^{-1} become visible. Between 210K and 240K the coexistence of the low and high temperature charge state is made evident by the coexistence of the three modes. At temperature close to T_c, T=270K, the cross section of the vibrational modes, already in the high temperature charge state, becomes larger. Fluctuation may play a role in enhancing the molecular polarisability and thereby also the Raman cross section. It is interesting to notice that the Raman spectra at 270K resemble already the one of the high temperature phase, while the transport properties revealed the phase transition to be at higher temperature (280K). Even though it is not possible to exclude local laser-induced heating on the sample, the low power used for this measurements ($\simeq$ 1J/cm^2s) suggest that the explanation may resides in a different physical phenomenon. The

charge ordering and the structural transition may happen at a different temperature. This would be supported by the presence at 270K of additional modes at higher frequency. In fig.6.4 the vertical black arrows above the 270K measurement indicate where these high energy modes appear. Unfortunately the quality of the measurements doesn't allow to distinguish clearly the high energy modes (barely visible) in the 270K trace. Above the phase transition temperature (295K) the presence of only one vibrational mode is a clear indication of a uniform charge state of the EDO-TTF molecules in the metallic phase.

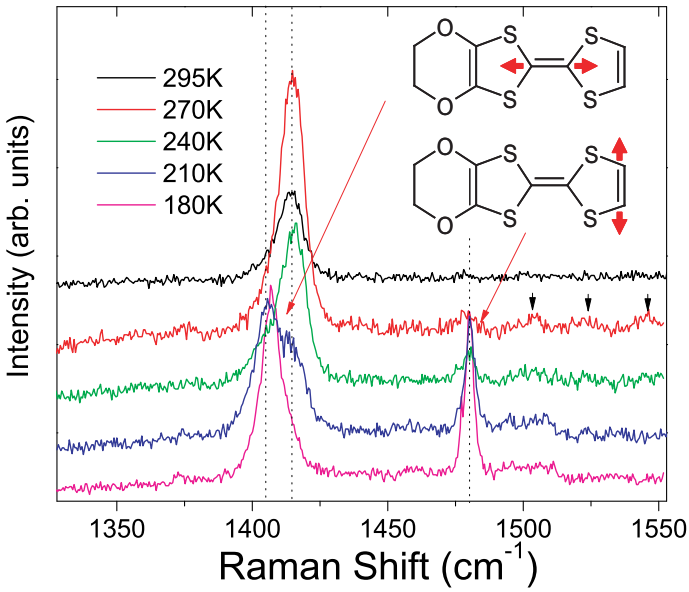

Figure 6.4: *Temperature dependence of the high energy mode of the EdoTTF molecule. The picture shows a sketch of the atomic displacement of the mode observed.*

6.3.3 Dynamical probes of the optically induced phenomena

Experiments The experimental setup used for pump and probe measurements on the μsec time scale is described in chapter 4. Short light pulses of 15-20μsec at 532nm are produced at a repetition rate of 1KHz with a custom designed mechanical chopper. The chopper was synchronized with an amplified Ti:Sapphire laser producing 100fs pulses at 800nm at 1KHz repetition rate. The 532nm light was used as probe while the 800nm was the pump. The probe intensity was kept below $100\mu J/cm^2$. The delay between the pump and the probe was controlled via the phase of the chopper with respect to the synchronization wave. All the measurements were performed in the Raman microscope coupled with a cryostat

(see chapter 4). For the Raman measurements the pump and probe leaving the microscope collinearly were coupled into the spectrometer. The accumulation times for the Raman spectra were set to 7 hour. The Raman response of the 532nm light was analyzed as a function of the delay between pump and probe. For the reflectivity measurements the pump and probe beam were spectrally filter, with a color filter allowing only the 532nm light through and subsequently measured with a diode optimized for visible light. A second chopper was added on the pump beam, so to allow a lock-in detection as in standard pump&probe experiments[9].

Results and Discussion To discuss the optically induced effects on EDO-TTF_2PF_6 we will at first make use of the experimental setup described with pump&probe overlapped in time. In this way the optically induced phase are characterized in all the excitation density regimes, from the unperturbed sample up to the irreversibly photo-damaged one. In a second moment at a suited power density the dynamics will be discussed comparing the transient reflectance to the transient Raman. Fig.6.5 shows the pump power dependence of the Raman spectra for pump and probe overlapped in space an time. The low temperature phase modes, at 1407cm^{-1}) and at 1480cm^{-1}, disappear increasing the excitation power. At the same time a new vibrational mode continuously appear at 1461cm^{-1} which is not present in the low power experiments in either of the thermal phases. Fig. 6.5 (b) depict the intensity of $\nu 1$ and of δ as a function of the pump power. It is clear that the intensity of δ is anticorrelated with the one of $\nu 1$ and $\nu 2$. The threshold behavior reported for the optically induced phase transition investigated was 0,12mJ/cm^2 per pulse[1]. In our measurement the critical power for inducing the phase changes is one order of magnitude larger ($\simeq$2mJ/cm^2). This is an indication that the electronic dynamics are not directly coupled to the structural dynamics. The enormous changes in the near infrared reflectivity at relative low power do not seem to correspond to a structural phase transition. Up to the excitation density of 2,8mJ/cm^2 the Raman features appear to be reversible, while at the highest power 3,7mJ/cm^2 a mechanical damage visible under an optical microscope was induced on the sample.

At the excitation density of 2,8mJ/cm^2 (Fig.6.5, blue curve) a reversible change is detected. Together with the appearance of the mode at 1461cm^{-1} characterizing the damaged phase, a broad feature between 1500 and 1600cm^{-1} become visible. The fact that this broad feature is not observed in the damaged phase suggest that it is due to a dynamic different from the one inducing the damage. We tentatively assign this feature to the presence of different transient charge states for the EDO-TTF molecules. The last, and probably the most important, outcome of this measurement regards the nature of the optically induce phase. As shown in Fig.6.4 the high temperature metallic phase is characterized by the presence of a phonon at 1415cm^{-1}. No traces of such a vibrational characteristic is found in the optically induced state at any excitation power. Hence, the nature of the optically induced metallic "state" seems different from both the

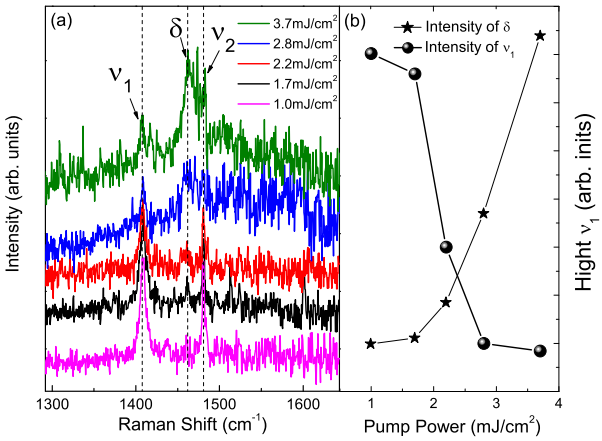

Figure 6.5: *(a) Pump power dependence of the Raman response in the C=C mode frequency region. The low temperature spectra is revealed to disappear continuously while new vibrational feature appear increasing the excitation density. (b) Intensity of the mode $\nu 1$ typical of the unperturbed phase and of δ characterizing the photo-induced phase.*

thermodynamically stable phases.

Phase Transition Dynamics To investigate the dynamics of the optically induced state we compare the transient reflectivity and the Raman response for 800nm pump and 532nm probe. Fig. 6.6 (b) shows the transient reflectivity changes for different excitation density, the probe intensity was kept constant at $200\mu J/cm^2$. The reflectivity shows a sudden change following the pump irradiation. The raise time was reported to be in the order of a picoseconds and therefore not resolvable with the time resolution of our experiments. The decay times measured confirmed the previously reported of $\simeq 50\mu s$[1]. The absolute value of the reflectivity changes increase with the excitation density between 1,5 and 2,8mJ/cm^2. No changes in the reflectivity is resolvable within our experimental resolution for excitation density below 1mJ/cm^2. The square dots show the measurements with excitation density at 0,9mJ/cm^2. The threshold behavior in the reflectivity measurement appear to be lower than the one measured in the Raman response ($I^{threshold}_{Reflectivity} \simeq 0,5 I^{threshold}_{Raman}$). This evidence, once more, suggest that the electronic dynamics seem to be unrelated to the structural ones. To explore the dynamics of the structural changes, the transient Raman response for excitation density of 2,8mJ/cm^2 was measured. The results are reported in Fig.6.6 (a). On a time scale faster than our experimental resolution (20μsec) the Raman

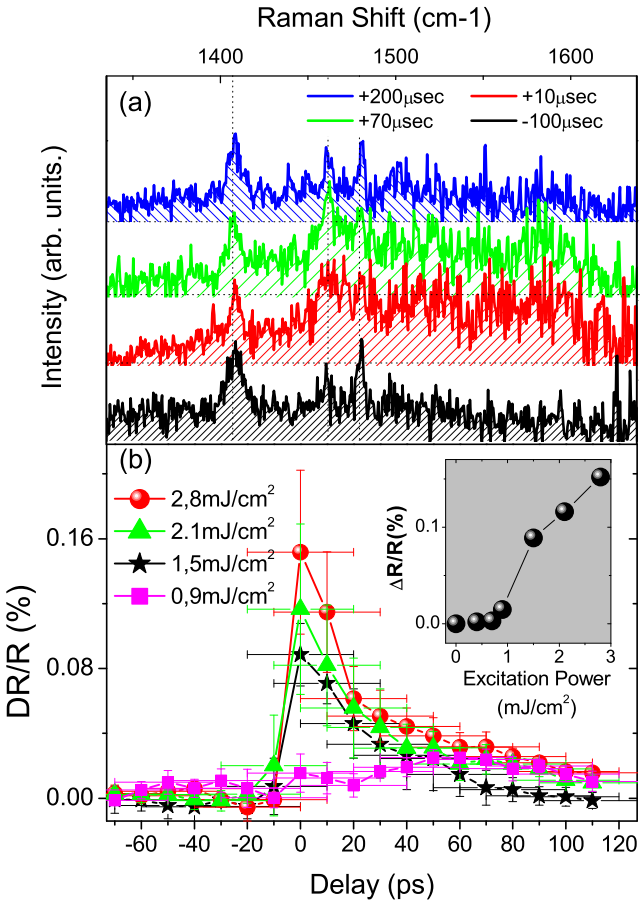

Figure 6.6: *(a) Transient Raman response in the C=C mode frequency region at 2,8mJ/cm^2 excitation density. The negative spectra revealed the presence of the low temperature modes. A transient response is observed between 1450 and 1600cm^{-1}. For positive time delays. ((b) Transient reflectivity at different pump power. The inset shows the maximum ΔR as a function of the pump power.*

modes in the C=C stretching region are perturbed. The mode at 1408cm^{-1} does not seem to be strongly affected by the optical perturbation. On the other end between 1450 and 1600cm^{-1} a broad band is induced by pump irradiation. The high energy mode(1480cm^{-1}) disappear into this broad background. The red, green and blue curve in Fig.6.6(a) corresponds to the Raman response measured 10, 70 and 200μs after the pump irradiation. It is clear that the optically induced

state disappear within the 200μs delay of the last measurement. Even though the quality of our measurements don't allow a detailed analysis of the Raman features, the presence of a broad band in the energy region of a C=C bond is possibly due to the presence of different charge states for the EDO-TTF molecules or to a transient disorder state perturbing the molecular phonon frequencies.

6.4 Conclusions

The optically induced phase transition for (EDO-TTF)$_2$PF$_6$ was investigated. The low temperature equilibrium phase was characterized by transport measurement. A non linear behavior of the conductance was discussed in terms of the presence of domains/disorder into the charge order phase. The Raman response in the low frequency region shows the appearance of various new vibrational modes at the charge order transition temperature. A single molecule calculation allowed us to distinguish between the intramolecular and intermolecular mode. The mode previously reported in the time domain measurements was assigned to intermolecular excitation. This gives plausibility to the suggested scenario of a phonon mediated collective behavior of the optically induce phase transition. The dynamical Raman response of the optically induced phase suggests the presence, in the optically induced transient, of EdoTTF charge states different from the ones of both the thermally accessible phases.

6.4.1 Appendix: Relative Phase Stability of a one dimensional charged chain

The anomalous charge ordered (CO) state of the EDO-TTF chains has been ascribed to a cooperation between dipole interactions and lattice distortions contributing to the free energy of the ground state configuration[1]. A large difference in the dipole moments of the charged and neutral molecules would favor the order observed experimentally. In addition to this, a structural deformation allowing neighboring charged molecules to increase their distance would also contribute to favor the observed |..001100.. > CO over the Coulomb favorable one |..01010101.. >.

The purpose of this appendix is to give a qualitative argument to shows how dipole interactions can drive the Coulomb favorable order |..01010101.. > to be replaced by the one observed experimentally (|..001100.. >). The approach we use is the following, we will calculate the Coulomb energy for an infinite linear chain with an average charge of 0.5e/site, for the two configurations |..01010.. > and |..001100.. >. We will do the same for the dipole interactions considering point dipoles under the condition that the distance between the molecule is much larger than the molecular size (point dipole). It should be also noted that the neighbors interaction is attractive, while the next nearest neighbor one is repulsive due to the "head to tail" stacking of the EDO-TTF molecules. Clearly, all this quantities will diverge, meaning that physically the charged chains is intrinsically unstable and stabilized in the $(EDO\text{-}TTF)_2PF_6$ crystals by the PF_6^- anions. On the other hand, comparing the two energy it is possible to get a hint on which one will be the ground state order.

We now consider the |..01010101.. > CO. The Coulomb repulsion can be written as:

$$E_C^{1010} = \frac{1}{4\pi\varepsilon_0}\sum_{i,j=1}^{\infty}\frac{q_i q_j}{d_{ij}} = \frac{1}{4\pi\varepsilon_0 d}\sum_{n=1}^{\infty}\frac{q_1^2}{n} \tag{6.1}$$

where $q_1$indicate the charge state of the molecules (+1) and d is the distance between two molecules. The final expression is obtained writing the total repulsion that an electron with charge 1 will experience from the other charged molecules in the chain, the 0 charge electron does not give any contribution.

The dipole attraction with dipoles p_1 and p_0 respectively for the charged and neutral molecules, can be written as:

$$E_D^{0101} = \frac{1}{4\pi\varepsilon_0}\sum_{i,j=1}^{\infty}\frac{p_i p_j}{d_{i,j}^3} = \frac{1}{4\pi\varepsilon_0 d^3}\sum_{n=1}^{\infty}[-\frac{4p_0p_1}{(2n-1)^3} + \frac{2(p_1^2+p_0^2)}{(2n)^3}] \tag{6.2}$$

We now consider the |..001100.. > CO. The electronic repulsion can be written as:

$$E_C^{0110} = \frac{1}{4\pi\varepsilon_0 d}\sum_{n=1}^{\infty}[\frac{2q_1^2}{(4n-3)} + \frac{4q_1^2}{4n} + \frac{2q_1^2}{(4n-1)}] \tag{6.3}$$

The dipole interaction for this configuration can be written as:

$$E_D^{0110} = \frac{1}{4\pi\varepsilon_0 d^3}\sum_{n=1}^{\infty} -\frac{2p_1^2+2p_0^2+4p_1p_0}{(4n-3)^3} + \frac{4p_0p_1}{(4n-2)^3} - \frac{2p_1^2+2p_0^2+4p_1p_0}{(4n-1)^3} + \frac{2p_1^2+2p_0^2}{(4n)^3}$$

So finally the relative stability of the $|..001100..>$ phase is given by the condition: $(E_C^{0101}+E_D^{0101})-(E_C^{0110}+E_D^{0110})>0$.

Considering a realistic distance between the molecules ($2\mathring{A}$), the conditions for the stability of the $|..001100..>$ phase are reached for a difference in the dipole moment of the charged and neutral molecule of $\sim$30 Debye. This value is more than one order of magnitude larger than the calculate value for the EDO-TTF molecules (charged and uncharged), suggesting indeed that a structural contribution to the free energy is necessary to stabilize the $|..001100..>$ ground state configuration. A more realistic calculation including extended dipoles and lattice energy would be needed to clarify this issue.

Bibliography

[1] M. Chollet, L. Guerin, N. Uchida, S. Fukaya, H. Shimoda, T. Ishikawa, K. Matsuda, T. Hasegawa, A. Ota, H. Yamochi, G. Saito, R. Tazki, S. Adachi, and S. Koshihara, Science **307**, 86 (2005).

[2] A. Ota, H. Yamochi, and G. Saito, J. Mat. Chem. **12**, 2600 (2002).

[3] A. Ota, H. Yamochi, and G. Saito, Synthetic Metals **135-136**, 643-644 (2003).

[4] O. DrozdovaBanfi, K. Yakushi, K. Yamamoto, A. Ota, H. Yamochi, G. Saito, H. Tashiro,and D. B. Tanner, Phys. Rev. B **70**, 075107 (2004).

[5] K. Saito, S. Ikeuchi, A. Ota, H. Yamochi,and G. Saito, Chem. Phys. Lett. **401**, 76-79 (2005).

[6] S. Aoyagi, K. Kato, A. Ota, H. Yamochi, G. Saito, H. Suematsu, M. Sakata,and M. Takata, Angev. Chem. Int. Ed. **43**, 3670-3673 (2004).

[7] H. Yamochi, G. Saito,and S. Koshihara, Mol. Cryst. Liq. Cryst. **455**, 105-112 (2006).

[8] D. Jerome,and H. J. Schulz, Adv. Phys. **51**, 293 (2003).

[9] D. M. Sagar, A. A. Tsvetkov, D. Fausti, S. van Smaalen, and P. H. M. van Loosdrecht, Journal of Physics: Condensed Matter **19**, 436208 (2007).

[10] Y. Shimizu, M. Miyagawa, K. Kanoda, M. Maesato, and G. Saito, Phys. Rev. Lett **91**, 107001 (2003).

[11] P. Monceau, F. Ya. Nad, and K. Brazovskii, Phys. Rev. Lett **86**, 4080 (2001).

[12] T. Hasegawa, *Study of lattice dynamics for some systems with static or dynamic structural distortions by first principles calculation and Raman scattering measurement* .

[13] S. Sirbu, P.H.M. van Loosdrecht, and T. Yamauchi, Y. Ueda, European Physical Journal B **53**, 289 (2006).

Memorie, Riflessioni ed Invito alla Lettura

Da bambino mi affascinava guardar la neve sciogliersi al sole. Ovviamente, allora, mai mi sarei immaginato che questo sarebbe stato l'inizio della sintesi della mia tesi di dottorato.

Avevo allora molti dubbi al riguardo, e forse ancora oggi li ho. Non mi spiegavo come materiali composti della stessa "*sostanza*" potessero avere proprietà tanto diverse: l'acqua trasparente e liquida, la neve opaca e soffice, il ghiaccio trasparente e durissimo. Oggi, il titolo di questa tesi "Transizioni di fase e fenomeni otticamente indotti in sistemi cooperativi" potrebbe essere riformulato:"La neve sciogliersi al sole, come la vedo oggi". Certamente meno scientifico, ma assai più divertente.

Una transizione di fase è una trasformazione di un sistema termodinamico, a composizione inalterata, da una fase ad un' altra. Le proprietà fisiche delle due fasi possono risultare molto diverse, così che la transizione può essere caratterizzata da un brusco (o meno) cambiamento delle proprietà fisiche del sistema. Le transizioni di stato solido-liquido, liquido-gassoso o solido-gassoso, come ad esempio la transizione di stato liquido-solido attraverso cui l'acqua è trasformata in ghiaccio, sono l'esempio più intuitivo di quanto una transizione di fase possa cambiare le caratteristiche fisiche di un materiale, senza cambiarne la composizione. Forse più difficili da intuire, ma non meno interessanti, sono le transizioni di fase solido-solido, che non coinvolgono un cambiamento di stato della materia, ma solo quello di alcune proprietà come la conduttività, la durezza, la densità o la magnetizzazione. Un esempio di trasformazione di questo tipo è rappresentato dalle proprietà magnetiche del ferro, che tutti conosciamo. A causa di una transizione da una fase "magnetica" ad una "non-magnetica", l'attrazione tra due calamite di ferro scompare se riscaldate sopra a 750 $^\circ$ C, mentre la struttura cristallina resta sostanzialmente inalterata fino a piú di 1300 $^\circ$ C.

L'interazione tra luce e materia giace alle fondamenta della nostra conoscenza della natura. Il nostro sistema visivo, infatti, fin dai primordi della razza umana, costituisce lo strumento principe di cui disponiamo per indagare la natura dei fenomeni. É solo possibile immaginare il numero di domande "scientifiche" che la

vista di un tramonto, di un cristallo di fluorite, di un arcobaleno, di un'eclisse, o semplicemente del cambio di colore delle foglie in autunno potesse suscitare in un nostro antenato. Sfuggiva ai nostri antenati, e forse a molti nostri contemporanei, che lo stesso nostro sistema visivo è basato sull'interazione radiazione-materia. L'interazione del "bagno elettromagnetico" in cui viviamo con la nostra retina è l'inizio del processo "di percezione" con cui formiamo le immagini degli oggetti nella nostra mente. Ovviamente, nella storia scientifica degli ultimi secoli, sono stati sviluppati moltissimi altri strumenti di indagine del mondo; ma è interessante notare come la maggior parte di essi si basi tuttora su diversi fenomeni di interazione radiazione-materia. In questo senso tutte le tecniche spettroscopiche di cui disponiamo, dall'analisi a raggi X alla spettroscopia infrarossa, si basano su processi di interazione radiazione-materia.

Allo stesso tempo però, la luce, oltre che come strumento di indagine, può essere usata come strumento con cui controllare le proprietà dei materiali. Per rendere il concetto in maniera intuitiva, risulta chiaro da vari esempi in natura come l'interazione tra luce e materia possa iniziare e guidare fenomeni fisici di diversa natura. L'esempio più intuitivo di fenomeno otticamente indotto è il riscaldamento: quando irradiato un materiale si surriscalda. Per tornare all'esempio che mi incuriosiva da bambino, la transizione di fase neve-acqua, dovuta al riscaldamento indotto dai raggi solari, costituisce un meraviglioso esempio naturale di *transizione di fase otticamente indotta*. L'energia portata dai raggi solari é assorbita dal ghiaccio e trasformata in energia termica (vibrazionale). Le vibrazioni, così eccitate, sono in grado di rompere i legami tra le molecole di acqua, inducendo lo scioglimento dei cristalli di neve. Oltre ai fenomeni otticamente indotti tramite riscaldamento, la luce può determinare processi che, non necessariamente causati dall'aumento della temperatura, sono il prodotto "diretto" dell'assorbimento. Per trovare un evidente esempio in natura, la fotosintesi nelle piante trasforma anidride carbonica ed acqua in ossigeno e glucosio, come diretta conseguenza dell'assorbimento di un fotone in una molecola; e questo avviene senza che la temperatura del sistema sia significativamente alterata.

La comprensione dei vari processi di interazione tra luce e materia non può prescindere dallo studio delle dinamiche dell'interazione stessa. In che modo l'eccitazione ottica perturba e modifica le proprietà dei materiali? Dopo quanto tempo queste proprietà sono alterate? Come si ritorna allo stato di equilibrio? Sono domande che, se da un lato aiutano nella comprensione del fenomeno, dall'altro aprono la strada per l'esplorazione delle proprietà fisiche dei sistemi, al di là dell'equilibrio termodinamico. La possibilità di manipolare lo stato di un materiale tramite irraggiamento e quindi di ottenere "fasi" transienti caratterizzate da proprietà, che possono essere diverse da qualsiasi configurazione raggiungibile termodinamicamente, è soggetto di innumerevoli studi negli ultimi anni. Un altro aspetto che fa di questa branca della fisica una delle piú interessanti e promettenti è il fatto che, tramite le tecnologie laser sviluppate nelle ultime due/tre decadi, è relativamente facile produrre in laboratorio impulsi luminosi estremamente corti (meno di 10^{-13} secondi). Questo fa sì che si possa pensare di controllare al-

cune proprietá dei materiali su scale temporali brevissime, aprendo la strada ad innumerevoli applicazioni nei campi più diversi: dall'elettronica ultraveloce alla micromeccanica. Oggi è solo possibile immaginare l'impatto che il controllo ottico di proprietá macroscopiche dei materiali potrà avere nei prossimi anni.

In particolare, il contributo di questa tesi è centrato su una tecnica spettroscopica chiamata spettroscopia Raman. Quando un quanto di luce (un fotone) interagisce con la materia, molti sono i processi possibili: assorbimento, diffusione, dispersione, etc. In particolare la spettroscopia Raman è basata sulla dispersione inelastica (inelastic scattering). Quando un fascio di luce ad una particolare energia interagisce con il materiale, una frazione molto piccola di fotoni ($10^{-8}/10^{-10}$ rispetto a quelli presenti nel fascio incidente) viene riemessa ad energie diverse. Tramite lo studio delle energie di questa luce dispersa è possibile studiare quali siano le eccitazioni caratteristiche del materiale e quindi estrarne informazioni dettagliate.

È interessante spendere qualche parola per spiegare la caratteristica che rende la spettroscopia Raman uno strumento unico per lo studio delle dinamiche fotoindotte e per lo studio di fenomeni non-termici. Due sono i processi di dispersione Raman. Nel primo, chiamato processo Stokes, l'energia dei fotoni dispersi è minore di quella dei fotoni incidenti e quindi un' eccitazione è lasciata nel sistema. Al contrario, in processi di dispersione del secondo tipo, Antistokes, l'energia dei fotoni in uscita è maggiore di quella dei fotoni in ingresso e quindi un'eccitazione risulta essere assorbita dal fotone. È facile intuire come i processi del secondo tipo (Antistokes) dipendano fortemente dalla presenza di eccitazioni nel sistema. Ad esempio in un cristallo a bassissima temperatura sono presenti pochissime eccitazioni (a 0K) e quindi nessuna eccitazione può essere assorbita dal fotone in uscita, così che i processi antistokes risultano avere intensità nulla. Come spiegato nell'introduzione a questa tesi, tramite il confronto delle intensità dei due processi (Stokes e Antistokes) è possibile determinare la temperatura specifica dell'eccitazione analizzata. In sistemi complessi le proprietà sono determinate dall'interazione tra diversi gradi di libertà: vibrazionale, magnetico ed elettronico. Tramite la spettroscopia Raman risolta nel tempo é possibile, potenzialmente, estrarre informazioni dettagliate sulle temperature dei diversi gradi di libertá. È facile a questo punto intuire quali siano le potenzialitá di questa tecnica per lo studio di dinamiche in sistemi complessi, in particolare per la caratterizzazione di quali dinamiche siano dovute a riscaldamento e quali invece siano di natura non termica.

Per concludere, il mondo finora inaccessibile della termodinamica di sistemi lontani dallo stato di equilibrio comincia ad essere esplorato. La possibilità di raggiungere proprietà inesistenti nella fase di equilibrio e di controllarle su scale temporali ultraveloci dischiude un mondo ancora in gran parte da scoprire, le cui leggi e le cui possibili applicazioni sono in gran parte inesplorate. Tutto ciò rende il lavoro dello "spettroscopista" nel ventunesimo secolo intrigante ed appassionante.

Sintesi dettagliata

Il lavoro riportato in questa tesi è diviso in due parti principali.

Nella prima parte (capitoli 2 e 3), la spettroscopia Raman standard (assieme ad altre tecniche) é stata utilizzata per lo studio strutturale e magnetico di transizioni di fase in due diverse famiglie di cristalli: $RFe_3(BO_3)_4$ (con R= Gd, Tb, Nd, Er e Y) e TiOX (con X=Cl e Br). La seconda parte della tesi (capitoli 4, 5 e 6) è dedicata alla descrizione della spettroscopia Raman dinamica sviluppata. Due sistemi diversi sono descritti (capitolo 4) ed applicati allo studio di transizioni di fase otticamente indotte in semimetalli (capitolo 5) ed in un sale organico (capitolo 6).

In particolare nel secondo capitolo abbiamo studiato una cascata di transizioni di fase caratteristica della famiglia di cristalli di "terrarara-ferroborati". Una transizione strutturale ad alta temperatura è seguita, a temperature piú basse, da transizioni di fase magnetiche (antiferromagnetica e spin-flop). Tramite lo studio Raman delle eccitazioni vibrazionali (fononi), abbiamo rilevato che la transizione di fase strutturale appartiene ad una categoria inusuale di transizioni, chiamata "transizioni debolmente del primo ordine" ("weakly first-order phase transitions"). Il parametro d'ordine della transizione di fase mostra un comportamento anomalo a metà tra quello caratteristico delle transizioni di fase del primo (isteresi) e del secondo ordine (evoluzione continua). Questo è spiegato dalla particolare simmetria cristallina di questa famiglia di cristalli. In aggiunta a questa peculiarità, l'analisi delle eccitazioni magnetiche rivela la presenza di correlazioni magnetiche a corto raggio fino a temperature molto elevate (10 volte la temperatura di Neel), dovute alla caratteristica bassodimensionale del sistema investigato.

Il terzo capitolo riguarda lo studio del diagramma di fase di un una classe di ossidi di titanio (TiOCl e TiOBr). La configurazione elettronica degli ioni di Titanio, assieme all'interazione prevalentemente monodimensionale tra essi, dovuta al caratteristico "splitting" degli orbitali d, fanno di questa famiglia di ossidi il candidato ideale ad una transizione Spin Peierls precedentemente osservata in un solo cristallo inorganico. Lo studio Raman della transizione di fase rivela due aspetti particolarmente interessanti.

La fase dimerizzata (Spin Peierls) è preceduta, a temperature piú alte, da una seconda transizione di fase, rivelando cosí la presenza di tre fasi stabili a diversa

temperatura.

La transizione alla fase dimerizzata risulta essere del primo ordine, in contrasto con il modello teorico della transizione Spin Peierls.

Lo studio dei modi vibrazionali ha permesso di determinare (assieme ad un'analisi a raggi X) la simmetria della fase spin Peierls e di rivelare una modulazione incommensurata con il periodo cristallino nella fase intermedia. Un modello in grado di spiegare l'anomalo carattere della transizione di fase Spin Peierls è stato proposto sulla base della simmetria della fase intermedia suggerita dallo studio dei modi vibrazionali misurati con spettroscopia Raman.

Nel quarto capitolo sono descritti e caratterizzati i vari apparati sperimentali utilizzati e sviluppati. All'inizio del capitolo è descritto l'apparato standard per la spettroscopia Raman in continua, usato nei capitoli 2 e 3. Nella seconda parte sono descritti e caratterizzati i due approcci seguiti per ottenere un'informazione Raman dinamica. Il primo approccio (per le misure del capitolo 6) è basato sull'utilizzo di un interruttore meccanico (chopper) e raggiunge risoluzioni temporali di 10 microsecondi (10^{-5} sec) combinate con risoluzioni in frequenza migliori di 1cm^{-1}. Il secondo approccio fa uso di tecniche interferometriche e di un laser ad impulsi corti e raggiunge risoluzioni temporali di qualche picosecondo (10^{-12} sec) a scapito della risoluzione in frequenza ridotta a 10cm^{-1}.

Nel quinto capitolo è riportato lo studio di due cristalli elementali di Bismuto e Antimonio. La fase termodinamicamente stabile di entrambi i materiali è caratterizzata da un comportamento semimetallico dovuto ad una distorsione di Peierls ("Jones-Peierls mechanism"). Tramite misure di Raman dinamico siamo riusciti ad evidenziare due dinamiche distinte: una dovuta ad un riscaldamento medio ed una di natura non termica. Siamo inoltre riusciti a dimostrare che, tramite eccitazione ottica di elettroni in banda di conduzione, è possibile in modo non termico modulare la distorsione cristallina dovuta alla distorsione di Peierls. Inoltre, per densità di eccitazione maggiori di 5mJ/cm^2, corrispondenti a 2,5 elettroni eccitati per atomo, una nuova vibrazione risulta essere Raman attiva. Questo dimostra che è possibile, in queste condizioni, eccitare in modo ultraveloce una "fase" di natura non termica. Futuri studi saranno necessari per chiarire la natura di questa nuova intrigante fase transiente.

Nel sesto capitolo abbiamo studiato la transizione di fase metallo-isolante precedentemente riportata in un cristallo organico di EdoTTF$_2$PF$_6$. Misure di resistività sul sale organico di EdoTTF$_2$PF$_6$ mostrano una transizione di fase metallo-isolante abbassando la temperatura al di sotto di 280K. A bassa temperatura la fase isolante è caratterizzata da un ordine di carica ("charge order") delle molecole di EdoTTF. Tramite irraggiamento con impulsi corti a 800nm è stato mostrato che da una fase isolante è possibile ottenere una fase metallica con intensità di irraggiamento estremamente basse (1fotone/500molecole). Le nostre misure di Raman indicano che questa fase fotoindotta transiente, sebbene metallica, abbia una natura diversa dalla fase termodinamicamente stabile ad alta temperatura.

Samenvatting

Het onderzoek beschreven in dit proefschrift is verdeeld in twee hoofddelen. In het eerste deel (hoofdstukken 2 en 3) wordt standaard Raman spectroscopie, in combinatie met andere technieken, gebruikt om de magnetische en structurele eigenschappen te onderzoeken van twee verschillende kristal families, te weten de zeldzame-aard ijzerboraten: $RFe_3(BO_3)_4$ (R = Gd, Tb, Nd, Y en Er) en de titanium-oxyhaliden: TiOX (X = Cl and Br). Het tweede deel van dit proefschrift (hoofdstukken 4, 5 en 6) wordt gewijd aan de beschrijving van de door ons ontwikkelde dynamische versie van Raman spectroscopie. Twee verschillende benaderingen om dynamische Raman informatie te verkrijgen worden eerst beschreven in hoofdstuk 4 en vervolgens toegepast om optisch geïnduceerde fase overgangen in halfmetalen (hoofdstuk 5) en in een organisch, ladings-geordend zout te bestuderen (hoofdstuk 6).

In het tweede hoofdstuk doen we verslag van een cascade aan fase overgangen die de familie van verbindingen genaamd de 'zeldzame-aard ijzerboraten' kenmerken. Een structurele fase overgang bij hoge temperatuur wordt gevolgd door twee magnetische fase overgangen bij lagere temperatuur: een antiferromagnetische ordening en een spin-flop overgang. Door de vibrationele eigenschappen (d.w.z. de fononen) te bestuderen konden we laten zien dan de structurele overgang een ongebruikelijk "licht eerste orde karakter" heeft; de order parameter van de fase overgang laat ongewoon gedrag zien dat het midden houdt tussen een eerste orde overgang (het vertoont hysterese) en een tweede orde overgang (ook een zgn. 'soft mode' is aanwezig). Dit afwijkende fenomeen wordt uitgelegd vanuit de eigenaardige symmetrie eigenschappen van deze familie van verbindingen. Daarnaast bracht de analyse van de magnetische excitaties de aanwezigheid van magnetische correlaties over korte afstand in de paramagnetische fase aan het licht, zelfs tot bij ongekend hoge temperaturen. Dit wordt in hoofdstuk 2 besproken door middel van de laag-dimensionale structurele eigenschappen van het magnetische systeem.

In het derde hoofdstuk presenteren we een op symmetrie gebaseerde uiteenzetting van de verschillende fasen van een groep overgangsmetaal oxiden, namelijk de titanium oxyhaliden (TiOCl en TiOBr). De electronische configuratie van de Ti ionen ($3d^1$) maakt, samen met het laag-dimensionale karakter van de magnetische interactie, deze systemen tot ideale kandidaten voor een zgn. spin-Peierls over-

gang, een overgang voorheen gezien in slechts één andere inorganische verbinding. Onze Raman studie van de fase overgang onthulde twee bijzonder interessante aspecten: i) de fase overgang bij lage temperatuur (de spin-Peierls overgang) wordt, bij een hogere temperatuur, vooraf gegaan door een tweede fase overgang naar een tussenliggende fase; ii) de spin-Peierls overgang heeft een eerste orde karakter, in strijd met de convertionele theoretische beschrijving. In hoofdstuk 3 leggen we ook uit hoe we, door de symmetrie van de vibrationele modes in de drie fasen te analyseren, de ruimtegroep van de spin-Peierls fase konden suggereren (een suggestie die later werdt bevestigd door een Röntgen-diffractie structuurbepaling). Op basis van dezelfde aanpak geven we een aantal symmetrie argumenten om het afwijkende eerste orde karakter van de spin-Peierls overgang te verklaren.

In het vierde hoofdstuk beschrijven we de verschillende experimentele opstellingen die werden gebruikt in de experimenten en de procedures die nodig waren om deze opstellingen te karakteriseren. Het hoofdstuk begint met een beschrijving van de 'continuous wave' Raman opstelling, waarbij we de specificaties van het systeem in ogenschouw nemen. In het tweede deel van het hoofdstuk worden de twee benaderingen om dynamische Raman informatie te verkrijgen beschreven. De eerste aanpak, gebruikt voor de experimenten in hoofdstuk 6, is gebaseerd op een zelfgemaakte mechanische chopper en haalt een tijdsresolutie van 10 μsec en een frequentieresolutie van 1 cm^{-1}. De tweede benadering (toegepast in hoofdstuk 5) gebruikt normale interferometrische technieken om een tijdsresolutie van een aantal picoseconden (10^{-12} sec.) te halen, wat echter ten koste gaat van de frequentieresolutie, die ongeveer 8 á 10 cm^{-1} wordt.

In het vijfde hoofstuk bespreken we onze studie naar de elementaire kristallen van bismut en antimoon. Bij kamertemperatuur wordt de thermodynamisch stabiele phase van beide materialen gekenmerkt door halfmetallisch gedrag, als gevolg van een Peierls vervorming van het rooster (d.m.v. het "Jones-Peierls mechanisme"). Met behulp van ultrasnelle Raman metingen konden we twee verschillende dynamische processen onderscheiden, die volgen op excitatie door een intense laser puls. De langzaamste van deze twee processen kon worden toegeschreven aan een thermisch effect (verhitten van het materiaal), terwijl de snelste een non-thermisch en dus direct optisch geïnduceerd effect laat zien. We konden laten zien hoe het mogelijk is om de kristal vervorming op een non-thermische manier te reguleren. Door middel van optische excitatie van electronen naar de geleidingsband, wordt de electronische energiewinst van de Peierls vervorming gereduceerd, met als gevolg dat deze vervorming (tijdelijk) instabiel wordt. Bovendien wordt een nieuw fonon Raman actief bij excitatiedichtheden hoger dan 5 mJ/cm^2, een dichtheid die overeenkomt met ongeveer 3 geëxciteerde electronen per atoom. Dit hebben we geïnterpreteerd als bewijs voor een optisch geïnduceerde fase overgang naar een non-thermische "fase", iets dat hopelijk toekomstige studies stimuleert om de precieze aard van dit fenomeen op te helderen.

In het zesde en laatste hoofdstuk presenteren we een studie naar de eerder ontdekte, optische geïnduceerde isolator-metaal fase overgang in het organische kristal $(EDO\text{-}TTF)_2PF_6$. Metingen van de electrische weerstand van dit organ-

ische zout laten een metaal naar isolator overgang zien wanneer de temperatuur wordt verlaagd tot beneden 280 K. De isolerende fase bij lage temperatuur wordt gekenmerkt door een ladingsordening in de EDO-TTF moleculen. Eerder was al laten zien dat door de lage temperatuursfase te bestralen met licht pulsen van 800 nm bij een extreem lage excitatiedichtheid (1 foton per 500 moleculen), het mogelijk is een tijdelijke metallische fase te induceren, die een paar honderd microseconden aanhoudt. Gesuggereerd werd dat deze vergankelijke fase in feite niets anders is dan de metallische hoge temperatuursfase. Onze tijdsopgeloste Raman metingen geven een duidelijke indicatie dat de foto-geïnduceerde fase, hoewel ook metallisch, wel eens van een andere aard kan zijn dan de hoge temperatuursfase.

Acknowledgments

The task of acknowledging all the people to whom I'm grateful for all these years in Groningen it's a major one. I'm sure that, no matter how long I will work on these acknowledgements, I will forget somebody. Hence, to make it safe and to protect myself from future complaints, retaliations and "revenges", I'll start by saying that I'm grateful to all people I've shared these very important years of my life, even those that now I don't remember.

The first personal acknowledgment naturally goes to my supervisor Paul H. M. van Loosdrecht. Your "physics sense" and your approaches to problems, Paul, gave me precious insights both in scientific and non-scientific questions. You always manage to give me directions and at the same time I always felt free of going in the direction I wanted. Thanks Paul, they have been five wonderful years!

A sincere acknowledgment goes to the reading committee of this "proefschrift". I'm grateful to Petra Rudolf for driving me in the difficult task of putting myself into the "reader's shoes" and for all the precious tips, scientific and not, she gave me over the years. I'm grateful to Daniel Khomskii for the deep and detailed remarks that improved this thesis, and for the precious discussions we had during my Phd period. After my graduation, when Fulvio Parmigiani asked: "Why don't you go to Groningen for a Phd?". My first reaction was: "I'm not sure I want to go to Germany!" Five years later, Fulvio, I can confess that I'm greatly in debt with you for initiating this. Not only I got to know where Groningen is, but I had the opportunity to work with people from whom I really learned a lot.

This brings me to the due acknowledgements to the entire optical condensed matter physics group in Groningen, the present and the old one. I'm grateful to Maxim for teaching me the parsimony in asking questions and to Victor for always being very talkative (oops, maybe I swapped them!!); jokes apart, I've learned a lot from you. I'm grateful to Audrius for reminding me constantly that after all I'm just a lazy b**d, cause in the end "it's always easy to align the laser" (for you!); thanks for teaching me so much.

It was a pleasure to work with the craziest group of technicians; Ben, Foppe and Arjen many things would have not been possible without you, thanks a lot! I would also like to mention that I'm proud I managed to finish this thesis despite Arjen... rather than despite him, I would say despite the endless, pointless, meaningless and hopeless lunch discussions he initiated daily (I loved them!). Ob-

viously he was not alone in keeping me out of the lab. I loved "working" with Artem (thanks for the climbings), Michiel, Ramunas (the third smartest spectroscopyst in the world!), Tom (the second!), Ruben, Marianne, Filippo, Sonia, Renate, Puri, Pedro, Dima one and two (you can fight over the numbers!), Silviu, Sagar, Cosmina, Dan and Patricio (buena suerte in Santiago!).

A special acknowledgment goes to Filippo, for bringing the *mariöla* (salami) regularly from Piacenza, for sharing with me the little Italy in the office, and especially for never complaining about my mess (there will always be a couch for you in my house!).

Before the great "removal", the honor of sharing my mess was reserved to Tom, alternatively called the "helpdesk". Thanks a lot, Tom, for replying always, and "almost calmly", to the tens of questions I was daily firing at you. Concerning this thesis, thanks a lot for the long editing checks (and by now you know how much my English needs it!!) and for translating the "samenvatting"; I'm looking forward to see you in the tuxedo.

A special memory goes to Katarzina.

It has been great to work and share with all of you my life in Groningen. Thanks!

There are dozens of people I have been working with in the past years. I'm greatly indebt to Sergei Klimin for helping me in getting started with the setup of the lab. I would also like to acknowledge all the co-authors I have been working with: Auke Meetsma, Tom Palstra, Agun Nugroho, Bernd Buchner, Natalia Tristan, Xavier Luzon, Ria Broer, Roberto Macovez (...I decline any responsibility concerning your choice of moving to optics!), Petra Rudolf, and Marina Popova. All the experiments reported in this thesis would have not been possible without samples. Hence I'm really grateful to all the people who supplied us the samples for the different projects: Sander van Smaalen (TiOBr); Angela Möller, Gerd Meyer, and Timo Taetz (TiOBr, TIOCl); Shin-ya Koshihara (EDO-TTF_2PF_6); Leonard N. Bezmaternykh ($RFe_3(BO_3)_4$); Oleg Mishoco (Bi and Sb). Special thanks go to Maxim Mostovoy for the enlightening "five minutes" discussions that could last for hours, and to all the people I've been discussing different different subjects of this thesis: Michiel van der Vegte, Paul de Boeij, Iberio Moreira, Markus Grüninger. Thanks to all the "Graphene people", especially to Csaba, Nikos, Alina, Pedro, and Shinichi.

I'm grateful to my former colleagues in the department of physics to the Catholic University of Brescia (UCSC) for always been keen to share results and ideas with me. In Particular I'm grateful to Claudio Giannetti, Francesco Banfi, and Gabriele Ferrini for the always insightful opinions they gave on my scientific and technical questions.

I will always be grateful to Francesca Gambardella and Michele Zaffalon. Thanks for getting me acquainted to the Netherlands and especially for the Saturday afternoon breakfasts with all the Italian "mafia": Francesca, Anton, Sandra, Francesco & Fiorella (also known as Picchionis).

My life in Groningen wouldn't have been the same (maybe healthier!) without

"i fantastici quattro" (the "Fantastic Four") accompanying me through the, by now mythical, Groningen Friday night battles: Alessio (you look much better with the blond beard!), Filippo (remember I'm lefty!), Primos (thanks for the parsimonious speaking!), and Simon (you know already what I like about you!). The four superheroes' were often supported by a bunch of braves in this difficult task: Damiano (always relaxed!), Roberto (not really interested in dark and strongly tasting Belgian beers, more into easy "blondes"!), Fabrizio ("piede amaro", seeing you play was always getting me emotional!), Tom (the "fris" alter ego!), Eleonora (only until 10.30!), Carol (for my promotion you have to drink a beer!), Tati, Lumi, Pablo, Regis, Jesus. A great acknowledge for hosting, always gently, these epic battles should be given to the "Pintelier staff". It was great fun, I'll miss those battles!

A particular acknowledgement goes to Simon, Simone, and Zöe for providing the only warm meals I would eat during the long months I spent writing this thesis, for the nice climbing together, and especially for Simon's patience in correcting my English.

The deepest acknowledge goes to my family. To my parents because their love and unconditional support to my choices always made me feel protected, loved and secure. To my sister and "brothers" cause no one has ever made me feeling "at home" as being with Claudia, Eugenio and Remo; and nothing has ever given me more joy than having Giulia on my lap. I want to welcome also the new comer, only the thought of him/her makes me joyful. *Grazie di cuore a tutti!* A thanks from my heart to all those that from far away have always been close to my heart and in particular, *un augurio allo zio Beppe di pronta guarigione.*

The last, but not least, I have to acknowledge Stefania (this goes into the due acknowledgments to avoid retaliations!). I'm grateful to you for always understanding me, standing my frustrations, and always succeeding in bringing me back to the real world when my mind is trapped into some parallel (possibly non-thermodynamical) universe. For this and much more I love you.

Daniele, Groningen, 2008